UNIVERSITY OF STRATHCLYDE
Department of Physics

Technology development for studying information flow in biological neural networks

by

Yunzhou Cheng

A thesis presented in fulfilment of the
requirements for the degree of
Doctor of Philosophy

July 2019

Declaration of Authorship

This thesis is the result of the author's original research. It has been composed by the author and has not been previously submitted for examination which has led to the award of a degree.

Signed: _____

Date: _____

Frontispiece

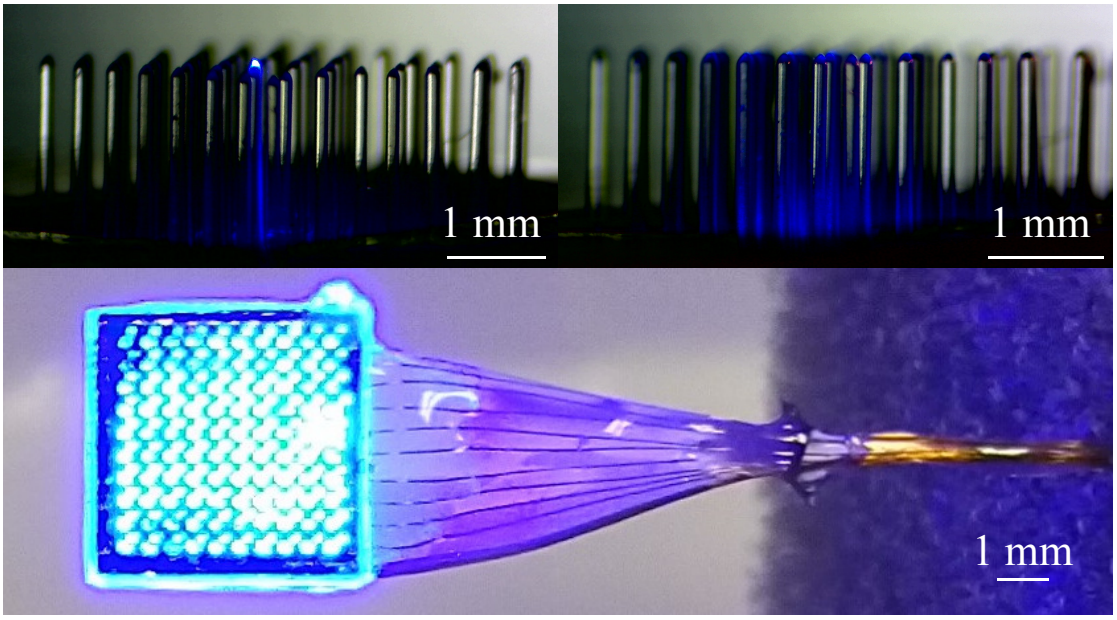

Micro-structured light emitting diode coupled glass optrode array. Top: prototype with metal pinhole layer. (Left) a lighted needle-aligned pixel for deep brain stimulation; (Right) a lighted interstitial pixel for brain surface stimulation. Bottom: prototype with silicon interposer structure with all pixels lighting up. The optrode array was wire bonded to electrical driven system by insulated gold wires and the device was encapsulated with a water proof polymer. (Scale bar: 1 mm).

Abstract

This thesis mainly focuses on the technology development of electrophysiological recording devices and optical stimulation devices for studying the information flow along the neural network in the brain. Specifically, it concentrates on the penetrating microelectrode array and the micro-sized light emitting diode (μLED) coupled glass optrode array for electrophysiological recordings and optogenetic applications respectively. Since a neuron is an electrically excitable cell which is the basic building block of human brain, its electrical activities (spikes) are responsible for functions such as vision, speech, hearing, learning and memory. Therefore, neural recording is one of the efficient ways to understand the relationship between neural activities and brain functions. Devices like microelectrode arrays have been developed to extract the spikes from brain tissue to a read-out electronic system for analysing. In order to identify and sort out spikes generated by a single neuron, the electrode density of the penetrating microelectrode array in this project is about 350 electrodes/mm^2. With the 200-μm long needles, the microelectrode array can penetrate the outer layer of sliced brain tissue and contact to the healthy cells underneath. Low impedance electrodes (450 kΩ at 1 kHz) makes the device able to record the small (hundreds of microvolts) extracellular signals. On the other hand, neuronal modulation is another strategy to investigate the information flows in neural networks. Compared to the electrical stimulation, optogenetics provides an optical modulation to the neurons with high selectivity and spatiotemporal resolution. In this project, a μLED array is designed and fabricated as a light source for a coupled optrode array. In terms of the design, the optrode array is able to provide an optical irradiance of about 80 mW/mm^2 at the needle tip which is enough to optically excite up to 5500 neurons in the sub-cortical structures. Moreover, the optrode array can provide both deep brain stimulation and superficial illumination of the brain cortex. Besides, multi-site stimulation could also be achieved by lighting up one or more LED elements. During the stimulation, the temperature change can be kept below 1 °C which will not affect neuronal signalling in the cortex.

Acknowledgements

First of all I'd like to thank my supervisor, Prof. Keith Mathieson. Thanks for giving me this opportunity to join several interesting projects and for his guidance, inspiration, patience and support. In particular, he helps me a lot to overcome all the difficulties during my PhD studies. I am also thankful to Prof. Martin Dawson and Dr. Ian Watson for their supports throughout my studies.

Many thanks must be given to Dr. Niall McAlinden who helps me a lot in building setups in the laboratory and setting up computer stimulations and Dr. Enyuan Xie who patiently teaches me the skills of semiconductor fabrication. I also receive valuable suggestions from them during my studies.

I also want to thank all my colleagues for making me feel relax and comfortable in IoP during working period. They help me a lot in both study and daily life. It is my honor to work and live with all the good friend I met in IoP.

Finally, I must to thank my families for their unconditional supports and encouragement all the time.

Contents

List of Figures

List of Tables

Dedicated to my family

Chapter 1

Introduction

People have been intrigued by the inner workings of our brains since the dawn of civilisation. We have striven to understand how we sense the world, what governs our emotions and how we learn and remember. Contemporary neuroscience research has revealed that the brain is an exquisitely complex organ. However, many aspects of its function are still not fully understood. Recently, huge collaborative efforts have been made to attempt to fill in some of the gaps in our understanding. These include large multi-disciplinary projects such as the Human Brain Project in Europe with €1.019 billion of funding [4, 5] and the BRAIN Initiative in the USA with $4.5 billion of funding [6, 7]. The work throughout this thesis aligns with these collaborative projects, aiming to develop new devices for neuroscience that allow researchers to push the boundaries of current human understanding.

1.1 Motivation

The human brain is one of the greatest mysteries in science with 10^{11} neurons and more than 10^{15} connections [8]. Neurons are key building blocks of the brain; they are responsible for information flow and processing. As such they are the key focus of most neuroscience work. Neurons process information through the use of both chemical and electrical signalling, however, the majority of the information flow is through electrical pathways. Recording these electrical signals is a popular strategy to investigate the links between neural activities and brain functions. In the past decades, tremendous efforts have been made to enable neural recordings (Fig. 1.1).

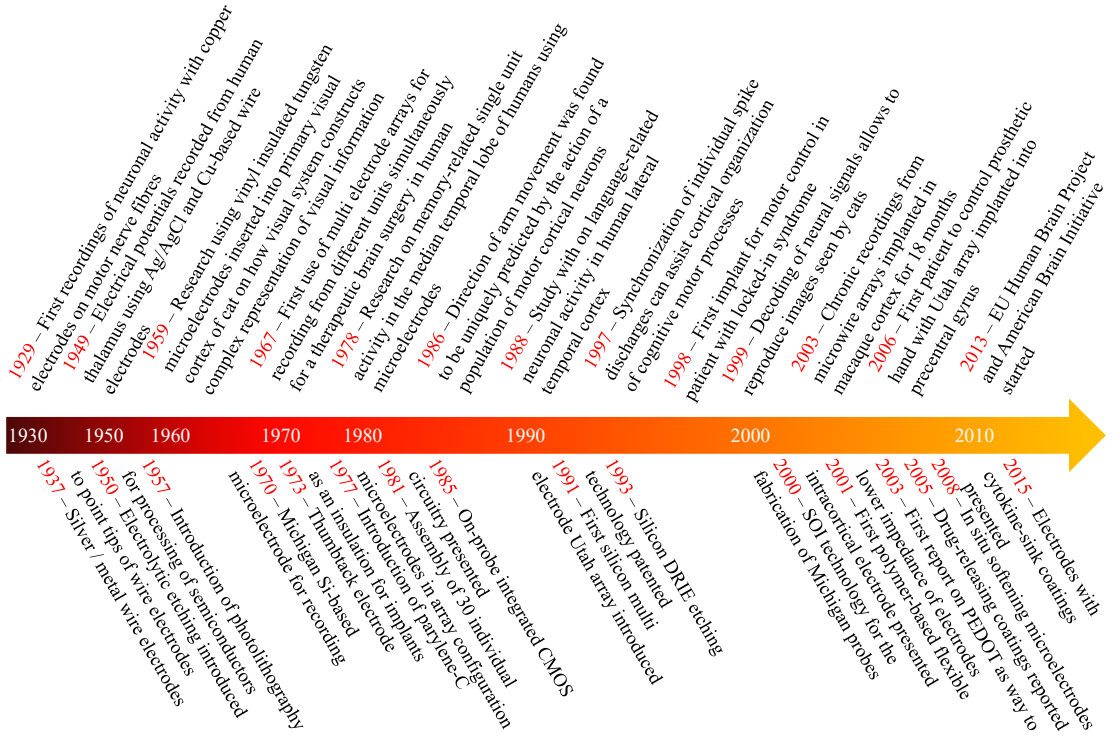

FIGURE 1.1: Time scale for the development of neuroscience. (Above the time arrow) time scale of milestones in neuronal recordings [9–20]; (Below the time arrow) time scale of developments in semiconductor microfabrication technologies [21–36]. After [37]

In 1929, one of the earliest neural recordings was reported by Edgar Adrian [9]. He inserted a concentric needle electrode (a 36-gauge needle with an enamelled copper wire in the centre) into the muscles and record neural activities from motor nerve fibres [9]. His refined method could be applied to achieve neural recordings from muscles, not only in a laboratory animal, but also in human being. As a reward of the excellent work in neural recordings, the Nobel Prize in Physiology or Medicine was given to Adrian and Sherrington in 1932. In the following decades, single-unit electrodes such as glass micro-pipettes or metal microelectrodes made of platinum or tungsten have been used to obtain neural activities from neurons [38, 39]. Even though individual neural signals could be recorded and analyzed, recording from many neurons simultaneously is required to understand the information flow in neural circuits. In order to record neural activities from large population of neurons, devices such as microelectrode arrays have been developed to enable high

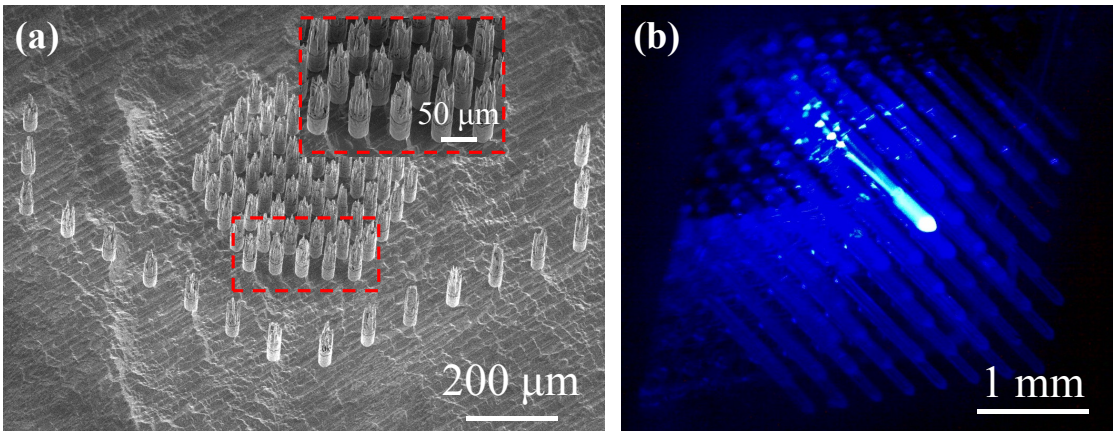

FIGURE 1.2: Novel devices developed in this project. (a) Scanning electron microscopy (SEM) image of high-density penetrating microelectrode array. Scale bar: 200 μm. (inset) close-up image of needles. Scale bar: 50 μm; (b) Image of optrode array with one illuminated element. Scale bar: 1 mm.

spatial resolution neural recording. For the most recent and advanced devices, the structure of microelectrode array has been transformed from two dimensional to three dimensional, which enables microelectrode arrays to access the neurons in deeper regions of brain. Furthermore, penetrating microelectrode arrays are able to achieve electrical recordings from neurons in a three-dimensional distribution in the brain.

Microelectrode arrays are not only able to achieve neural recording, but also to enable electrical neural stimulation. Based on the nature of neuron, electrical stimulation of neurons can initiate a response by depolarizing the membrane potential of the neuron. In this way, the activity of the nervous system could be modulated by applying electrical current. However, electrical stimulation results in the depolarization of all neurons around the stimulated area. This makes it a challenge to link brain functions to the activities of specific neurons. To face this challenge, a novel stimulation technology called optogenetics has been developed to optically control the behaviours of neurons that have been genetically modified. This technique was named as the "Nature Method of the Year" in 2010 [40]. By applying genetic engineering processes, targeted types of neurons can be transformed into light-sensitive neurons and only genetically targeted neurons generate electrical signals in response to a light pulse. Consequently, optogenetics opens a new door for exploring brain functions.

During this thesis, novel devices have been designed and fabricated for the investigation on how information flows in a neural network. In order to record

signals from neurons located in deep brain regions, a penetrating microelectrode array with high electrode density has been developed (Fig. 1.2(a)). Moreover, three-dimensional electrodes are able to penetrate into the deep region of brain to extract signals from neurons that are difficult to reach [41]. Micro-structured light emitting diode (μLED) arrays have been fabricated for optogenetics. A μLED is a simple but powerful source that could be easily integrated with other devices. Here, the μLED array is coupled to a Utah glass needle array [42, 43] so that the light could be guided into the deep brain region in a minimally invasive fashion (Fig. 1.2(b)). The integrated device, named as optrode array, enables optical control on neural behaviours with high spatiotemporal resolution and minimal heat generation. Details of both devices are demonstrated later in this thesis including fabrication steps and performance characterizations.

1.2 Outline of thesis

In this thesis, the background of this interdisciplinary project is introduced in chapter 2, including neuroscience and the state-of-the-arts in this field. In chapter 3, experimental semiconductor fabrication techniques used in this project are described. In subsequent chapters, device fabrication and characterization are all covered: chapter 4 describes the fabrication process of penetrating microelectrode array; characterization of penetrating microelectrode array is also included in this chapter. The fabrication process and characterization of μLED coupled glass optrode array is detailed in chapter 5. All experimental results show that the devices have good performance and could be applied in further biological experiments. Finally in chapter 6, an overall conclusion is given and some new ideas for future work are outlined.

Chapter 2

Neuroscience and optogenetics

Neurons are electrically excitable cells and are the basic computational building block of the brain. Because of their unique structures, they can communicate with each other via electrical and chemical signalling. Electrical signals can propagate along the neural structure, for example, slow-wave potentials and local field potentials. On the other hand, chemical signals such as neurotransmitters pass from one neuron to the next adjacent neuron. It is known that the electrical signals are partly responsible for many brain functions. They can propagate in the whole nervous system so that the brain can control our behaviour efficiently. To date, several technologies have been developed that allow us to electrically record from neurons and help to improve our understanding of the interactions between neurons. In particular, two popular types of microelectrode arrays are the Michigan probe [44] and the Utah microelectrode array [45]. Both of them enable electrical recordings from large population of neurons. Moreover, some types of microelectrode arrays could also enable electrical stimulation [46, 47]. However, when introducing an electrical stimulus, a group of neurons around the stimulus would be activated simultaneously. Therefore, the electrical stimulation is unable to selectively activate specific types of neurons or activate neurons in the specific region of brain. In order to stimulate a certain type of neuron or neurons in specific region, a novel strategy called optogenetics has been developed [48]. In this chapter, an introduction to neurons is given in section 2.1 including neuron structure and function and in section 2.2, the development of optogenetic technique is introduced. In section 2.3, microelectrode array technology for neural recording and stimulation is detailed highlighting the state-of-the-art of electrophysiological devices. Devices for optogenetics are also described in this section.

2.1 Structures and functions of neuron

The human brain consists of billions of neurons and each neuron has up to 10,000 synapses [49, 50]. The structure of a neuron is different from other cells in the human body [1, 51]. There are three main parts in a single neuron: soma, axon and dendrites. The schematic of neural structure is shown in Fig. 2.1.

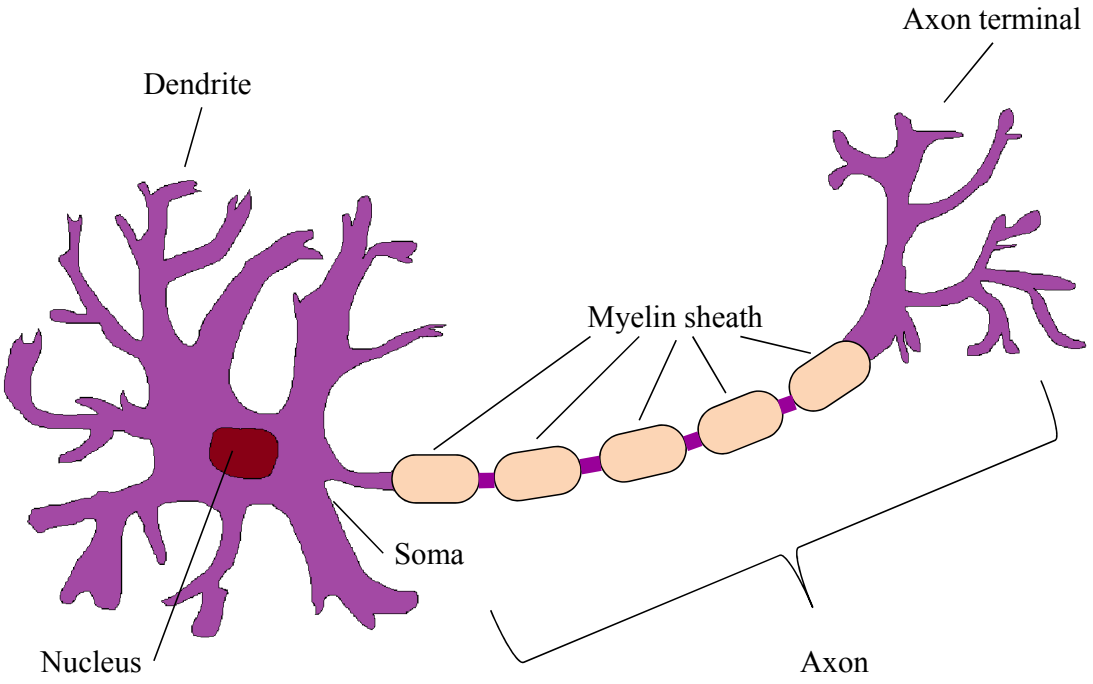

FIGURE 2.1: Schematic of neuron structure, including three parts: soma (cell body), axon and dendrites.

The soma is the cell body which contains the same organelles that are found in all animal cells and the size of soma varies from 10 μm to 25 μm in diameter. The most important component inside the soma is the nucleus, which contains DNA (deoxyribonucleic acid). DNA contains the blueprint of growth, development, function and reproduction. To control the cellular behaviours, proteins are produced based on the sequences of DNA to participate in virtually every process within cells. For example, some proteins are enzymes that catalyse biochemical reactions. Other proteins also function as structural units in cell membranes to maintain the stability of the intracellular environment (cytoplasm).

Axon and dendrites are extensions of the soma. The axon begins with a region of soma called the axon hillock and can extend from less than a millimeter to over a meter long. The end of axon is called the axon terminal. This is the point of the neuron that makes contact with the dendrites of another neuron. The contact point

is called a synapse and each neuron has up to 10,000 synapses. The synapse has two sides: presynaptic and postsynaptic side. The presynaptic side is on the signalling neuron and the postsynaptic side is on the receiving neuron. Neurons receive a signal or multiple signals from their dendrites, processes the signal and then if the correct conditions are met a new action potential is generated and passed down the axon to a neighbouring neuron/neurons. Since the structures of dendrites are similar to the branches of a tree, each neuron can make at least 10,000 connections to other neurons, allowing neurons to build the complex nervous system.

The entire neuron is defined by the neuronal membrane. The membrane acts as a barrier to separate the cytoplasm from the extracellular fluid. The cross-section of neural membrane is shown Fig. 2.2. The basic chemical unit of the membrane is the phospholipid and it contains a long tail, which is hydrophobic and a head which is hydrophilic. When making a neuronal membrane, the hydrophilic heads of phospholipid molecules face the outer and inner water-based environment and the hydrophobic tails face each other. As a result, the phospholipid molecules form a stable structure called phospholipid bilayer. Moreover, there are proteins studded inside the phospholipid bilayer, which are called channel proteins. These proteins form ion channels and are able to allow ions to flow across the cell membrane. In this way, a balance of neuronal internal environment and external environment is kept to maintain the normal function of neurons. In particular, the information transmission between neurons mainly depends on the neuronal membrane, and the channel dynamics.

When the neuron is in rest state, the ion concentrations in both the internal and the external environment is different. As shown in Table 2.1, potassium ions (K^+) are more concentrated inside of the neuron and sodium ions (Na^+) are more concentrated outside the neuron due to the high selective permeability to K^+ ions.

TABLE 2.1: Approximate ion concentrations on each side of a neural membrane: the Giant Axon of the Squid [1, 2].

Ion	Concentration outside (in mM)	Concentration inside (in mM)
K^+	20	400
Na^+	440	50
Cl^-	560	52
A^- (organic anions)	–	385

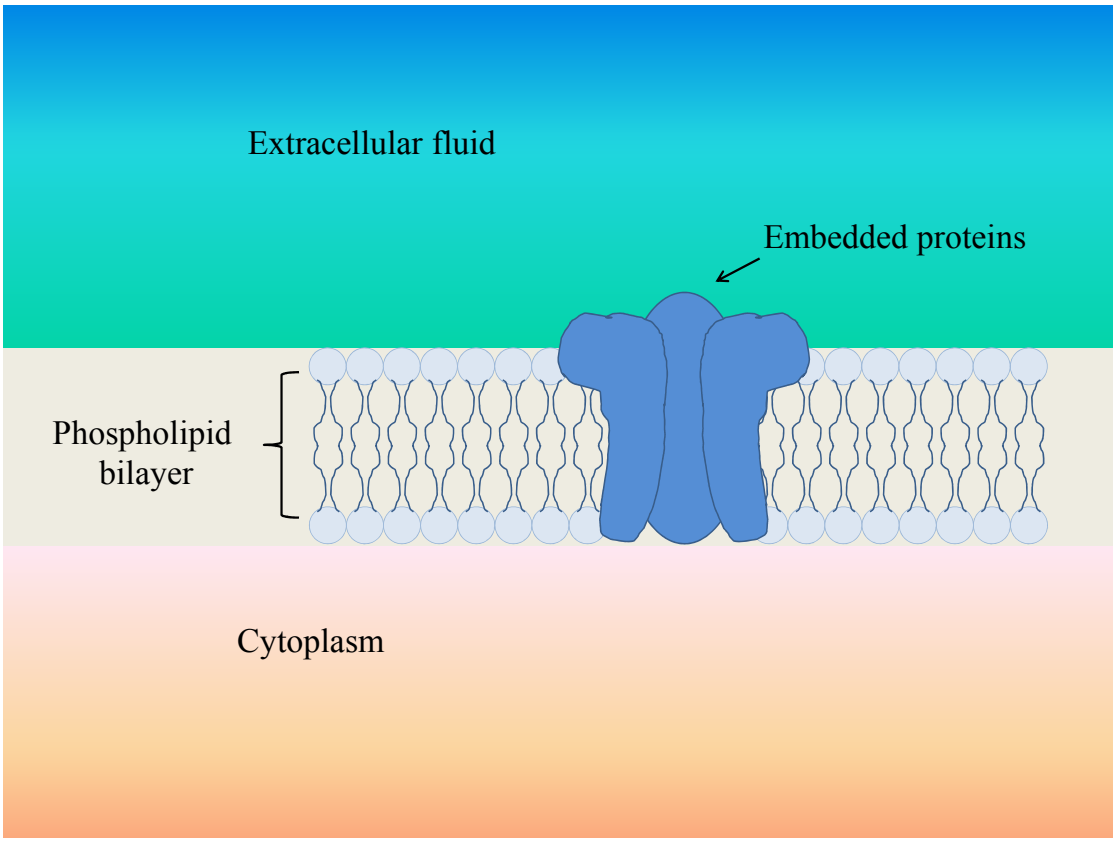

FIGURE 2.2: Cross-sectional diagram of neural membrane. The phospholipid bilayer is the main component of neural membrane and the embedded proteins form ion channels that allow ions flow into and out of neuron.

Typically, the measured resting potential is about -75 mV with respect to the outside [1, 51]. The discrepancy between the measured resting potential and E_{ion} given in Table 2.1 demonstrates that the real neurons at rest are not exclusively permeable to potassium ions or sodium ions. The resting potential is contributed to by concentrations of all types of ions inside and outside of the neurons.

When the neuron is at excitable state, the proteins will open the Na^+ channels. Because of the large concentration gradient between inside and outside of neuron, the Na^+ ions can flow into the neuron. As a result, the cytoplasm becomes less negatively charged and the neural membrane is depolarized. When the depolarization passes a certain threshold level, the membrane will generate an action potential. When the action potentials propagate to the axon terminal, the depolarization will make the synapse release a chemical signal called a neurotransmitter to the postsynaptic terminal of the neuron. Therefore, the information in the form of action potential is transformed into a chemical signal at the presynaptic terminal

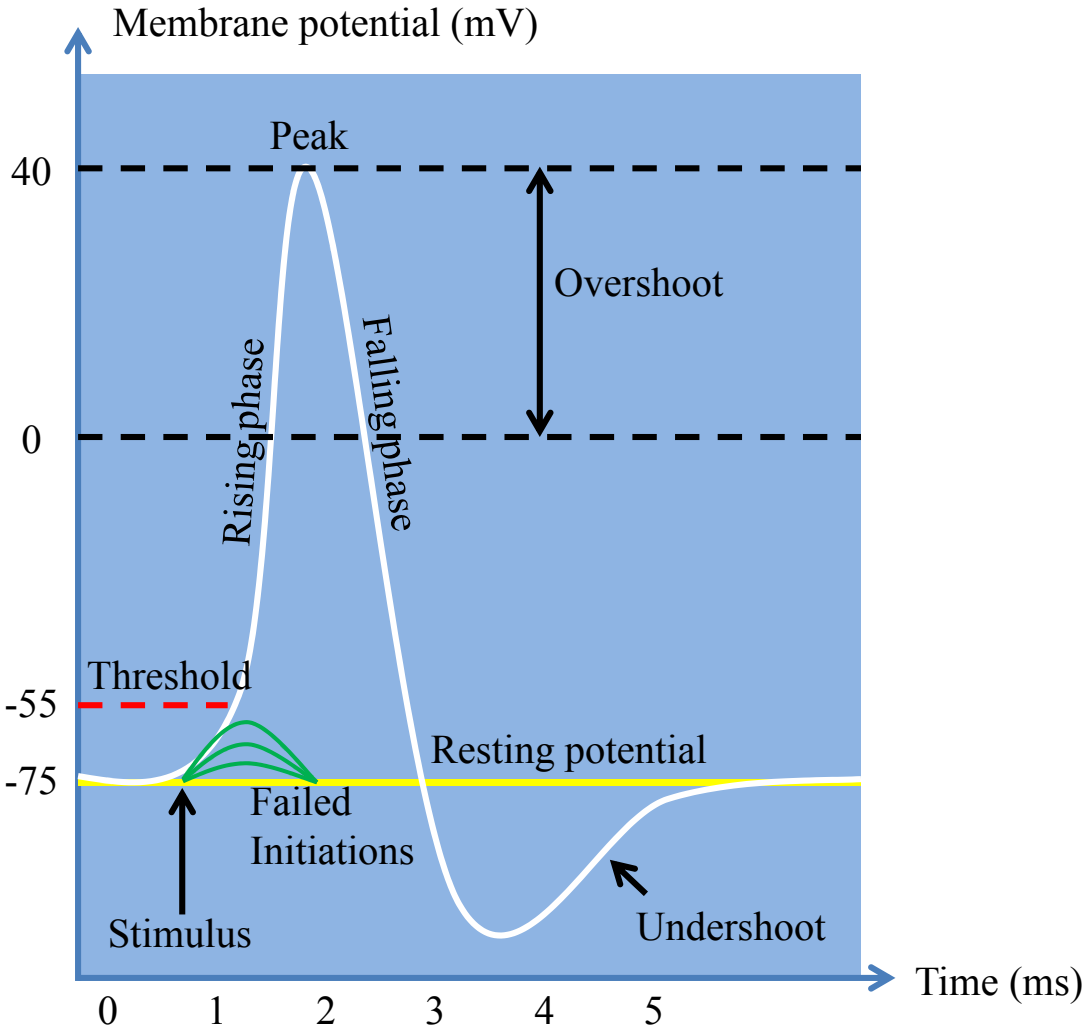

FIGURE 2.3: Schematic of an action potential from any intracellular microelectrode measurements. If the stimulus is not strong enough, the initiations (green) could not reach the threshold level (red) and would be back to resting potential (yellow) rapidly. However, the action potential is triggered (white) with certain identifiable parts: resting potential, rising phase, overshoot, falling phase and undershoot. After [51]

and the chemical signal then is converted into an electrical signal at the postsynaptic side of next neuron. As a result, the information spreads out in the entire neural network via electrical and chemical signals.

In this thesis, I focus on the development of devices to record or elicit action potentials. The basic waveform of a single action potential is shown in Fig. 2.3. If the stimulus is not strong enough to trigger the depolarization over the threshold level (typically about -55 mV [52]), the initiation would return back to resting potential rapidly. On the contrary, an action potential would be generated by the neuron as a response to the stimulus. From the beginning to the end, the

action potential typically lasts a few milliseconds (ms). Therefore, I designed and fabricated a novel type of device for electrical recording and the details will be given in the following chapters. In the next section, recent technologies for electrical recording are reviewed to show the state-of-the-arts in the electrophysiological recording field.

2.2 Technologies for electrophysiological recordings

In the past decades, different types of devices for electrical recordings from neurons have been developed. In 1959, Hubel and Wiesel demonstrated neural recordings from single neurons in the striate cortex of cats by using tungsten-based microwire electrodes [11]. Based on the experimental results, Hubel and Wiesel found the relationship between the brain regions and the visual functions. Moreover, they discovered how nerve cells process the sensory information on their way from the retina to the cerebral cortex and how the cortex changes during the information process. In 1981, Hubel and Wiesel received the Nobel Prize in Physiology or Medicine for discoveries on how information is processed in the visual system [53]. Other materials such as platinum and iridium were also used to make microwire electrodes [54, 55]. However, the neural recording achieved by microwire electrodes could not be used to clarify the information flow in neural circuits due to the low spatial resolution. Therefore, novel microelectrode arrays have been developed to improve the recording resolution by extracting electrical signals from large population of neurons simultaneously. Due to the high electrode density, signals from up to a thousand neurons could be recorded simultaneously. As a result, neural recordings with high spatiotemporal resolution could be recorded to analyse information flows in neural circuits. Microelectrode arrays are now made from different materials using microfabrication techniques. A review of microelectrode array development is given in the following sections and the related fabrication techniques will be described later.

2.2.1 Planar microelectrode array

One of popular styles of microelectrode arrays is a planar microelectrode array. Normally, planar microelectrode arrays consist of large numbers of individually addressable electrodes which are used to record the action potentials generated by neurons. In 1980, J. Pine et al. demonstrated an efficient way of recording action potentials from cultured neurons via extracellular microelectrode array with 32 electrodes [56]. In order to achieve high recording resolution and high quality of spike sorting, the microelectrode arrays with large area coverage and high electrode density have been developed for different applications in the following decades. As shown in Fig. 2.4(a), Morin et al. fabricated a 8×8 planar microelectrode array, which provided 32 channels to record neural network activity [57]. Typically, the microelectrode array was fabricated on a rigid substrate such as silicon due to the ease of fabrication. However, some experiments required light transmission through the microelectrode array. For example, in order to fully understand the information flow in retina, the photoreceptors could be illuminated by light, resulting in signal generation in the retinal ganglion cells (RGCs) layer recorded by the planar microelectrode array. Therefore, the microelectrode array was required to be transparent to let the light pass through and reach the retina. Litke et al. developed a planar 512 microelectrode array on glass substrate for studying retina *in vitro* [58]. The diameter of electrode was 5 μm and the electrode spacing was 60 μm. All the electrodes and interconnection wires were made of indium tin oxide (ITO), which is a conductive and transparent material. The device was further optimized by Gunning et al. by increasing the electrode density [59]. In their report, they demonstrated a high-density 519-microelectrode array with 30 μm electrode pitch (center-to-center distance between two neighbouring electrodes) to record signals from hundreds of RGCs simultaneously (Fig. 2.4(b)). Considering the size of neurons, which ranges from tens micrometres to a hundred micrometres, it is important to design the microelectrode array with cellular or subcellular dimensions. To achieve cellular or subcellular recording resolution, Frey et al. combined microelectrode array to CMOS system so that the entire array consisted of 11,016 electrodes (7 μm in diameter with 18 μm pitch) [60]. The CMOS-based microelectrode array showed high spatial-resolution recordings with high signal-to-noise ratio from neuronal cells (culture and slice) (shown in Fig. 2.4(c)).

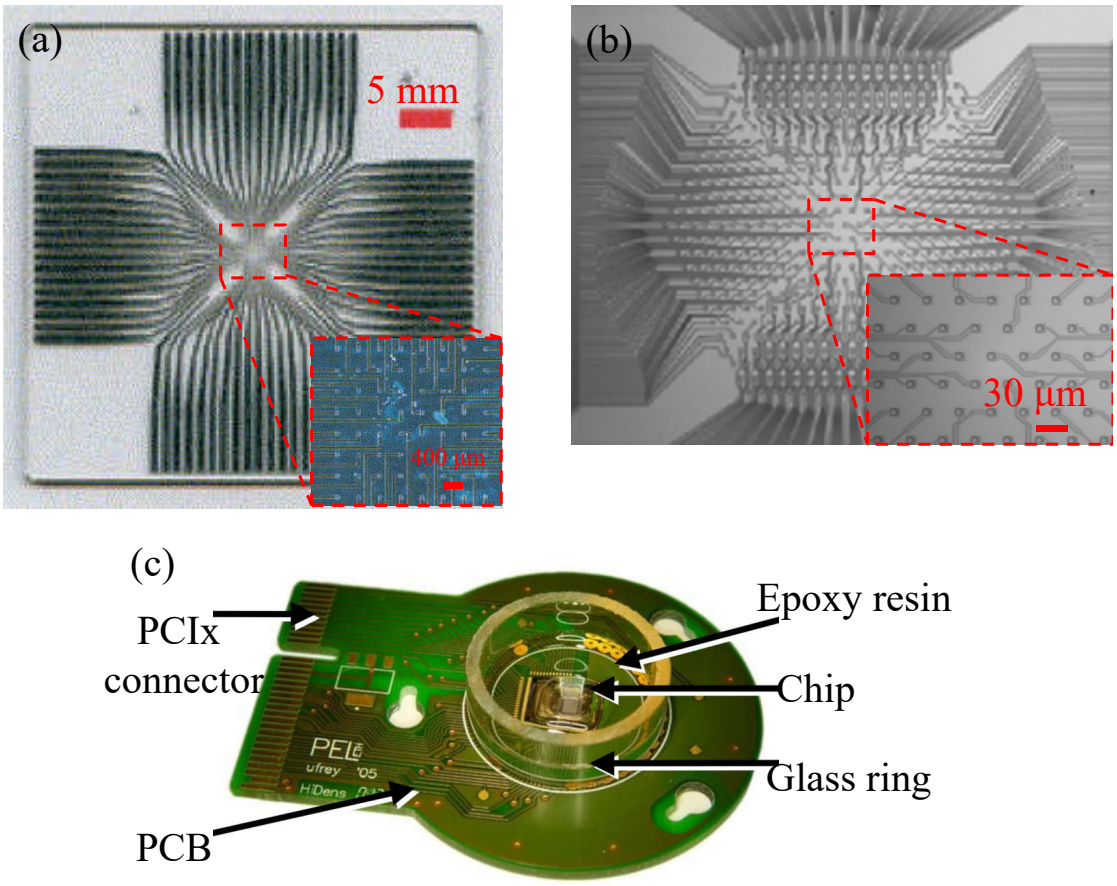

FIGURE 2.4: Different designs of planar microelectrode arrays. (a) The top view of 8 × 8 planar microelectrode array. Scale bar: 5 mm. The inset is the close-up image of array (scale bar: 400 μm) [57]. (b) The 30 μm spacing 519-electrode array designed. The inset is the close-up image of the center (scale bar: 30 μm) [59]. (c) The fully packaged CMOS-based planar microelectrode array [60].

Even though the planar microelectrode arrays have a large number of electrodes and are able to achieve high recording density, they could only record signals from neurons which lie at the surface of tissues. When preparing slices, neurons on the surface of a slice may get damaged during preparation and may not behave normally. Therefore, it would be better for the microelectrode arrays to record from healthy neurons below the surface. However, planar microelectrode arrays could not easily reach neurons located deeper in the tissue. As a result, penetrating microelectrode arrays have been developed to record electrical signals from neurons beneath the surface layer.

2.2.2 Penetrating microelectrode array

When neural tissues, like the brain, are sliced for studying *in vitro*, the surface of the tissue slice may get damaged. As a result, planar microelectrode arrays are unable to reach the healthy neurons with intact connections. Moreover, some neurons of interest are underneath the surface and cannot be contacted directly by planar microelectrode arrays. Therefore, penetrating microelectrode arrays have been developed to overcome those problems. Recently, there are two main types of penetrating microelectrode arrays that are widely used: one is the Michigan probe and the other one is the Utah needle array. Both microelectrode arrays can be made by semiconductor fabrication techniques and the details will be introduced in chapter 3.

The Michigan probe

The Michigan probe is one of the classic types of penetrating MEAs, which was firstly developed by Wise et al [61]. This probe included gold electrodes which were fabricated on a silicon substrate and could be used to record spikes from neurons in the brain. Since then, there has been a drive to reduce probe dimensions and minimize tissue damaging during implantation. Therefore, different probes have been developed in the following decades. Wise et al. developed a single shank probe with multiple recording sites in 1985 [62]. A scanning electron microscope (SEM) image of the device is shown in Fig. 2.5(a). The shank of probe was thinner and narrower (50 μm wide and 15 μm thick) than previous device so that the probe was capable of simultaneous multichannel recording in deep brain with minimal tissue disturbance. In order to record signals from more neurons in deep brain regions, novel designs have since been developed. There is not only single shank with multiple recording sites, but also multiple shanks with multiple recording sites. Norlin et al. fabricated several different probes in 2002. One had single shank with 32 iridium electrodes and the other two had multiple shanks (as shown in Fig. 2.5(b), 8 shanks with 4 electrodes on each shank and 4 shanks with 8 electrodes on each shank) [63]. All the shanks had dimensions of 5 mm $\times$ 25 μm $\times$ 20 μm (length $\times$ width $\times$ thickness) and the sharp tips with angles of 4°. The more advanced neural probe was reported by Scholvin et al. in 2015 [64]. Compared to the old designs, their design included close-packed microelectrodes (1000 recording sites with the pitch of 11 μm and each site is 9 μm $\times$ 9 μm, Fig. 2.5(c) & (d)) which enabled spatial oversampling of neural activity in the live

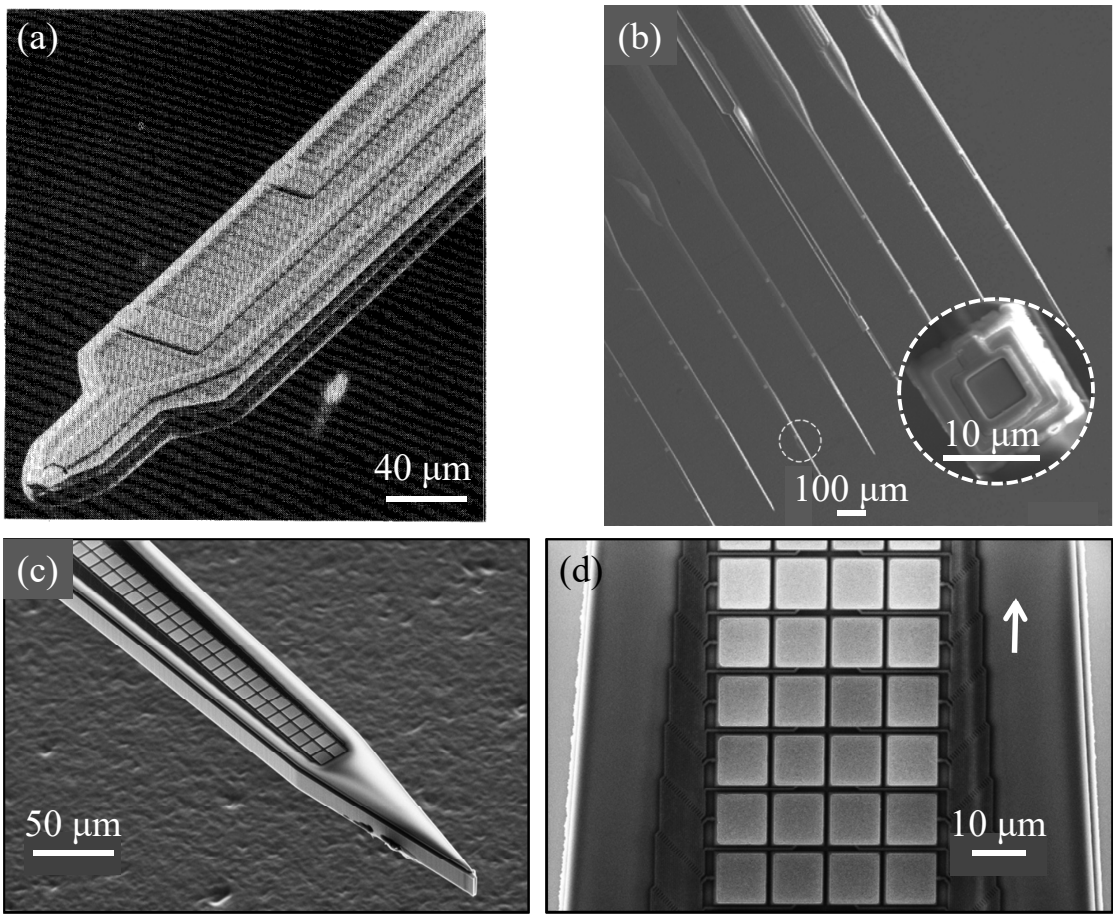

FIGURE 2.5: SEM images of different types of probes for neural recordings. (a) The probe with single shank. Scale bar: 40 μm) [62]. (b) Multi-shank probe, with 4 recording sites on each shank. Scale bar: 100 μm). The inset shows a close-up image of single electrode. Scale bar: 10 μm) [63]. (c) The high density neural probe, including 1000 9 $\times$ 9 μm^2 electrodes. Scale bar: 50 μm [64]. (d) The top-down SEM image of recording area with four columns close-packed electrodes. The arrow indicates the direction towards to the tip of the probe. Scale bars: 10 μm [64].

mammalian brain. The close-packed recording electrodes were able to record the electrical signals of single neurons from multiple recording sites, making the data analysis easier. To date, NeuroNexus Inc. has made the Michigan probe available for commercial production. The standard probes are utilized in labs all over the world for single-unit and multi-unit neural recordings and stimulations.

The Utah array

The Utah array is another popular penetrating MEAs that has been widely used in neural recording. The Utah array is a silicon-based microneedle array that used to stimulate and record from cortical neurons [65]. When compared to the Michigan probe, the Utah array has larger coverage area and was able to map

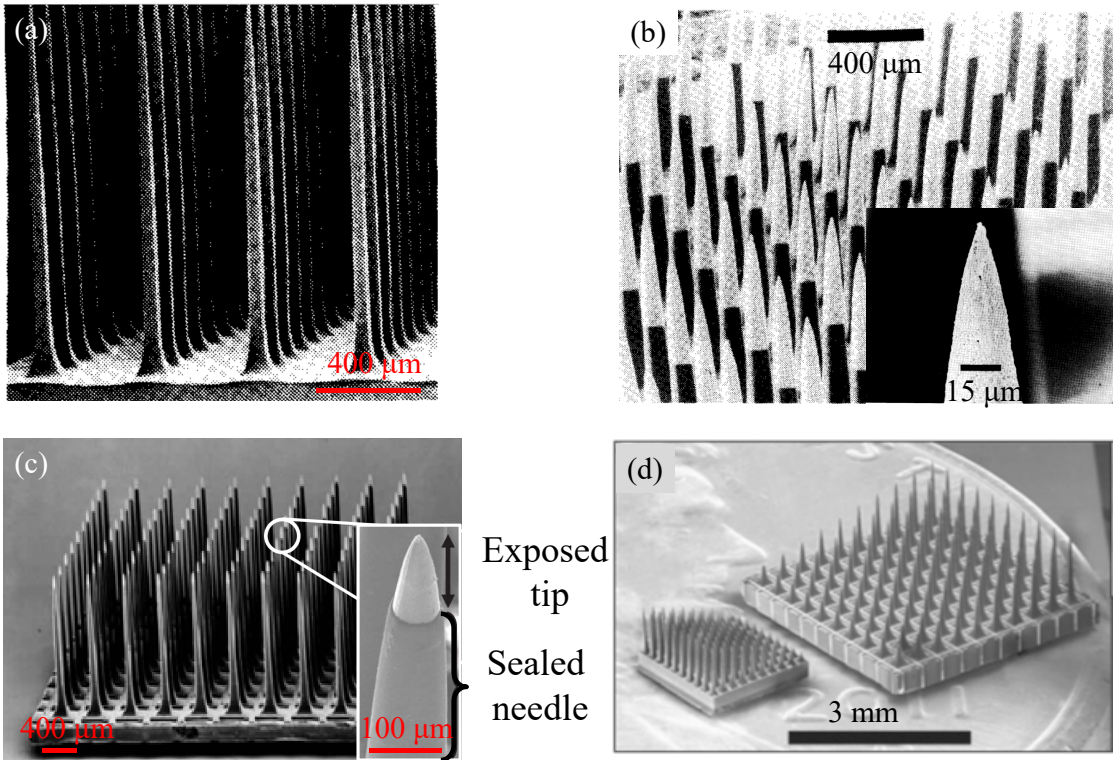

FIGURE 2.6: SEM images of different types of Utah array. (a) The SEM image from Campbell et al. Scale bar: 400 μm [65]. (b) The close-up image of silicon-based Utah array. Scale bar: 400 μm. The inset shows the tip of needle. Scale bar: 15 μm [66]. (c) The SEM image of parylene-coated Utah array. Scale bar: 400 μm. The inset shows the needle coated with parylene-C. The tip was exposed to record electrical signals generated by neurons. Scale bar: 100 μm) [67]. (d) The SEM image of high-density Utah needle array located on a US penny. The length of needles ranges from 300 μm to 800 μm. Scale bar: 3 mm [68].

the interactions between neighbouring neurons. Campbell et al. demonstrated a complete design of Utah array [66]. As shown in Fig. 2.6(a) & (b), this silicon-based array consisted of a 4.2 mm $\times$ 4.2 mm $\times$ 0.12 mm silicon substrate and 100 sharpened silicon needles with 1.5-mm length. The array was connected to outer electronic circuits via wire bonding so that electrical properties could be characterized and then could be used to record signals from the neural tissue.

In the following decades, some advanced Utah arrays have been developed for different applications. When considering the biomedical microsystem, the material selections are really important since all the implantable devices should be biocompatible to biological tissues. Therefore, R Bhandari et al. developed an integrated system which combined the integrated circuits (IC) to the Utah array and the whole system was encapsulated with parylene-C, which was a widely used biocompatible material [67]. The SEM image of parylene-coated device is shown in

Fig. 2.6(c). The whole needles were coated by parylene-C film except for the tips of the needles which functioned as recording sites. Moreover, in order to record signals from sub-millimeter neural structure and small diameter nerves (<2 mm), the device with small recording sites was required. Wark et al. developed Utah needle array with approximately 10-μm recording sites [68]. As shown in Fig. 2.6(d), the whole array involved penetrating needles with lengths ranging from 300 to 800 μm so that the array could be used to fully understand more complex spatial neural interactions.

2.3 Technologies for optogenetics

Extracting electrical signals from neurons is one of the popular strategies in studying neural circuits. Furthermore, activating neurons via electrical stimulation is a conventional way to stimulate neural circuits [69]. However, electrical stimulation has no selectivity for neuron type, with all neurons in a certain volume being activated. It is also not possible to electrically inhibit neurons. Therefore, novel techniques such as optical regulation have been developed to achieve full control over neural activities, including activation and inhibition. This capability was firstly mentioned by Francis Crick in 1979 [70] when he considered light as a possible control tool in neural circuit analysis. However, the strategy to make neurons responsive to light was not available until optogenetic techniques were developed in 2007 [71]. Optogenetics is known as the combination of genetic neural modulations that make neurons express light-sensitive proteins in cell membrane and the optical regulations of neural activities. Those light-sensitive proteins are called opsins and they are embedded into the membrane to create light-sensitive ion pumps or ion channels. As a result, ions flow across the membrane and can be controlled by visible light, which leads to optical control of neural activities.

2.3.1 Opsins

Opsins are a group of light sensitive proteins and come in two different types [72, 73]. Type I opsins are seven-transmembrane-domain proteins produced from microbial opsin genes [74] and tpye II opsins are similar proteins to type I, but are mammalian counterparts [74].

The first identified opsin is the haloarchaeal proton pump bacteriorhodopsin (BR, Fig. 2.7) [75–77]. Once in low oxygen conditions, BR is highly expressed in the haloarchaeal membrane to pump the protons from the cytoplasm to the extracellular environment in response to light [77, 78]. Some other opsins have similar functions, and were identified later such as archaerhodopsin (Arch). These light-gated proton pumps respond to green or yellow light (wavelength is from 500 nm to 600 nm) by pumping protons out of cells [79]. Halorhodopsin (HR), a light-activated chloride pump, was then discovered in archaebacteria in 1977 [80]. The operating principles of HR are similar to the ones of BR. When HR is expressed in the cell membrane, it will pump chloride ions into the cytoplasm from the extracellular environment as a response to yellow light (wavelength is about 570 nm) [81]. In the following decades, channelrhodopsins (ChR) were found in green algae [82]. ChRs are light-gated ion channels which allow ions to flow across the cell membrane. One of the most widely used channelrhodopsins is ChR2. When it is expressed in a neuron and exposed to blue light (wavelength is about 470 nm) [83], ChR2 is able to depolarize the neuron to trigger a spike in response to the blue light.

The control over ion transport across the membrane presents two ways to manipulate neural activity: either to excite neurons or inhibit neurons. To achieve those two goals, different types of opsins are used. ChR-2 is one of the most widely used opsins in neuron excitation [86]. It is a directly light-gated cation membrane channel which allows H^+, Ca^{2+}, Na^+ and K^+ flow in and out across the membrane as a response to the blue light. The neuron is activated when the membrane potential is beyond the threshold. When the membrane potential falls back to the rest level, the neuron is deactivated. According to the plot of membrane potential, a time constant called off-kinetics is used to characterize the neural deactivation. Typically, ChR2 provides about 10 ms off-kinetics. In order to achieve higher expression level, some improvements have been made by genetically engineering ChR2. For example, introduction of the H134R mutation into ChR2 offered about two-fold slower off-kinetics (18 ms) [74], but higher sensitivity to light. Another variant of ChR2 is called Chronos, which is a new blue and green light-drivable channelrhodopsin [87]. It has a short deactivation time constant (about 3 ms), so that it can generate spikes as a response to light with a frequency of 60 Hz [87]. There is also a new red light drivable variant called Chrimson. It shows a red-shifted absorption spectrum (peak at 590 nm) and allows neurons to be activated by short light pulses (5 ms) [87] . In addition, Chrimson may achieve precise

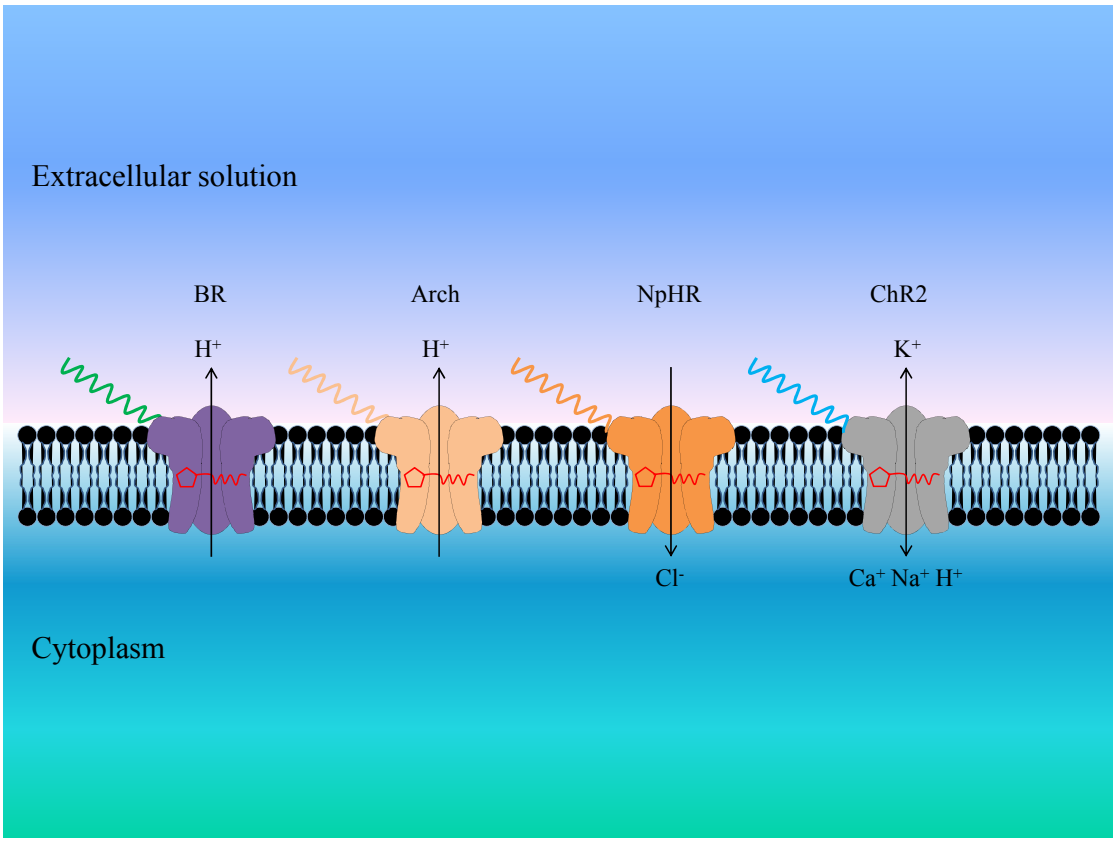

FIGURE 2.7: Basic properties of optogenetic tools. From left to right: bacteriorhodopsin (green light), archaerhodopsin (yellow light), halorhodopsin (yellow light) and channelrhodopsin-2 (blue light). The delivered ions and ion flow pathway are indicated [79, 84, 85].

temporal experiments in deeper brain regions where blue light is scattered.

For neural inhibition experiments, the light-driven chloride ion pump, halorhodposin (NpHR), and light-driven proton pump archaerhodopsin (Arch) are the most widely used opsins. The peak absorption of NpHR is at about 590 nm and the off-kinetics is about 4.2 ms [88]. Both Arch and its variant ArchT have a deactivation time constant of 9 ms and the variant ArchT improved the light sensitivity (more than 3 times) [74]. To further improve the light sensitivity of optogenetic tools, the light-gated anion channel rhodopsins (ACRs) are introduced to provide efficient membrane hyperpolarization and neuronal silencing through light-gated chloride conduction [89].

2.3.2 Opsin expression

When opsins are expressed in neurons, those neurons become light sensitive and are able to respond to the corresponding light stimulation. Several approaches, such as viral delivery, transgenic mouse generation and in utero electroporation can be utilized to introduce opsins into neurons [90, 91]. Viral delivery is a method that uses viruses as carriers to deliver opsins into neurons. Viruses such as adeno-associated viruses (AAV) and lentiviruses have been widely used in recent studies and opsins delivered via AAV can be introduced not only in mice, but also in other species such as rats and non-human primates [92–95]. Moreover, in order to make viruses target specific types of neurons, the opsin gene is inserted in the neighbouring region of placed sites that undergo genetic recombination. Recently, Cre recombinase is one of the most commonly used recombinases for genetic recombination [96, 97]. When the AAV virus with opsin gene is injected into the Cre mouse, it recombines and then enables opsin expression only in the neurons that express Cre recombinase [98–101]. Chan et al. have shown that the viruses can be injected into multiple regions in the brain at once by using multipleinjector arrays [102]. Therefore, opsins could be expressed in different brain regions and can be used to map neural circuits. An alternative opsin expression method, that avoids the use of viruses, is to use a transgenic animal to carry optogenetic construct with a site-specific recombinase [103]. Therefore, the viral expression of opsin is not required due to the expression of the particular Cre in the animal. All the described methods can be used to make large population of neurons respond to light stimulation. To target the single neuron, electroporation is an option to introduce the opsin gene into an individual neuron. As mentioned by B Judkewitz et al., a micropipette is placed close to the targeted neuron. Then a train of negative voltage pulses (e.g. -12 V) is applied to force neural membrane to be permeable for the transfection [104].

2.3.3 Development of optogenetic devices

In order to optically stimulate neurons in a large volume, optogenetic techniques have been developed to modify the neurons and optogenetic devices have been designed to introduce light to the target region. After genetically engineering light-sensitive proteins into neurons, the corresponding light should be delivered into brain tissue to activate them. One of the most simple and common strategies

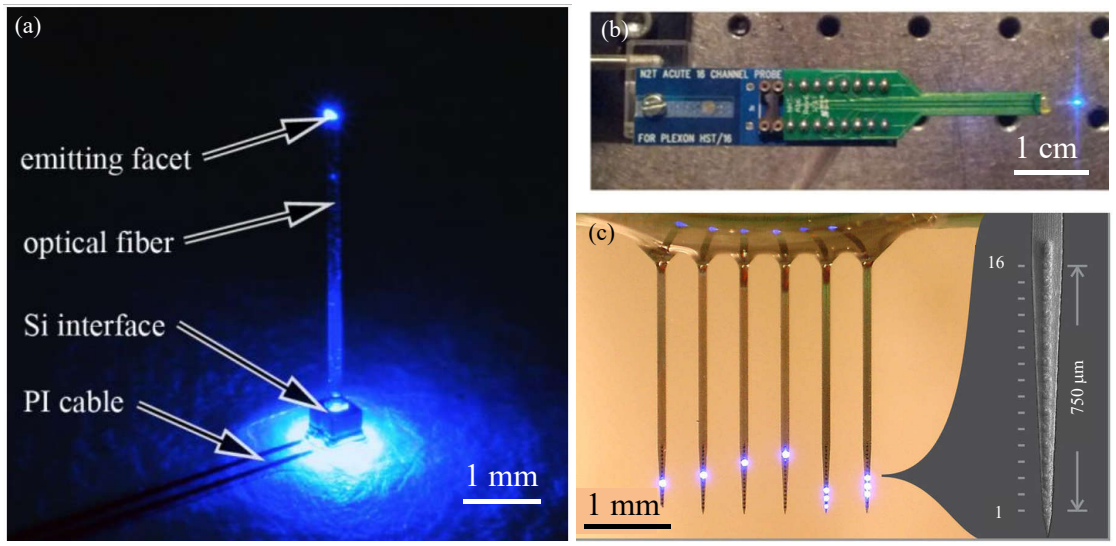

FIGURE 2.8: Images of different optogenetic devices. (a) The integrated system driven by a current of 20 mA. Light coupled from μLED delivered to the facet of fiber. Scale bar: 1 mm [105]. (b) McAlinden et al. demonstrated that final device mounted onto a printed circuit board (PCB). Scale bar: 1 cm [106]. (c) 6- shank μLED probe with 16 μLEDs per shank. The inset on the right: a SEM image of one shank. Scale bar: 1 mm [107].

is to use fibre optic cannula to deliver light into deep region of brain tissue [91]. In 2014, Pisanello et al. have developed an approach to couple light into the brain by using tapered optical fibres [108]. The tapered optical fibres enable spatial control over the light beam, resulting in large illumination volume.

However, the light was delivered via optical fibres and the light sources were usually lasers which are bulky and expensive [91, 109, 110]. The behaviours of subjects were often limited by the optical fibres. Therefore, to overcome the drawback, a μLED array is used as a light source to be coupled directly to the cannula to allow more animal movement [111]. In the following decades, the development of micro-structured light emitting diodes (μLEDs) makes it available in optogenetics. Initially, the devices consisted of a simple μLED mounted on a polyimide waveguides (Fig. 2.8(a)) [105]. In order to achieve optical stimulation with high spatial resolution, multiple μLEDs have been integrated together to enable patterned stimulation, which provide two-dimensional neural activation with sufficient irradiance into cultured tissues [112, 113]. However, those μLED arrays with planar structure are unable to deliver light into deep brain region to stimulate neural circuits. Therefore, some advanced μLED-based optogenetic devices have been developed in recent years. A probe that contained independently activated μLEDs was reported by McAlinden et al. and used to activate neocortical neurons *in vivo*

(Fig. 2.8(b)) [106]. The device had one tapered shank with 5 mm length and the tip was about 1 mm long and 150 μm wide. The shank contained four μLEDs which emitted at 450 nm wavelength with an irradiance of up to 2 W/mm^2 at the LED surface. An advanced LED probe was developed afterwards to achieve deep stimulation with complex patterns. Scharf et al. reported a high-density LED probe consisted of 96 individually addressable μLEDs on 6 shanks and each shank had 16 μLEDs (Fig. 2.8(c)) [107]. Therefore, the probe could cover a large volume of tissue at deep region of brain and deliver light in different patterns with cellular-scale resolution. However, extra recording probes are still required to extract neural responses since there were no recording sites on the LED probes. Due to the possibility to integrate recording sites onto the LED probe, the recording sites were fabricated around the μLEDs so that the neurons could be optically controlled and the spikes could be recorded [114, 115].

In this thesis, I designed, fabricated and characterised two novel devices to investigate information flow in biological neural networks. One is a penetrating microelectrode array and the other is the μLED coupled glass optrode array. The former is used for neural recording and the latter is used for optical stimulation. The penetrating microelectrode array was designed so that it could record neural activity in brain tissue that has been sliced during preparation (a common technique in neuroscience when accessing deep structures in the brain). This is required in order to access the healthy network of neurons beneath the sliced surface and to achieve good neural recordings. Moreover, the density of electrodes is required to be high to simplify the signal sorting and allow neuron identification. As a result, the penetrating microelectrode array presented here includes 61 electrodes with high spatial density (350 electrodes/mm^2). Each electrode is designed to be 200 μm high so that it is able to reach the neurons beneath the damaged surface of sliced tissue. The device was fabricated on a silicon wafer platform using semiconductor fabrication techniques

On the other hand, for optical stimulation, the main difficulty is coupling light into the brain which strongly scattering the blue light needed for optogenetic experiments. Therefore, in this thesis, a customized μLED array was designed, fabricated and integrated with an optical version of the well-known Utah electrode array. The direct integration of the light sources on to the Utah glass needle array removes the need for external optics. This produces a compact, lightweight

device capable of spatiotemporal optical stimulation of the primate cortex during behavioural studies.

The μLED arrays were also fabricated using semiconductor fabrication techniques and so this is introduced in the next chapter.

2.4 Summary

In this chapter, a brief introduction of neuron is firstly given and then followed by the overview of the approaches that used to fully understand the functions of neurons. Two main strategies are used recently to study neurons: one is to study the information flow in the neural circuits via analysing the electrical signals (spikes) recorded from neurons and the other one is to study the connections between brain function and neural responses via precisely control on neural behaviours (optical modulation). Devices that used in electrophysiological recordings and optogenetics are demonstrated in section 2.3. In the next chapter, modern semiconductor fabrication techniques used to produce electrical recording devices and optogenetic devices will be introduced.

Chapter 3

Experimental semiconductor fabrication techniques

Throughout this thesis, semiconductor microfabrication techniques have been used to develop new electrophysiological and optogenetic devices. These devices will be used to study the information flow in neural circuits. The initial materials for fabricating these devices are silicon and gallium nitride (GaN). In modern semiconductor fabrication, silicon is a well-known substrate material which is widely used in different types of semiconductor devices. GaN is also widely used for light-emitting diode structure and power transistors. It can be grown on different substrates (for example, sapphire or silicon) depending on the application. In this chapter, the wafer material is introduced (section 3.1), then typical semiconductor fabrication techniques are detailed including material deposition (section 3.2), pattern definition (section 3.3) and pattern transfer (section 3.4). Finally, additional steps (section 3.5) are introduced to the fabrication process for the purpose of improving the fabrication yield and the device performance.

3.1 Materials used in semiconductor fabrication

The fabrication processes of silicon have been comprehensively developed in the past decades. Silicon wafers are one of the most widely used material in semiconductor fabrication. In this project, silicon serves as a substrate to support the features of a penetrating microelectrode array.

The material used to produce GaN-based LEDs has been developed over the last 3 decades. The first LED was invented by the British experimenter Round using a crystal-metal-point-contact structure fabricated from silicon carbide (SiC) in 1907 [116]. As a result, a yellow light was generated when the SiC crystal was touched by a metal electrode. In the following decades, a detailed investigation on the luminescence phenomenon of LEDs was reported and many other materials such as II-VI semiconductors were used for LED fabrication. In the 1950's, III-V materials were demonstrated to be another option for LED fabrication [117]. Therefore, LEDs with different emission wavelengths have been developed from the middle of the 1950's. In 1962, the first infrared (IR) LED (wavelength $\approx$ 870 nm) based on gallium arsenide (GaAs) was reported by Hall et al. In the same year, General Electric Corporation provided the first commercial red LED based on gallium arsenide phosphide ($GaAs_{1-x}P_x$) [118]. $GaAs_{1-x}P_x$ is a semiconductor alloy of GaAs and gallium phosphide (GaP) and the fraction x in the formula indicates that there are different composition ratios between GaAs and GaP. The value is adjustable depending on the targeted emission wavelength. To extend the spectra of LEDs, different semiconductor materials and their alloys have been used in the following years. Indium gallium nitride ($In_xGa_{1-x}N$) is chosen for designing ultraviolet (UV), blue and green LEDs; GaP is for green and yellow LEDs; aluminium gallium indium phosphide (AlGaInP) for yellow, orange and red LEDs and aluminium gallium arsenide (AlGaAs) is for red and IR LEDs [119]. In this project, the blue μLED array is fabricated from $In_xGa_{1-x}N$ wafer.

3.1.1 Categories of semiconductor

According to the solid-state energy band theory, the energy band structure in the semiconductor crystal is defined by the periodic atomic arrangement. The energy band structure can be visualized as having a valence band and a conduction band separated by a bandgap, which is a forbidden energy region. There are two general types of semiconductors: one is direct bandgap semiconductor such as GaAs and GaN (Fig. 3.1(a)) and the other one is indirect bandgap semiconductor (Fig. 3.1(b)) such as Si. As shown in Fig. 3.1, the energy of the valence band and the conduction band can be plotted versus the crystal momentum of electrons and holes. The minimum in the conduction band and the maximum in the valence band of a direct bandgap semicondutor have the same crystal momentum (κ). On the other hand, the indirect bandgap semiconductor has a conduction band

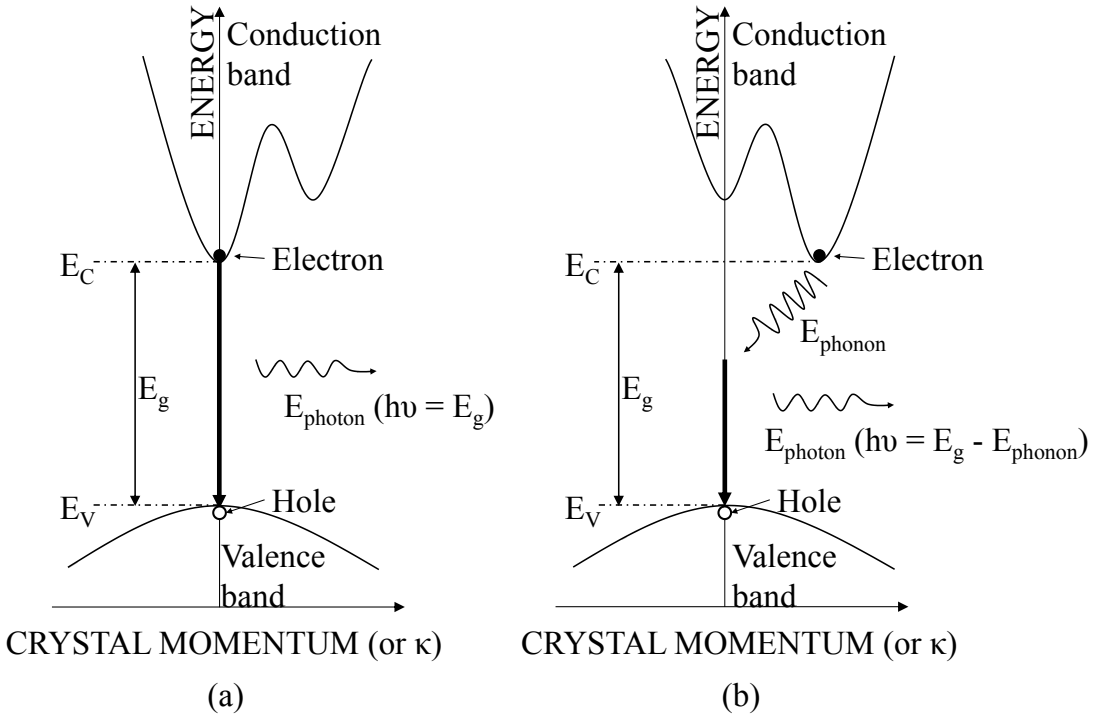

FIGURE 3.1: The band structure of (a) direct bandgap semiconductors and (b) indirect bandgap semiconductor. The related band-to-band transition of electrons in the direct bandgap semiconductor and the indirect bandgap semiconductor is also demonstrated. After [120].

minimum and a valence band maximum for the different crystal momentums. As a result, in the direct bandgap semiconductor, an electron can recombine with a hole without a change in κ value and the recombination will generate a photon with with specific wavelength (λ). The relationship between the wavelength of emitting photon and the bandgap can be written as:

$$E_g = E_C - E_V \approx h\nu = \frac{hc}{\lambda} \tag{3.1}$$

where E_C represents the minimum energy of the conduction band, E_V represents the maximum energy of the valence band, h is the Planck's constant and c is the speed of light in vacuum. However, in the indirect bandgap semiconductor, a lattice vibration (phonon) is required to achieve the electron-hole recombination. Consequently, the probability of the band-to-band transition in the direct bandgap semiconductor is higher than that in the indirect bandgap semiconductor. Therefore, the efficiency of LEDs fabricated from the indirect bandgap semiconductor is lower than the ones fabricated from the direct bandgap semiconductor.

Generally, the semiconductors without impurity atoms and lattice defects in the crystal are called intrinsic semiconductors [121]. In intrinsic semiconductors, the number of generated free electrons in the conduction band is equal to the number of free holes in the valence band. Therefore, the intrinsic semiconductors are overall neutrally charged and have a relatively low conductivity. In order to improve the conductivity of semiconductors, some impurities called dopants can be induced into the semiconductors. This process is known as the doping process. For example, when adding a group V element (e.g. phosphorus) to silicon, four out of five valence electrons will be used to form the covalent bonding between silicon atoms and phosphorus atoms. As a result, the fifth electron is left and can be elevated to the conduction band, leaving the positively charged phosphorus ion fixed in the silicon. The electron then can move through the crystal to generate a current when adding a small amount of energy. Consequently, this type of dopant is called donor and the doped material is referred to as an n-type semiconductor. If a group III element, such as boron, is added to silicon, three covalent bonds will be formed and one covalent bond will be left empty since the group III element only have three valence electrons. As a consequence, the electrons can occupy the empty position in the covalent bond, leaving the boron ions negative charged. When the empty positions in the covalent bonding are occupied by the electrons, the valence electron positions will become empty . The boron ions become negatively charged since they "accept"the electrons and those empty positions can be referred to as holes. Therefore, this type of dopant is called acceptor and the doped material is referred to as a p-type semiconductor.

3.1.2 P-n junction

When an n-type semiconductor is brought into contact with a p-type semiconductor, a p-n junction is formed which is the basic component of a μLED device. For p-type semiconductors, the majority carriers are holes and the minority carriers are electrons. The majority carriers in n-type semiconductors are electrons and the holes are minority carriers (Fig. 3.2(a)). When no external voltage is applied across the junction, there are large density gradients for both electrons and holes. Therefore, the electrons in the n-type region diffuse to the p-type region and the holes in the p-type region diffuse to the n-type region. As a result, a depletion region (as noted in Fig. 3.2(b)) is created around the interface between p-type and n-type semiconductor due to the diffusion of the electrons and the holes. Across

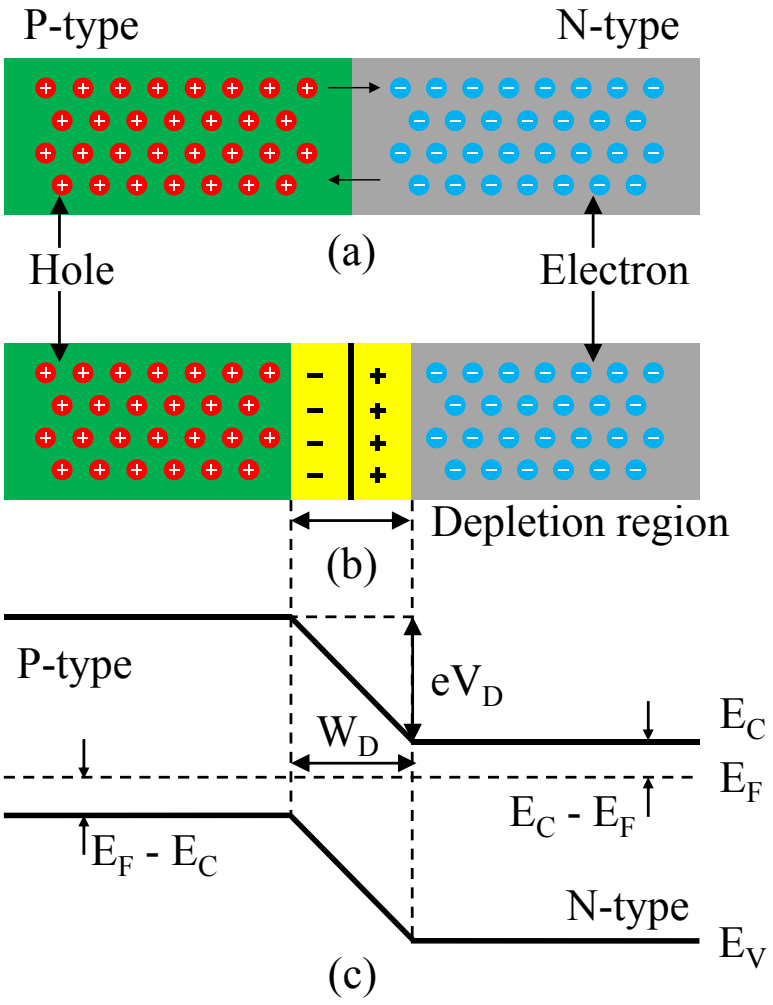

FIGURE 3.2: (a) Simplified geometry of a p-n junction. (b) P-n Junction under zero bias, demonstrating the depletion region. (c) Band structure of a p-n junction under zero bias.

the depletion region, a potential is generated by the positively charged donors in the n-type semiconductor and the negatively charged acceptors in the p-type semiconductor and inhibits the further diffusion of free carriers. This potential is known as the diffusion voltage (V_D) and it can balance the diffusion of carriers in a thermal equilibrium state. According to the band diagram shown in Fig. 3.2(c), a barrier is formed when the n-type semiconductor and the p-type semiconductor are in contact and it can be written as eV_D, where e is the elementary charge.

When an external voltage is applied as a reverse-bias voltage, the diffusion voltage across the depletion region will be increased and the diffusion of free carriers will be further inhibited. On the contrary, when apply a forward-bias voltage, the potential across the depletion region will be decreased and more carriers will be injected into the depletion region (Fig. 3.3). Then the recombination of electrons

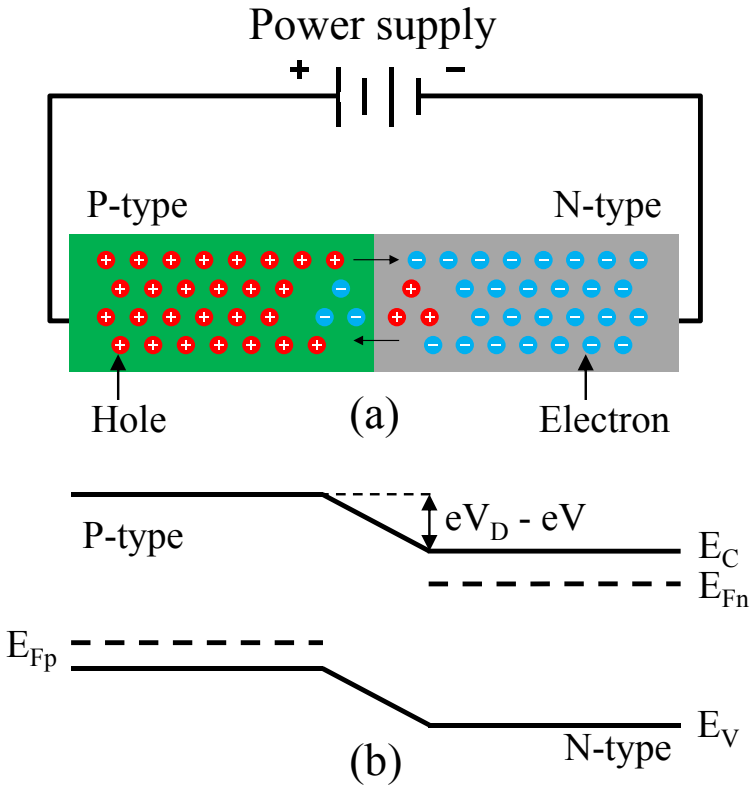

FIGURE 3.3: (a) P-n junction under forward-bias voltage. (b) Band structure of a p-n junction under forward-bias voltage.

and holes occurs and leads to photon generation. Therefore, a forward-bias voltage is needed to drive LEDs.

3.1.3 Heterojunction and quantum well structure

As discussed before, the p-n junction is formed by an n-type semiconductor and a p-type semiconductor. When assuming that the semiconductor material is homogeneous throughout the structure, the junction is called homojunction. On the other hand, if the two semiconductor materials have different bandgap energies, the junction is called heterojunction. As shown in Fig. 3.4, if a small-bandgap semiconductor is sandwiched between two larger-bandgap semiconductors (an n-type semiconductor and a n-type semiconductor respectively), the heterojunction then consists of two barrier regions and this junction structure is known as a double heterostructure. In the double heterostructure, the smaller-bandgap semiconductor is used for the active region and the larger-bandgap ones are used for the barrier regions. Consequently, when a forward-bias voltage is applied, the injected carriers are confined to the active region. This results in a higher carrier

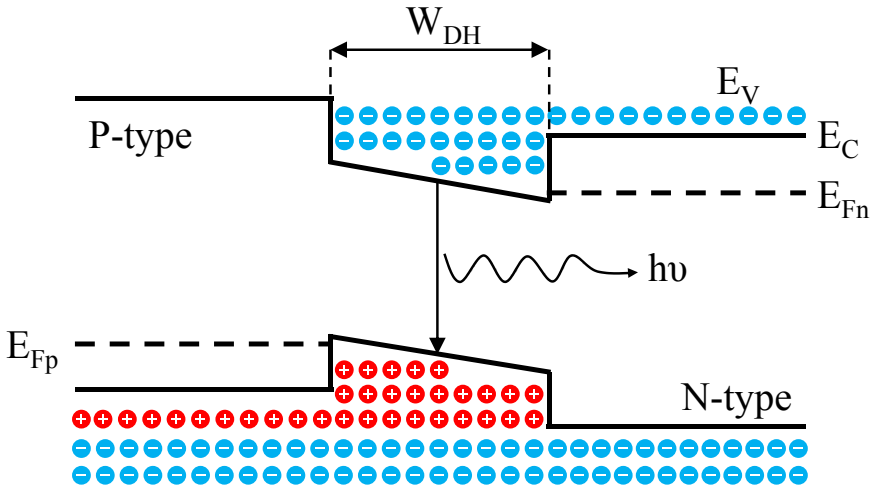

FIGURE 3.4: Band diagram of a double heterostructure under forward-bias voltage. After [122].

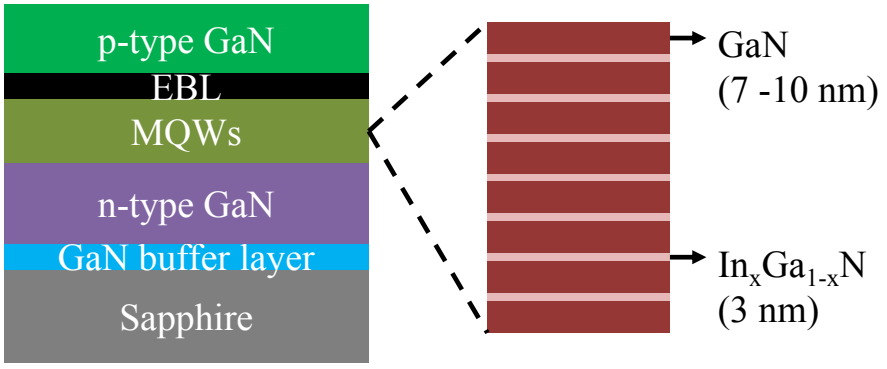

FIGURE 3.5: Typical structure of a commercial $In_xGa_{1-x}N$/GaN-based LED wafer grown on a c-plane sapphire substrate. The GaN is grown on the sapphire substrate and includes p-type GaN, electron blocking layer (EBL), multi-quantum well (MQW) region, n-type GaN and GaN buffer layer. The MQW region comprises $In_xGa_{1-x}N$ layer (3 nm) and GaN layer (7 - 10 nm).

density in the double heterostructure. Therefore, all the high-performance LED devices are fabricated based on p-n heterojunctions.

When the width of the active region W_{DH} is small enough and the value of W_{DH} is comparable to the de Broglie wavelength of the carriers, the active region of the double heterostructure becomes a quantum well (QW). Since the width of the QW can be smaller than the width of the active region, the carrier density can be further increased by employing QW in the active region. Therefore, most μLED devices currently consist of several QWs in the active region and this type of active region is called multi-quantum well (MQW) region.

In this project, the wafer material used to fabricate μLED arrays is commercially

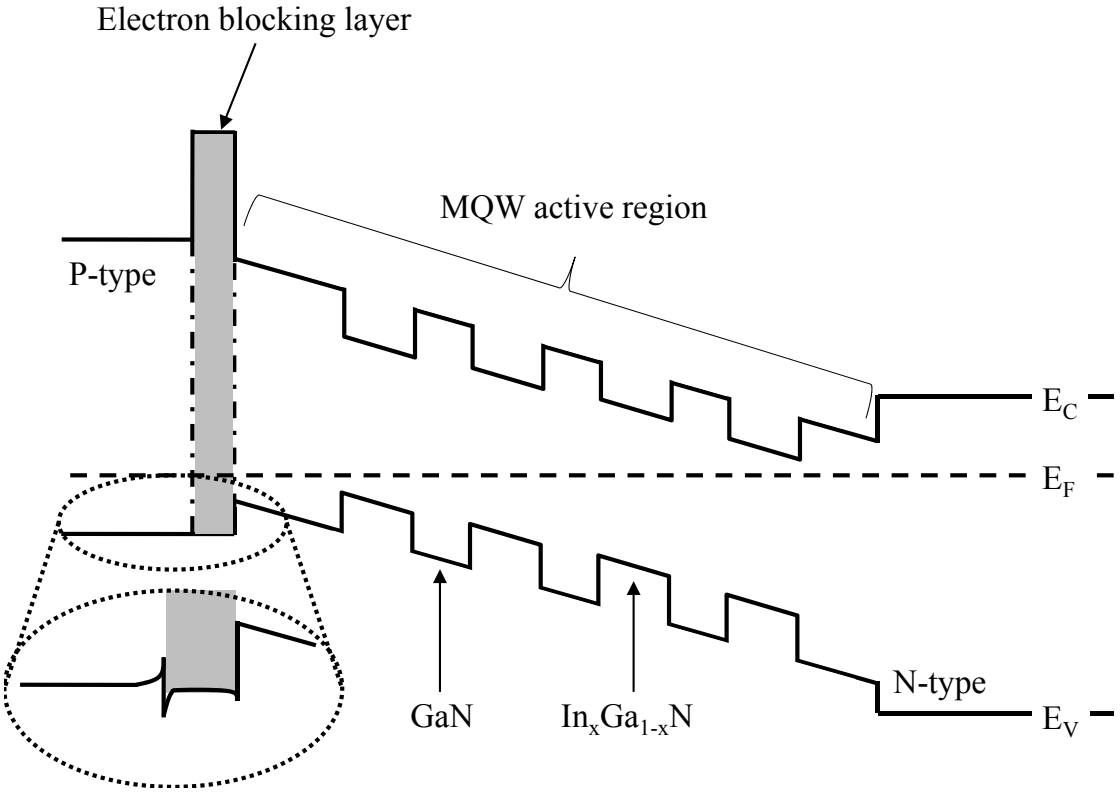

FIGURE 3.6: Simplified band diagram of $In_xGa_{1-x}N$/GaN under forward-bias voltage. The grey region is the electron blocking layer. The Al content in the electron blocking layer is higher than in the p-type GaN (highlighted by the inset). After [122].

designed and grown using epitaxial growth techniques. The whole structure is shown in Fig. 3.5. The $In_xGa_{1-x}N$/GaN-based LED wafer is grown on a c-plane sapphire substrate, which is approximately 300-μm thick. The MQW region comprises $In_xGa_{1-x}N$ layer and GaN layer. As mentioned previously, the fraction x in the formula indicates the ratio of indium/gallium. Therefore, the bandgap of compound can be tuned by varying the amount of indium [123]. The combination of $In_xGa_{1-x}N$ and GaN is designed for high radiative efficiency light emission. The MQW region is normally covered by an electron blocking layer (EBL). Typically, the EBL layer is made of a p-type wider-bandgap $Al_xGa_{1-x}N$ ternary alloy so that it has higher bandgap energy. As a result, the electrons will not escape from the MQW region [122]. Fig. 3.6 demonstrates the simplified band diagram of the MQW region under forward-bias voltage.

3.2 Semiconductor fabrication techniques

Semiconductor fabrication is a series combination of different process types used to produce integrated circuits (ICs) that are in everyday electrical and electronic devices. Normally, the entire fabrication process starts from the wafer preparation to the device packaging. In this project, I mainly focused on the device fabrication process and the whole fabrication process normally fell into three categories: material deposition/growth, pattern definition and pattern transfer.

3.2.1 Material deposition/growth

Material deposition/growth is a process that grows, coats or transfers a material onto the sample. Available techniques include physical vapor deposition (PVD) and chemical vapor deposition (CVD). Additional deposition strategies such as thermal oxidation, electroplating and epitaxy are also commonly used in semiconductor fabrication.

3.2.1.1 Physical vapor deposition

Physical vapor deposition (PVD) is a process used to transfer material onto the sample without a chemical reaction. The material is released from a solid source and transferred as a gas or vapour to the sample surface to condense as a thin film with controlled thickness. Two common PVD techniques used in semiconductor fabrication process are sputtering and evaporation.

Sputtering

Sputtering deposition is a process that deposits material onto the sample surface by ion bombardment. The schematic of sputtering deposition is shown in Fig. 3.7(a). The material source is mounted on the plate (cathode), which is negatively charged. The sample is placed on the positively charged electrode (anode). An electrical field is generated between the cathode and anode due to the DC voltage. Therefore, the ejected atoms such as argon (Ar) are ionized at low pressure and accelerated towards the material source with high energy (typically up to mega electronvolt, MeV) [124]. Material atoms then are released by ion bombardment from the source and deposited onto the sample surface as a thin film. In this

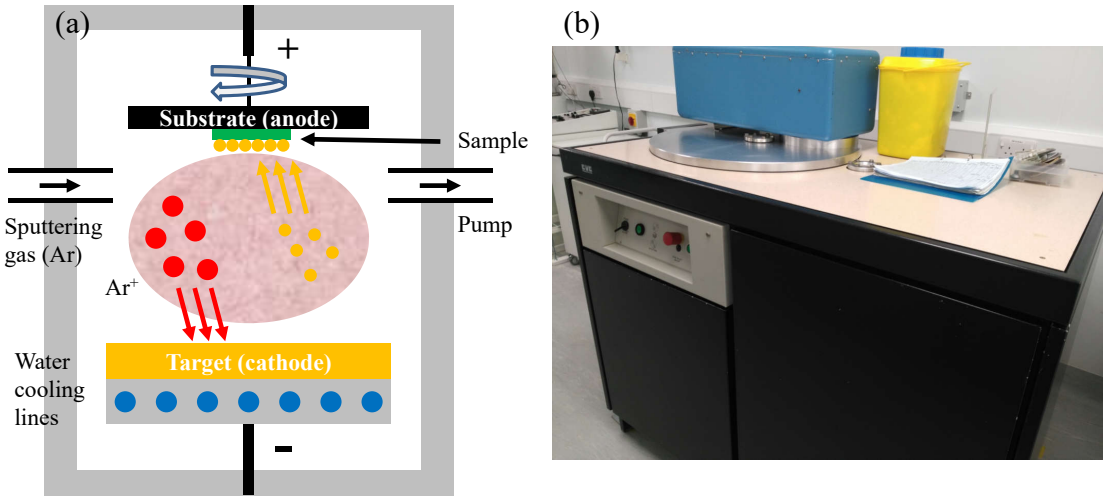

FIGURE 3.7: (a) Schematic diagram of sputtering deposition. The sputtering gas (Ar) is introduced into the chamber and ionized at low pressure. Ar^+ ions then bombard the target surface to release the target atoms. Those sputtered atoms are deposited to the sample surface to form a film with controlled thickness. The cathode is cooled down continuously by water cooling lines due to the heat generation of bombardment. (b) CVC sputtering system used in this project.

project, sputtering deposition is accomplished in the CVC sputter system which is shown in Fig. 3.7(b).

Evaporation

Evaporation is another physical deposition process. As shown in Fig. 3.8(a), the sample is placed inside the process chamber, where the material source is also located. During the deposition, the material source is heated to the point where it starts to melt and evaporate. Molecules subsequently condense on the sample surface. Two main methods are used in evaporation processes to heat up the material source: one is using electron beams to provide a local heating on the material source and the other one is applying high current to electrically heat up the material source. As a result, there are two popular evaporation technologies, which are electron-beam evaporation and resistive evaporation. These technologies only differ in the heating strategies. In this project, an electron-beam evaporator is used. The electron beam is generated from tungsten filament and is targeted to the target materials under the magnetic field. In order to ensure the molecules evaporate freely, the process chamber should be maintained at low pressure and the thickness of condensed film is measured by the crystal monitor. At the meantime, the platform of material source is continuously cooled down by the water cooling

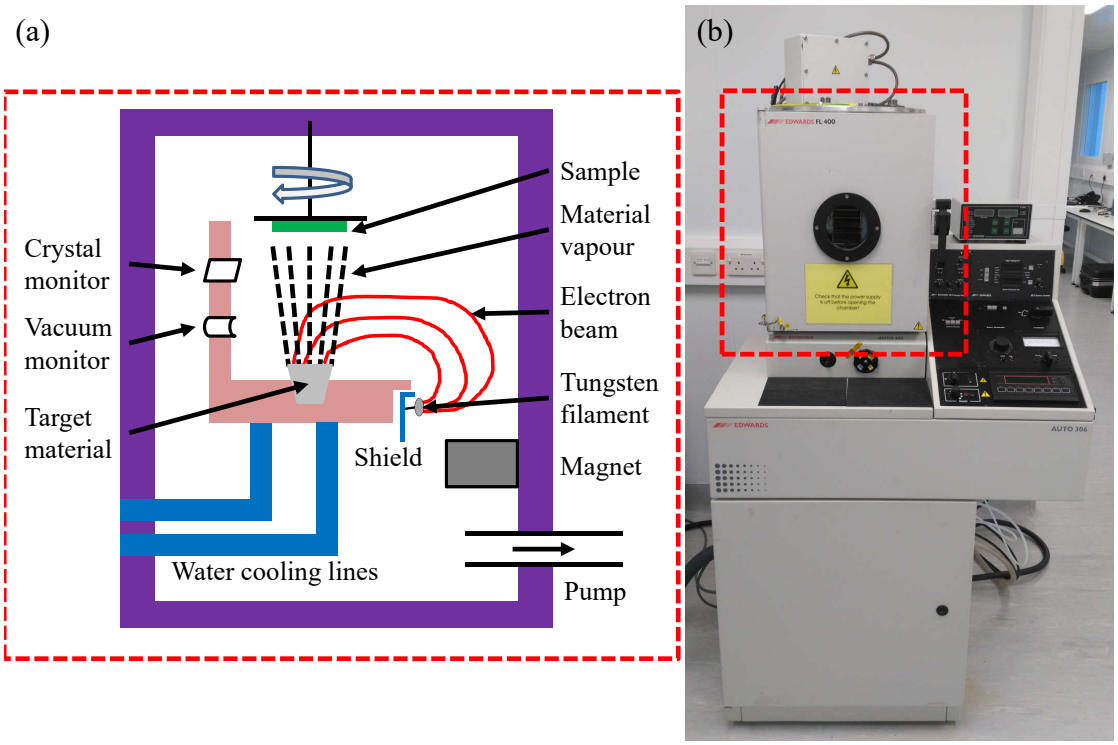

FIGURE 3.8: (a) Schematic diagram of electron-beam evaporation. Both the sample and the material source are located in the process chamber. The electron beam is generated from the tungsten filament and targeted to the material source under the magnetic field. The material source is heated up and starts to melt and evaporate. At the meantime, the platform of the material source is cooled down by the water cooling lines. The vapour of the material source is then condensed onto the sample surface as a uniform film. The thickness of the film is monitored by the crystal monitor. (b) Edwards E306 electron-beam evaporator used in this project. The processing chamber is highlighted by red box.

lines. The evaporation system used in this project is Edwards E306 electron-beam evaporator and shown in Fig. 3.8(b).

3.2.1.2 Chemical vapor deposition

Chemical vapor deposition (CVD) is another material deposition process to form thin film on the sample surface via chemical reaction. In general, gaseous material sources are supplied into a reaction chamber, where the sample is also placed inside. A chemical reaction then takes place between the gases and produces a solid material on the sample surface. The two main CVD technologies used in microelectromechanical system (MEMS) fabrication are low pressure CVD (LPCVD) and plasma enhanced CVD (PECVD). The schematics of both CVD reaction chamber

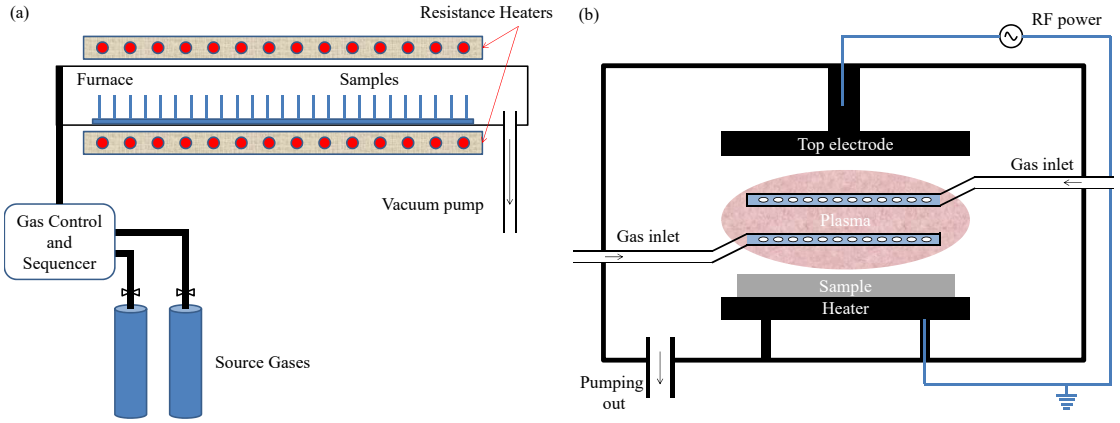

FIGURE 3.9: (a) Schematic of LPCVD reaction chamber. The gaseous materials chemically react with each other in the furnace and 25 wafers can be processed simultaneously. (b) Schematic of PECVD reaction chamber. The plasma is generated in the process chamber to enhance the chemical reaction between the gaseous materials.

are shown in Fig. 3.9(a) and (b) respectively. In principle, the LPCVD is able to produce films with good uniformity but the processing temperature is higher than 600 °C. The PECVD could be processed at a lower temperature (about 300 °C.) due to the extra energy supplied by the plasma. The LPCVD system is capable of double-sided deposition on about 25 wafers at a time and most PECVD systems could only achieve one-sided deposition on approximately 4 wafers at a time.

3.2.1.3 Additional deposition techniques

Except for the techniques mentioned above, thermal oxidation and electroplating are also widely used in semiconductor fabrication. The former is to deposit a dense silicon dioxide (SiO_2) layer on silicon (Si) substrate and the latter is to deposit thin electrically conductive materials such as platinum.

Thermal oxidation

Thermal oxidation is a simply oxidation process to form SiO_2 on silicon substrates in an oxygen rich atmosphere. Two basic schemes are used in thermal oxidation: dry oxidation and wet oxidation. Both oxidation processes take place between about 800 °C and 1100 °C.

Dry thermal oxidation results thin SiO_2 layer no thicker than 1000 $\mathring{A}$ on the sample surface and the whole process takes much longer time than wet thermal oxidation. Dry thermal oxidation has a very similar process to wet thermal oxidation. The

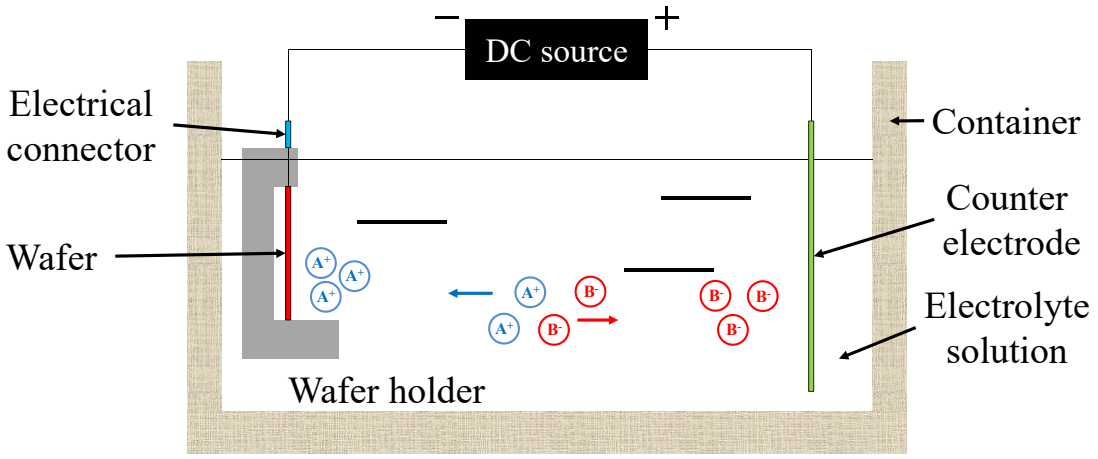

FIGURE 3.10: Schematic diagram of a typical electroplating setup. The sample is immersed into the electrolyte together with a counter electrode. The sample is negatively charged and the counter electrode is positively charged so that an electrical field is created between the sample and the counter electrode. A chemical redox process therefore happens and the positively charged ions (A^+) move towards the sample surface under the electrical field and form a solid film, while the negatively charged ions (B^-) move towards the counter electrode.

only difference is that dry thermal oxidation uses pure oxygen instead of steam to react with silicon. The reaction formula is given below:

$$Si + O_2 \rightarrow SiO_2 \tag{3.2}$$

Wet thermal oxidation is used to form thicker SiO_2 layer. The thickness of SiO_2 layer could be up to 2.5 μm. In order to avoid impurities, pure steam is used to react with silicon substrate and the reaction formula is given below:

$$Si + 2OH^- + 2H_2O \rightarrow SiO_2(OH)_2^{2-} + 2H_2 \tag{3.3}$$

However, the growth rate of SiO_2 in both dry and wet thermal oxidation is non-linear due to the oxygen diffusion into the silicon substrate. When the reaction takes place between the Si and oxidants, part of Si is replaced by SiO_2. If the thickness of SiO_2 layer is D, the thickness of replaced Si layer is $0.45D$ according to the molar volumes of both materials.

Electroplating

Electroplating is a process that deposits material onto the sample by applying electrical current. It is a common technique used in microelectrode array fabrication

process to form platinum black over recording sites. Typically, the sample is immersed into an aqueous solution (electrolyte), where a counter electrode (usually a platinum wire) is also located. During the electroplating process, an electrical potential is applied between the electrode on the sample and the platinum wire. As a result, a chemical redox process takes place in the solution, leading to a formation of a thin film on the electrode. A schematic diagram of a typical electroplating setup is shown in Fig. 3.10.

3.2.2 Pattern definition

Pattern definition is the first step in most fabrication processes. The most widely used technique in pattern definition is photolithography, which is used to form geometric patterns to the photosensitive materials, such as photoresist (PR). The basic photolithography process is shown in Fig. 3.11.

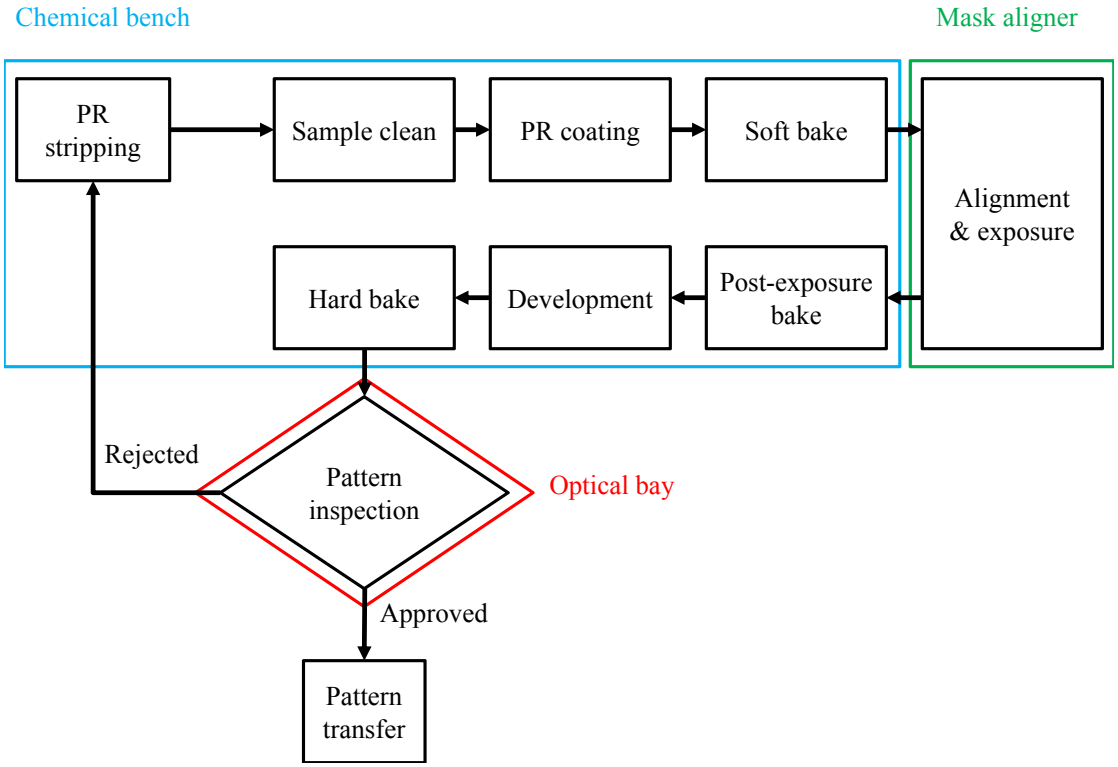

FIGURE 3.11: Flow chart of photolithography process. The sample is firstly prepared in chemical bench. A mask aligner is then used to perform alignment and exposure steps. Followed by the pattern inspection in optical bay to ensure the pattern meets the requirement.

Before photolithography, the substrate, or the wafer should be chemically cleaned. Any residuals and impurities may affect the quality of photolithography. After

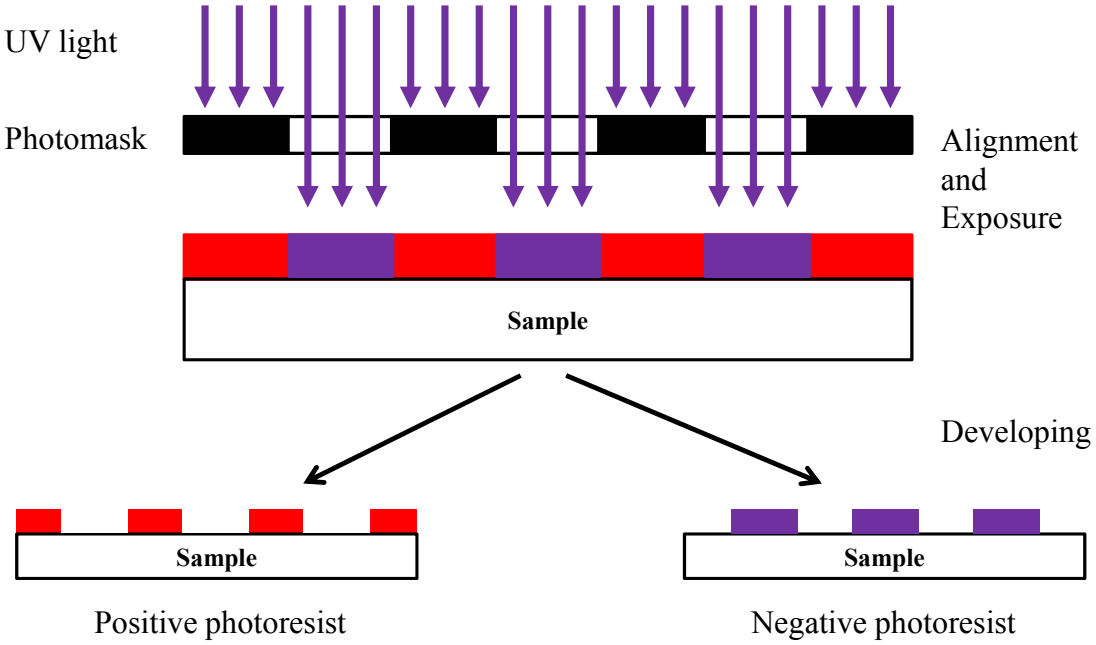

FIGURE 3.12: Patterning process with positive and negative photoresists. Based on the intrinsic chemical properties of photoresist, the exposed parts of positive photoresist will be dissolved during developing step. On the contrary, the exposed parts of negative photoresist will remain and the unexposed parts will be removed by developer solution.

cleaning, PR is applied, typically using a spin coating method, on to the substrate and then the sample is soft baked and cooled down to room temperature. In order to define patterns precisely, the alignment and exposure steps are performed in a mask aligner. Typically, between the exposure and development steps, a baking process called post-exposure bake is applied to avoid a standing wave effect that occurs during the exposure process. The standing wave is formed by the interference of incoming and reflected light. As a result, ridges can be found in the sidewall of photoresist pattern, which significantly affect the quality of the feature. The post-exposure bake is able to lead a diffusion of molecules in photoresist to smooth the sidewall. After the exposure step, the sample should be rinsed in a specific developer solution so that the patterns that have been defined with PR will be revealed. If the patterns are not reproduced as expected, the PR can be stripped and the sample needs to be chemically cleaned. Then the whole photolithography process should be repeated until the patterns are acceptable.

In the exposure step, the PR is exposed to the ultraviolet (UV) light through a photomask because the PR is sensitive to the UV light. The photomask includes clear patterns and opaque patterns based on the design of devices. The UV light is able to pass through the clear region but is blocked at the opaque regions.

The clear and opaque regions of photomask specifically depend on the types of PRs. In general, two main types of PRs are used in the semiconductor fabrication processes: negative PRs and positive PRs. Patterning processes with negative PRs and positive PRs are shown in Fig. 3.12 respectively. According to the nature of PR components, the chemical property of PR would be changed by the UV light during the exposure step. For negative PR, the exposed parts become insoluble in the developer due to the photochemical reaction. The unexposed parts, on the contrary, would be dissolved in the developer solution. For the positive PR, the exposed parts would be softened by the photochemical reaction and hence, are dissolved in the developer solution.

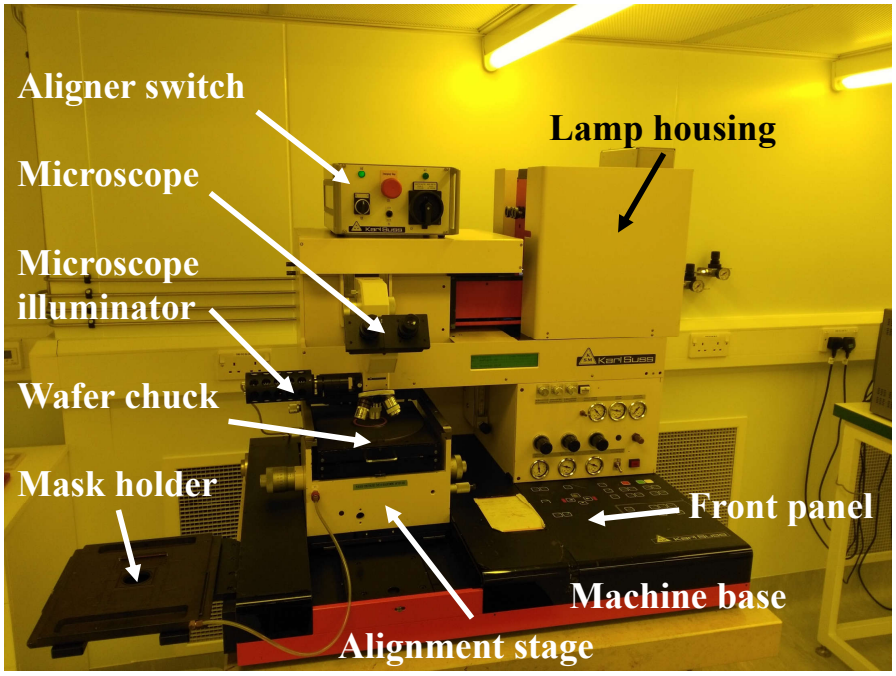

FIGURE 3.13: Photograph of Karl Suss MA6 Mask Aligner used for operation of alignment and exposure in the photolithography process. The exposure lamp source is located inside the lamp housing. The alignment is performed under the microscope while the photomask and the sample are placed to the mask holder and the wafer chuck respectively. The wafer chuck sit on the alignment stage so that the sample can be moved vertically and horizontally. Moreover, a rotation adjustment is also available for the sample movement. The buttons on the front panel are used to control the movement of microscope.

The photolithography process is achieved on a piece of equipment called mask aligner. In this project, a Karl Suss MA6 Mask Aligner (Fig. 3.13) is used. The mask aligner includes three main parts: lamp housing, microscope and alignment stage. The lamp housing is an enclosure where the exposure lamp source is placed. The microscope stage is used to visualise the alignment process. The alignment

stage includes three components: mask holder, wafer chuck and control panel. The photomask and the sample are put on the holder and chuck respectively; the control panel is the terminal to control sample x-y movement and θ adjustment. Due to the optical design in the mask aligner, the achievable minimum feature size is determined by the lamp wavelength and the numerical aperture of the optical system. Therefore, the ideal resolution R could be expressed as below:

$$R = k_1 \frac{\lambda}{NA} \tag{3.4}$$

where k_1 is a system constant and NA is the numerical aperture of the system. As shown in the equation 3.4, resolution R could be improved by either reducing lamp wavelength λ or increasing the numerical aperture NA. However, this will cause a reduction of the depth of focus DOF to the optical system. DOF is the distance around the focus in which a good resolution R of patterns is obtained. The DOF can be written as:

$$DOF = k_2 \frac{\lambda}{NA^2} \tag{3.5}$$

where k_2 is a system constant. According to the equation 3.4 and 3.5, there is a trade-off between resolution R and the depth of focus DOF. Therefore, it would be more challenging to achieve high-quality PR patterns with small feature size in the photolithography process. In this project, due to the multi-wavelength of the mercury short-arc lamp, the minimum feature size of PR patterns that can be achieved in this mask aligner is approximately 1 to 1.5 μm. In practice, this is challenging and a limit of 2 μm is more typical.

3.2.3 Pattern transfer

In previously sections, techniques to define patterns have been introduced. For a fabrication process, pattern transfer is the following step after pattern definition. Etching is a widely used technique to achieve pattern transfer. Two main types of etching process are used: dry etching and wet etching.

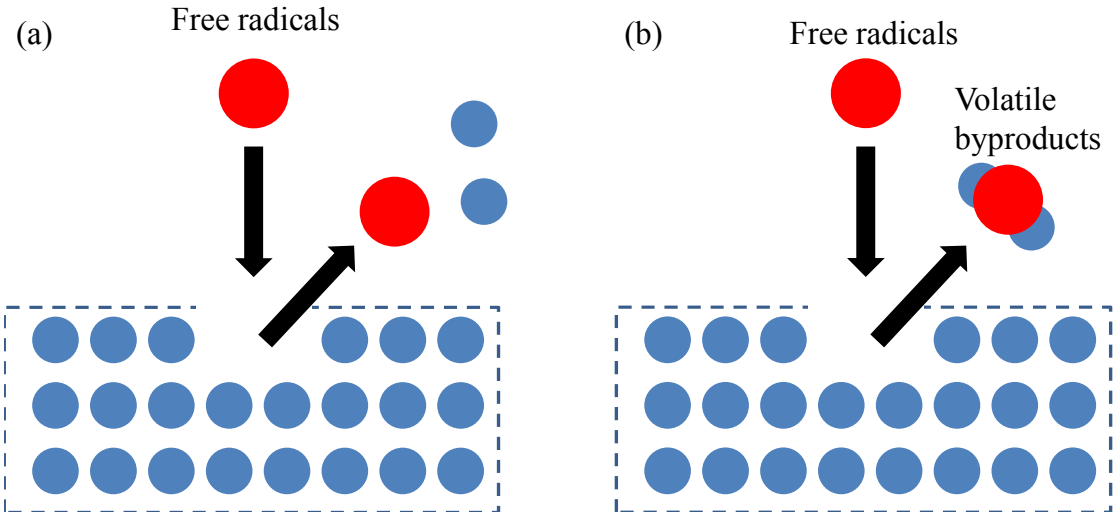

FIGURE 3.14: Schematic diagram of two types of dry etching process. (a) pure chemical reaction etching and (b) physical ion bombardment etching.

3.2.3.1 Dry etching

Dry etching is one of the pattern transfer techniques in semiconductor fabrication and is accomplished in a gaseous environment. There are two main types of dry etching processes: pure chemical etching and physical ion bombardment etching. Both etching processes are schematically shown in Fig. 3.14. In pure chemical etching, the materials are removed solely by the chemical reaction. The volatile byproducts would be produced during the chemical reaction between the materials and the chemical etchants.The etch rate of pure chemical etching strongly depends on the chemical reaction of the gaseous enchants and the materials. It is necessary to ensure that the byproducts formed from the reaction are volatile. If the byproducts are non-volatile, they may stay on the etched surface so that the further reaction may be influenced or even interrupted. On the contrary, there is no chemical reaction during the physical ion bombardment etching since the materials are removed from the sample surface by energetic ions. Therefore, the etching rate of physical ion bombardment etching is dependent on the flux and the ion energy.

The system used to achieve dry etch is called reactive ion etching (RIE) system. Typically, the RIE system consists of a vacuum chamber with a sample holder located on the bottom. Gas enchants could flow into the chamber via small inlets on the top of the chamber, and be pumped out by the vacuum pump system on the bottom of the chamber. When applying a strong radio frequency (RF)

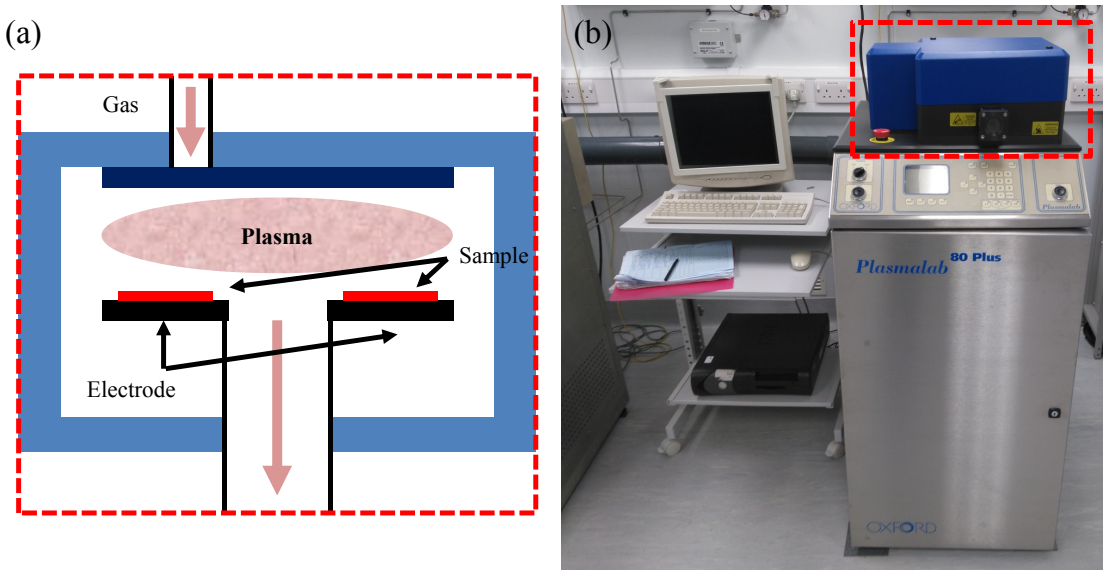

FIGURE 3.15: (a) Schematic diagram of RIE processing chamber. The gas enchants are introduced into the vacuum chamber via small inlets. When applying a electromagnetic field, the gas enchants will be ionized and then react with the materials on the sample surface. (b) Plasma 80 Plus RIE tool used in this project. The processing chamber is highlighted by red box.

electromagnetic field to the sample holder, the gaseous enchants could be ionized to etch the sample. A schematic diagram of the process chamber in a typical RIE system is shown in Fig. 3.15(a). The RIE system used in this project is Plasmalab 80 Plus supplied by Oxford Instruments and the system is demonstrated in Fig. 3.15(b).

Another type of RIE system is called an inductively coupled plasma (ICP) system, also widely used to achieve pattern transfer. In ICP systems, an extra RF magnetic field is applied in the coil to enhance the ionization. Therefore, higher plasma densities can be achieved in the ICP process chamber, resulting in higher etch rates and more isotropic etch profiles. A schematic diagram of the process chamber in a typical ICP system is shown in Fig. 3.16(a) and Fig. 3.16(b) shows the STPS Multiplex ICP system used in this project.

3.2.3.2 Wet etching

Wet etching removes materials using chemical solutions. During wet etching, a suitable selectivity between the mask material and the target material should be achieved and the selectivity is mainly determined by the environment temperature

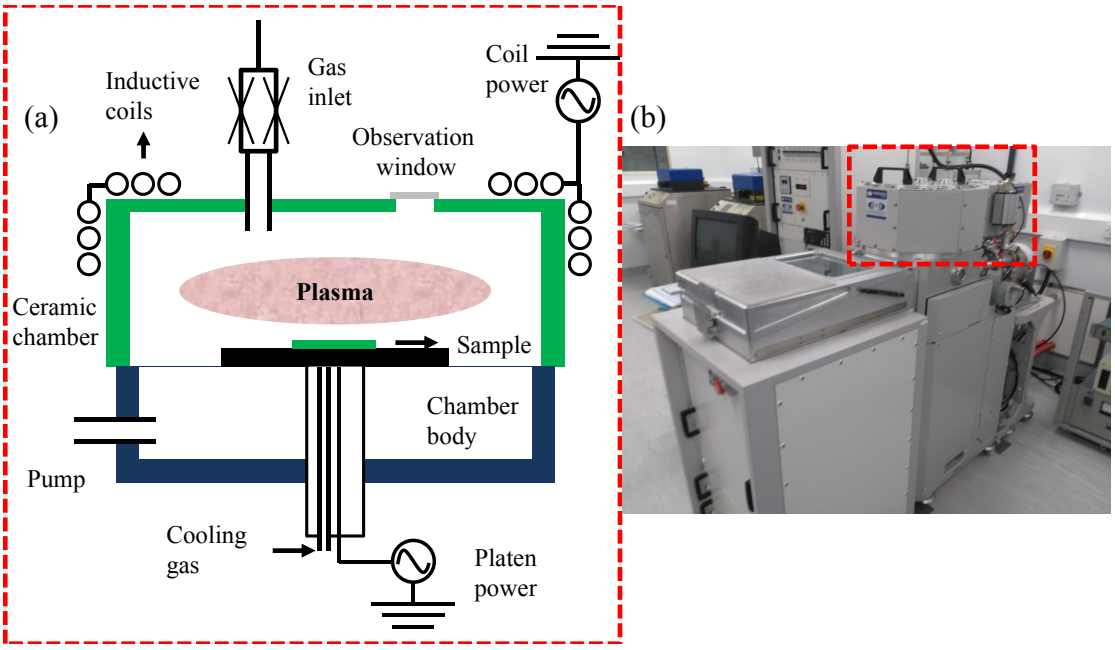

FIGURE 3.16: (a) Schematic diagram of ICP processing chamber. The gas enchants flow into the vacuum chamber via gas inlets on the top of the chamber. Then the enchants are ionized under the electromagnetic field. The ionization is also enhanced by the additional RF magnetic field so that the plasma densities are higher than the ones in RIE tools, resulting in higher etch rates and more anisotropic etch profiles. (b) STPS Multiplex ICP system used in this project. The process chamber is highlighted by red box.

and the concentration of chemical solution. Moreover, the etch rate of wet etching process also strongly depends on the temperature, concentration of solution and the crystallographic plane of materials. Besides, wet etching process normally produces an isotropic etching profile. Therefore, it is a challenge to achieve high-quality etching profile with small feature size via wet etching process. The processes of wet etch used in this project will be detailed in the next chapter.

3.3 Additional steps in fabrication process

In order to improve the fabrication yield and the device performance, some additional steps are applied: one is plasma ashing for photoresist striping and the other one is thermal annealing for creating a metal contact with low electrical resistance.

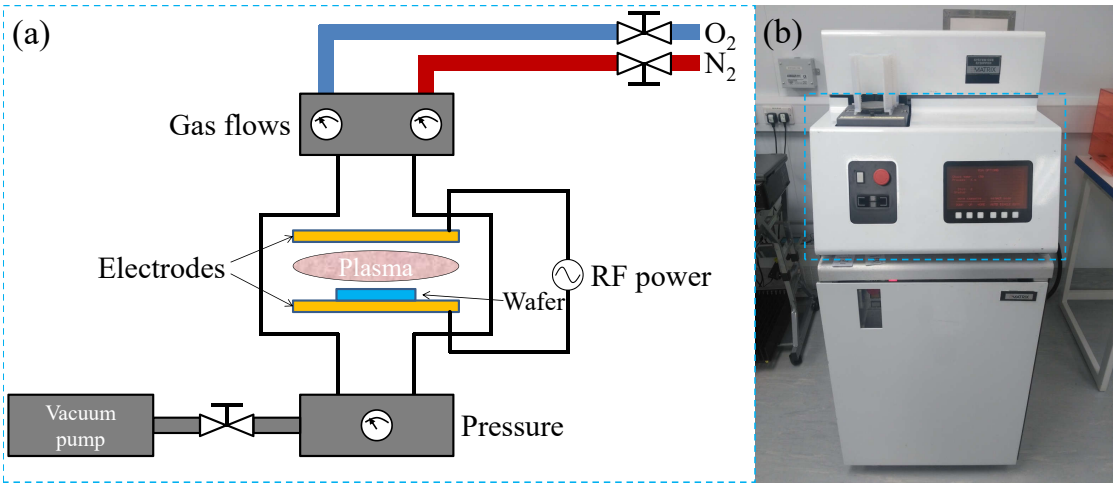

FIGURE 3.17: (a) Schematic diagram of the O_2 plasma asher system. The ionized gas mixture (O_2 and N_2) flows across the sample surface and the organic residuals (e.g. photoresist) chemically react with the dissociated O_2. (b) Matrix 105 O2 plasma asher system used in this project.

3.3.1 Oxygen plasma asher

The O_2 plasma asher is used for the purpose of removing the stubborn photoresist from the sample surface. When the photoresist served as a softmask during the plasma etch process, it is etched simultaneously and is burned by the plasma bombardment, resulting in altered chemical properties of the photoresist. This hardens the photoresist making it diffcult to be removed by standard solvent cleaning processes. The O_2 plasma asher system generates a mixture of O_2 and N_2 plasma in a reaction chamber (Fig. 3.17(a)) and the mixture flows across the sample surface. Dissociated O_2 then chemically reacts with the photoresist residuals and burns them off the sample. The Matrix 105 O2 asher used in this project is shown in Fig. 3.17(b)

3.3.2 Thermal annealing

The thermal annealing process is one of widely used processes in semiconductor fabrication. Thermal annealing has several purposes such as doping activation [125], defect recovery [126] and contact formation [127]. The schematic diagram of the processing chamber is demonstrated in Fig. 3.18(a) and the Jipelec JetFirst RTA system used in this project to achieve thermal annealing process is shown in Fig. 3.18(b). The heat source inside the chamber is a tungsten halogen lamp, which provides infrared (IR) radiation to generate heat at the sample chuck. The

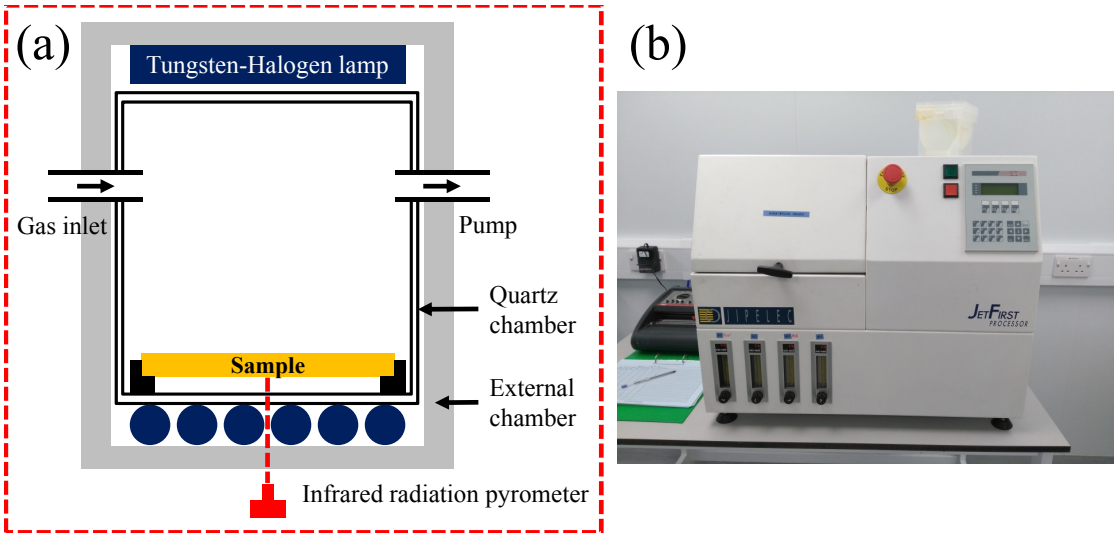

FIGURE 3.18: (a) Schematic diagram of processing chamber. The sample is heated up by a tungsten halogen lamp overhead while a infrared radiation pyrometer is used to monitor the sample temperature. (b) Jipelec JetFirst RTA system used in this project.

vertical-arrayed lamp units are located under the sample chuck to provide uniform heating. In order to monitor the wafer temperature, an IR pyrometer is set to monitor the sample. The steady peak temperature of the RTA used in this project is 1000 °C while the maximum peak temperature is 1300 °C. Different gases such as nitrogen (N_2), O_2, air and argon (Ar) can be introduced into the chamber via gas inlet so that the sample can be annealed in different gaseous environment. In this project, the annealing temperature for the Pd-based metal contacts to the p-type GaN is about 300 °C.

3.4 Summary

In this chapter, semiconductor fabrication techniques have been introduced. The initial materials used in this project are firstly described in section 3.1. Details of fabrication techniques including deposition, pattern definition and pattern transfer are given in the following sections (from section 3.2 to section 3.4). The devices demonstrated in this thesis are produced by using above techniques. In the next chapter, the designs and fabrication steps of devices will be introduced.

Chapter 4

High-density penetrating microelectrode array for electrophysiology

In previous chapters, devices to investigate information flows in neural circuits have been reviewed (chapter 2) and typical semiconductor fabrication techniques used to produce those devices have been introduced (chapter 3). Here, the fabrication process and the performance characterization are detailed. The design of penetrating microelectrode array is firstly introduced in section 4.1. Then the fabrication process and the performance characterization are demonstrated in section 4.2 and 4.3 respectively.

4.1 Design of high-density penetrating microelectrode array

In order to achieve neural recordings with high signal-to-noise ratio (SNR), recording sites should be positioned close to the neurons (< 100 μm) [128]. Moreover, a dense array enables neural recordings with high spatial resolution. Therefore, a novel high-density penetrating microelectrode array is designed and fabricated in this project to record neural signals *in vivo* or *in vitro*. The novelty of the device lies in the fact that the electrodes are at the tips of needle-like structure (> 100 μm tall) that are closely spaced to allow spike sorting (60-μm pitch).

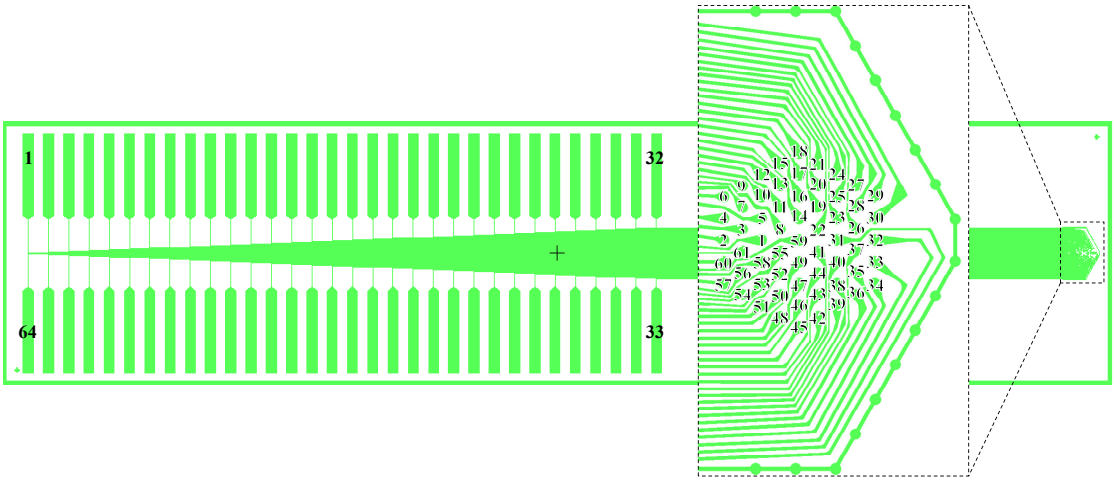

FIGURE 4.1: Design of high-density penetrating microelectrode array. Channel 5 is unused and channel 32 and 33 are connected to the grounding electrodes. The close-up image shows the microelectrode array.

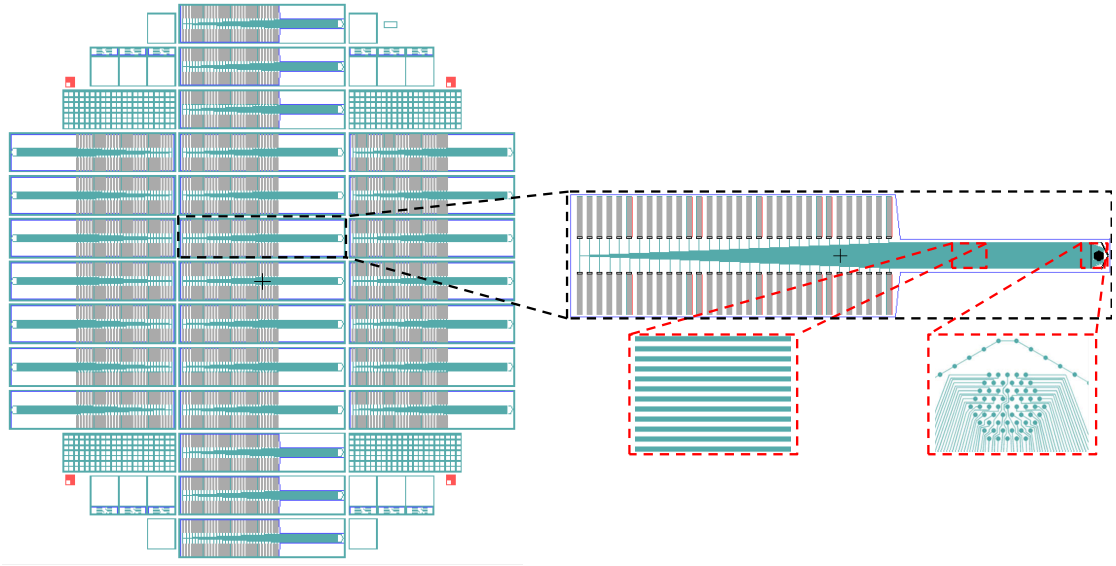

FIGURE 4.2: Photomask design of microelectrode array. The mask is designed for 4-inch wafer fabrication and each wafer contains 27 devices. The array region and tracks are highlighted by red dash boxes.

In this project, a novel high-density microelectrode array has been developed which enables high resolution electrophysiological recordings. As shown in Fig. 4.1, the design has 61 hexagonally close-packed recording needles and 18 ground needles placed around the array. In the design, channel 32 and 33 are connected to the grounding needles to achieve a local ground that will improve the background noise while recording signals from neurons. Since the total number of recording needles is 61, channel 5 will be left unused. The pitch of the recording array is 60 μm, which enables high resolution recordings. Each needle is 250-μm long and has a

tapered profile (20-μm diameter at the base and 10 μm at the tip) which minimizes the invasive damage to the neural tissues. Bonding pads and the recording array are separated, resulting in better implantation into the tissue without restriction of external electronic circuits.

The microelectrode array is fabricated on a silicon substrate, with tungsten-based interconnection wires and recording sites. In order to further improve the electrical properties of the electrodes, platinum black is coated on the tip of each needle. A gold layer is deposited on the bonding pad area to allow for reliable connections to the external electronic system. As a result, photomasks are required to accomplish pattern processing in different layers. The photomask is designed using the software package *L-edit*. As shown in Fig. 4.2, a 4-inch photomask includes 27 devices (left) and one die is highlighted by the black dash box. The array region and the tracks are detailed in red dash boxes. Two pairs of alignment marks (in red) are set on the four corners to achieve precise alignment between patterns on the photomask and the sample.

4.2 Fabrication process of high-density penetrating microelectrode array

A schematic of the fabrication process is shown in Fig. 4.3. The fabrication starts with 4-inch Si wafer, which is about 380-μm thick. Deep holes with tapered profiles are formed on the Si substrate by a deep RIE process. Thermal oxidation follows to create a dense layer of SiO_2 on the surface of the substrate and down the tapered holes. A bilayer of Ti/W is conformally deposited using a CVD process to form recording sites, interconnection wires and bonding pads. The pads are created with a Ti/Au layer to facilitate wire bonding. After that, the whole sample is coated with a parylene-C film. Since parylene-C is a biocompatible and insulating material, it acts a good protecting layer when the needle array is implanted into the animal brain *in vivo* or used with cultured tissues *in vitro*.

All needles are revealed from the backside of sample by wet etch. Typically, potassium hydroxide (KOH) solution is used to etch the bulk silicon substrate to expose the needle array. The revealing process is separated into three steps: firstly, the bulk silicon is etched by KOH wet etch to expose needle tips; secondly, a buffered oxide etch (BOE) solution is used to thin down the thickness of SiO_2 layer

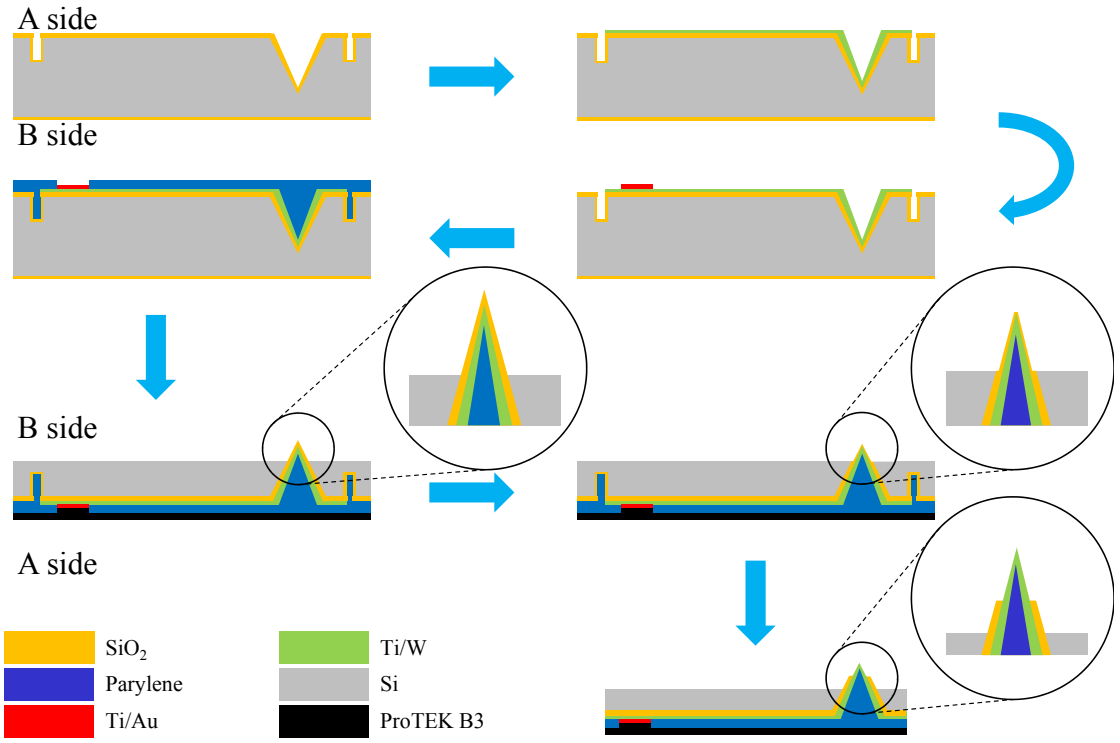

FIGURE 4.3: Fabrication process flow of high-density penetrating microelectrode array. The fabrication started with a 4-inch silicon wafer (shown in grey). The wafer was firstly deep etched to form needle profiles (250-μm deep) and then a thermal oxidation layer (2 μm, shown in yellow) was grown on both sides of wafer. The metal tracks and electrodes (50 nm/400 nm titanium/tungsten bilayer, shown in green) was formed and titanium/gold bilayer (50 nm/300 nm, shown in red) was then deposited to form wire bonding pads. All the tracks and electrodes were insulated by parylene-C film (5 μm, shown in blue). The front-side fabrication was end with coating alkaline resistance film (ProTEK B3, shown in black). The needle tips were firstly revealed by potassium hydroxide aqueous solution and then the oxide layer on the tip were initially thinned by buffered oxide etching solution. Finally, the whole needles were exposed by potassium hydroxide aqueous solution and then the remaining oxide on the tips were finally removed by buffered oxide etching solution to reveal the metal contacts.

on the tips; thirdly, the silicon substrate is further etched by KOH wet etching to reveal the whole needles. In order to protect samples during the KOH etch step, a thin layer called ProTEK B3 is used as a protection layer. The ProTEK B3 is supplied by Brewer Science, Inc and is an organic material with high resistance to alkaline solution. The fabrication ends with SiO_2 etching, achieved by BOE solution, to expose the conductive recording sites on the needle tips.

The fabrication process is detailed step by step in the following paragraphs. The entire process is challenging since both the front side and the back side of sample

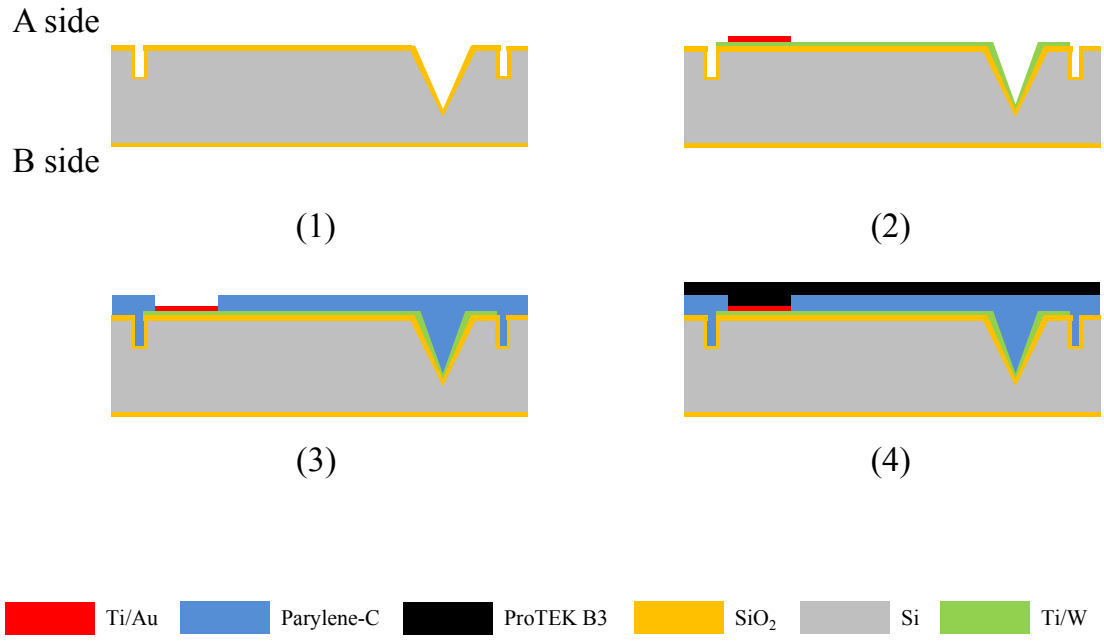

FIGURE 4.4: Front-side fabrication steps of the microelectrode array. The needle structures are formed on the substrate and a SiO_2 layer is grown on the surface of sample (**step #1**). Recording sites, tracks and bonding pads are made of Ti/W bilayer and wire-bonding areas are made of Ti/Au (**step #2**). Insulation layer (parylene-C film) is coated to the sample (**step #3**) and KOH protection layer (ProTEK B3) is spin coated to the sample afterwards (**step #4**).

are required to be processed. Therefore, some steps have been optimized and several extra steps have been added to ensure successful device fabrication.The entire fabrication process of microelectrode array is divided into two parts: fabrication on the front side and fabrication on the back side.

4.2.1 Front-side fabrication (Fig. 4.4)

Step #1 The sample is solvent cleaned with acetone, methanol and isopropyl alcohol (IPA). In order to achieve deep silicon etch in ICP system, a 580-nm thick aluminium (Al) layer is firstly sputter deposited onto the sample as a hard-mask. To pattern the Al layer, Shipley S1805 positive photoresist is used in a photolithography step and acted as a softmask in Al etch. In this project, the Al layer is etched in ICP system by using boron chloride gas (BCl_3) and chlorine gas (Cl_2). The Al etching recipe is shown in Table A.1. Before Si deep etching, the sample is solvent cleaned to remove the remaining photoresist during the Al etch.

The Si deep etch is achieved using the Bosch process in an ICP system. This process gives an aspect ratio of needle height : base diameter > 12 : 1. Furthermore, this process gives a tapered needle profile which will minimise the insertion damage caused by the device.Typically, the Bosch process is designed to obtain high aspect ratio structures with parallel sidewalls. Therefore, the parameters of Bosch process should be optimized to achieve the tapered etch profile.

The Bosch process is named after the Germany company Robert Bosch GmbH which patented the process. It is a cyclic process which consists of alternating etching and deposition steps [129]. As shown in Fig. 4.5, the process starts with an etching step. Sulfur hexafluoride (SF_6) is used to etch silicon. Then it is followed by the deposition step, which uses octafluorocyclobutane (C_4F_8) to form a Teflon-like polymer on the Si surface. The polymer does not react with SF_6 so it can protect the sidewalls during the etching step. When the next etching step begins, the polymer on the bottom of structure will be removed by physical bombardment etching. The ions are accelerated by the electrical field so that they are able to directionally strike the surface with near normal incidence. As a result, the polymer on the sidewalls will not be removed and the one on the bottom will be removed. By switching back and forth between the etching step and the deposition step, the Si can be etched hundreds of micrometres at high aspect ratio.

After the Bosch process, a test sample was cleaved across the hole to check the cross-section under the scanning electron microscope (SEM). When the duration of an etching step equals the duration of a depositing step, parallel sidewalls are created (Fig. 4.6(a) & (b)). The etch recipe is shown in Table A.2. Since the etch rate of the Si, using this recipe, is about 27 μm/hour, a 250-μm deep structure requires approximately a 10-hour etch, which is a long etch step. Therefore, to increase the etch rate, Ar gas is added to increase the portion of physical etch, resulting in improving etch rate. Moreover, the etching profile is expected to be tapered at the bottom. So the time ratio between the etch step and the deposit step is further optimized. As shown in Fig. 4.7, the tapered profile is achieved by setting a 1:2 time ratio between etching and deposition. Furthermore, in order to improve the sidewall roughness we adapted a standard etch recipe (shown in Table A.3) that alters the SF_6 flow rate from 150 sccm (1.5 seconds) to 300 sccm (3.5 seconds).

After the Si deep etch, the remaining Al layer is removed by hydrochloride acid (HCl). Once the sample is solvent cleaned, a dense SiO_2 layer (2-μm thickness) is

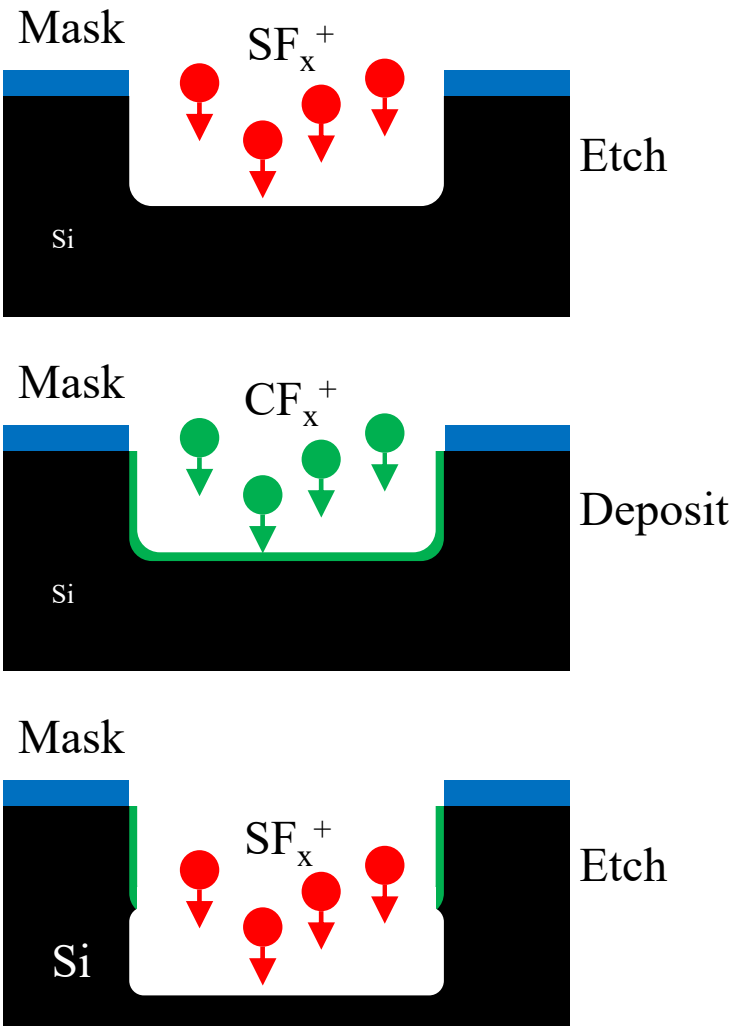

FIGURE 4.5: Schematic of Bosch process for Si etching. The process cycles between etching step (SF_6) and deposition step (C_4F_8). The polymer produced in deposition step can protect the sidewalls so in the etching step, the etch direction will be more vertical. Therefore, high aspect ratio profile can be achieved by Bosch process.

grown on the surface of sample by a wet thermal oxidation process (Fig. 4.8).

Step #2 A Ti/W bilayer (50 nm/450 nm) is deposited using a CVD process. In particular, the chemical reaction of W deposition can be summarized below:

$$2WF_6 + 3SiH_4 \rightarrow 2W + 3SiF_4 + 6H_2 \tag{4.1}$$

$$WF_6 + 3H_2 \rightarrow W + 6HF \tag{4.2}$$

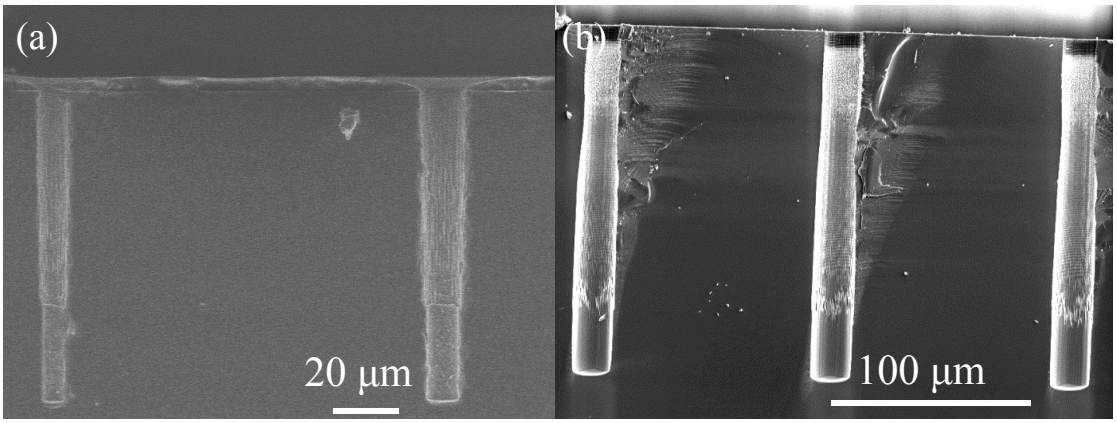

FIGURE 4.6: SEM images of etching profile achieved by initial Bosch process. (a) Bosch process applied on 10-μm hole (left) and 15-μm hole (right). Scale bar: 20 μm; (b) Bosch process applied on 20-μm holes. Scale bar: 100 μm.

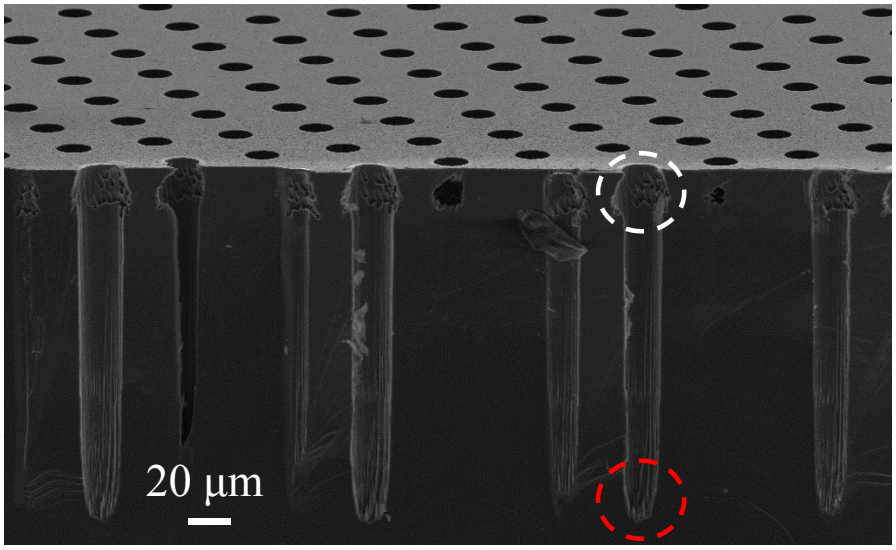

FIGURE 4.7: SEM images of etching profile achieved by optimized Bosch process. Base diameter is 20 μm (highlighted by the white dash circle) and tip diameter is 10 μm (highlighted by the red dash circle). Scale bar: 20 μm.

After deposition, a SiO_2 layer (100 nm) is deposited by PECVD process and acts as a hardmask in the Ti/W etching. The chemical reaction of SiO_2 deposition is given below:

$$SiH_4 + O_2 \rightarrow SiO_2 + 2H_2 \tag{4.3}$$

To pattern the SiO_2 layer, Shipley S1805 positive photoresist is used to transfer the features from the photomask to the sample by photolithography. However, the spinning uniformity of photoresist is significantly affected by the high aspect ratio features on the sample. Without deep holes, spin coating of S1805 photoresist

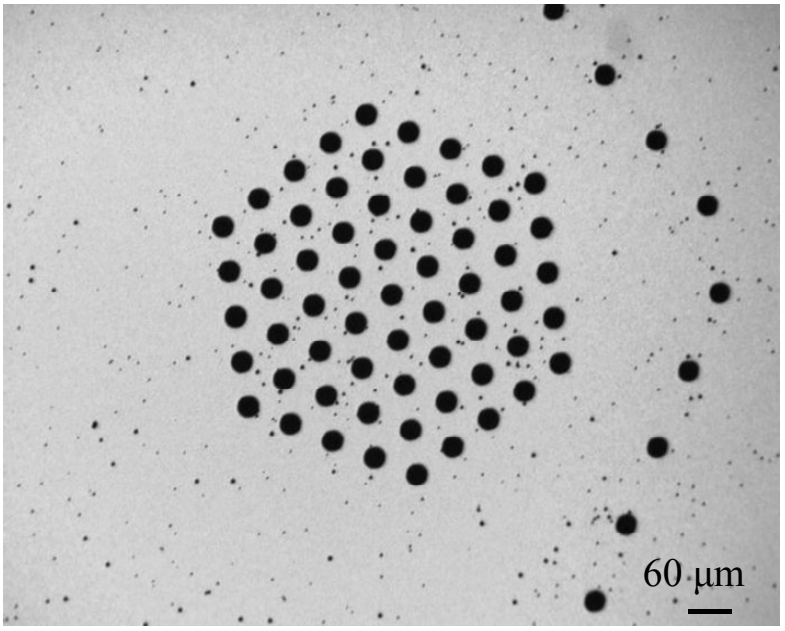

FIGURE 4.8: Optical microscope images of the sample after the wet thermal oxidation process. Scale bar: 60 μm.

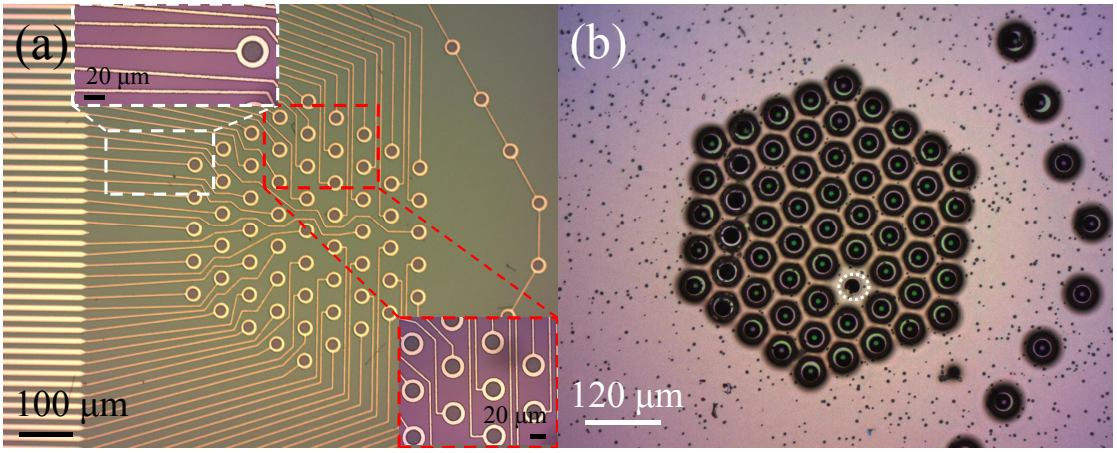

FIGURE 4.9: Comparison of photoresist coating on the sample without and within the high aspect ratio needle structure. (a) Uniform photoresist coating on the flat sample and good definition of metal electrode and inter-connection wires. Scale bar: 100 μm. (Inset) top and bottom are the close-up images of the array area. Scale bar: 20 μm; (b) Nonuniform photoresist coating over the needle structures. Photoresist around the needle is thicker than in the rest of the device. The white dash circle indicates an unetched electrode. Scale bar: 120 μm.

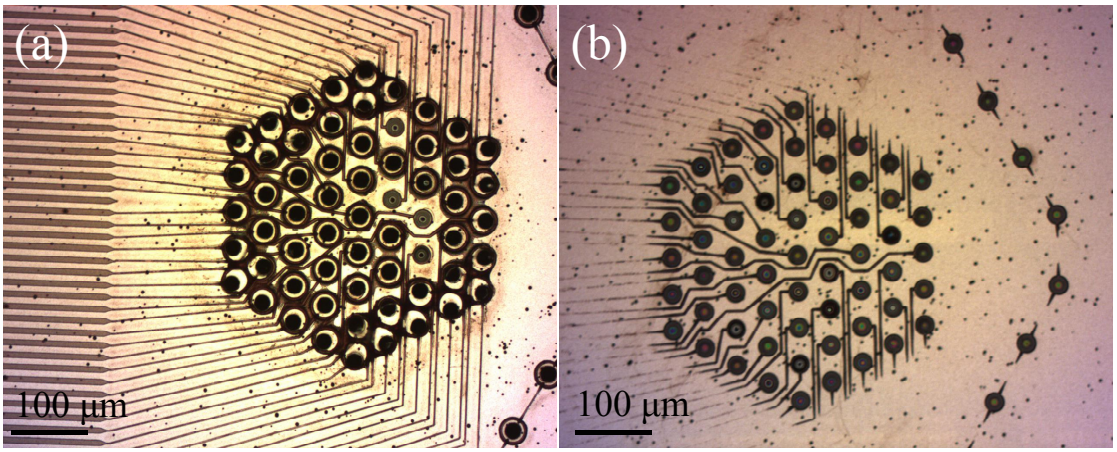

FIGURE 4.10: Optical microscope images of photolithography process applied to the nonuniform photoresist-coated samples. (a) Inter-connection wires are exposed and developed completely while the metal electrodes are not fully revealed due to the nonuniformity of the photoresist around the holes. Scale bar: 100 μm; (b) Metal electrodes are successfully exposed and developed but the inter-connection wires are sacrificed due to over-developing. Scale bar: 100 μm.

could be uniform so that the microelectrode array and tracks could be defined clearly (Fig. 4.9(a)). On the contrary, poor uniformity of photoresist coating occurs when spin coating photoresist onto the sample with the deep hole features. Non-uniform coating of photoresist is showed in Fig. 4.9(b). The array has been deep etched by our optimized Bosch process except for one site labelled by the white dash circle. When spin coating the photoresist onto the sample, the photoresist accumulates at the edge of hole and partially covers the hole due to the spin dynamics, gravity and the surface tension of photoresist. However, no photoresist accumulates at the unetched site which represents a flat surface at that region. Therefore, photoresist around the holes is thicker than in other region of the sample surface (black rings around the holes in Fig. 4.9(b)). As a result of the thicker photoresist, the photolithography steps become significantly more challenging. If the photoresist is processed using our standard processes, the area around the deep holes will not be exposed or developed properly (Fig. 4.10(a)). However, if we modify the standard process to account for the thicker resist we will overdevelop regions away from deep holes and loose the contrast of our structures (Fig. 4.10(b)).

In order to avoid nonuniform spin coating, here a multi-exposure strategy is developed in this project to overcome this challenge. Since the photoresist around the holes is thicker than the one in other parts of the sample, longer exposure times are required to completely expose the thicker part of photoresist. Moreover,

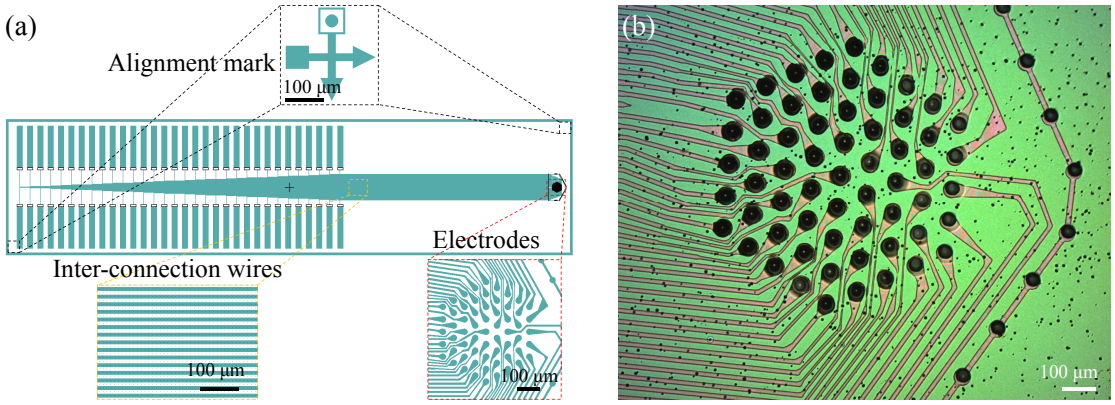

FIGURE 4.11: (a) Photomask for multi-exposure step. Scale bar: 100 μm; (b) Optical microscope image of photolithography after multi-exposure step. Scale bar: 100 μm.

during the longer-time exposure, thinner tracks around the electrode area are over exposed and will disappear in the developing step. Therefore, a new photomask with wider tracks was designed for this multi-exposure step (Fig. 4.11(a)) and a better photolithography result is shown in Fig. 4.11(b).

The SiO_2 layer is then etched by Ar and CHF_3 in an RIE tool, while photoresist serves as a softmask. The etching recipes are shown in Table A.4 and A.5. After etching, the sample is solvent cleaned to remove the photoresist. Then the Ti/W bilayer is etched in a RIE tool by SF_6. The etching recipe is shown in Table A.6. The remaining SiO_2 is removed by BOE solution (as shown in Fig. 4.12(a) and (b)). The BOE solution used in this project is a mixture solution which normally includes a 7:1 volume ratio of 40% NH_4F in water to 49% HF in water. As a consequence, the etch rate of SiO_2 in BOE solution is about 100 nm/min. The chemical reaction is expressed below:

$$SiO_2 + 6HF \rightarrow H_2SiF_6 + 2H_2O \tag{4.4}$$

In order to achieve a good quality of wire bonding, a Ti/Au (50 nm/300 nm) bilayer is required on the top of the bonding pads. In order to avoid plasma damage on the Ti/W layer, a lift-off process is used to define features on the Ti/Au layer. Firstly, patterns are transfered from the photomask by using MEGAPOSIT SPR220-4.5 photoresist. Then the Ti/Au bilayer is sputter deposited onto the sample. Finally, the sample is soaked in the Microposit^{TM} remover 1165 which is heated up to 80 °C in the water bath to dissolve the remaining photoresist. As a result, the metal layer deposited on the top of the photoresist is 'lift' off from the sample surface,

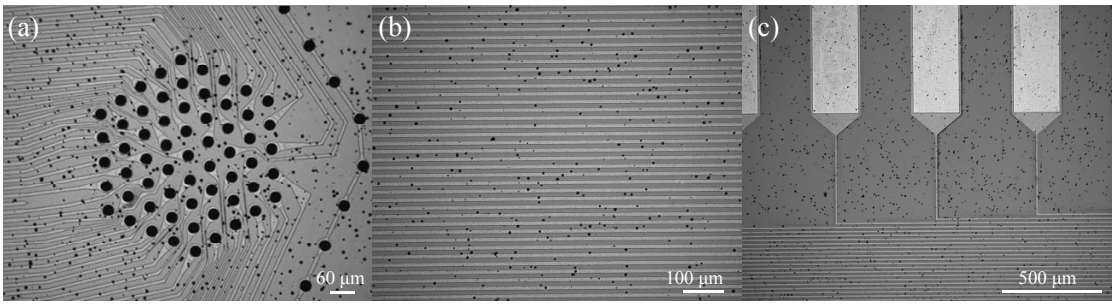

FIGURE 4.12: Optical microscope images of the sample after metalization. (a) Recording sites formed by Ti/W bilayer. Scale bar: 60 μm. (b) Interconnection tracks. Scale bar: 100 μm. (c) Bonding pads for connecting external electronic system. Scale bar: 500 μm.

whereas the one without photoresist underneath is left on the sample surface. The optical microscope images of metal bonding pads are shown in Fig. 4.12(c).

Step #3 A thick parylene-C film (5 μm) is coated to the sample to insulate the neighbouring interconnection wires. In this project, the parylene-C film is deposited using a dedicated parylene coater. To pattern the parylene-C film, a MEGAPOSIT SPR220-7.0 photoresist is used due to the low selectivity between parylene-C and photoresist under O_2 plasma etching (about 1:1). The parylene-C film is etched in RIE tool by O_2 and the etching recipe is shown in Table A.7.

Step #4 In order to protect the features on the front side of the sample during the KOH etch, a ProTEK B3 film is spin coated onto the sample as a protection layer.

4.2.2 Back-side fabrication (Fig. 4.13)

Step #5 30 wt% KOH solution is used to etch bulk Si so that the needle tips could be exposed. The temperature of solution is kept at 80 °C to achieve the etch rate of approximately 2 μm/min. The chemical reaction between KOH and Si is shown below:

$$Si + 2OH^- + 2H_2O \rightarrow SiO_2(OH)_2^{2-} + 2H_2 \tag{4.5}$$

However, the edge interface of ProTEK B3 and the sample is etched by KOH solution even though ProTEK B3 fully covers the sample surface. As a result, the ProTEK B3 film starts to peel off from the sample surface and features underneath

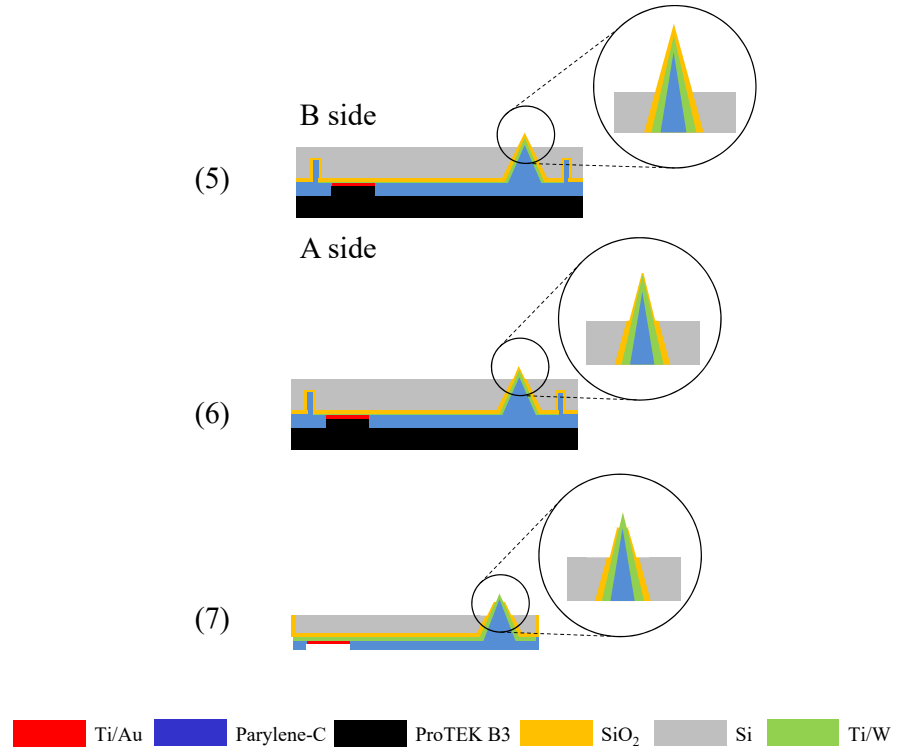

FIGURE 4.13: Back side fabrication steps of the microelectrode array. The needle tips are firstly revealed (**step #5**). Entire needles are then revealed (**step #6**). The last step (**step #7**).

are damaged by KOH solution (Fig. 4.14(a)). After several tests, it was found that features could be protected in a 70-minute etching step (Fig. 4.14(b)). The uniformity of ProTEK B3 film becomes poorer after 70 minutes. Therefore, the KOH etch was separated into several 70-minute etch steps. After each step, the ProTEK B3 film is fully removed from the sample and a fresh one is spin coated. Furthermore, an etching setup is designed to provide a simple control on the KOH etch (Fig. 4.15). The sample is fixed onto a platform which could freely move in vertical direction. Therefore, the KOH solution only etches the Si at the array region. The needle tips are exposed as shown in Fig. 4.16.

Step #6 After this partial KOH etching, where the needle tips are revealed to a depth of about 20 μm, the oxide that coats the tip of the needles is thinned down to 1μm by BOE solution (shown in Fig. 4.17). Again, only the array region is immersed into the BOE solution.

Step #7 120-min KOH etch is performed to further etch down the Si substrate so that the array could be revealed to the designed height. After solvent clean, the sample is immersed into the BOE solution to remove the remaining SiO_2 layer on the tips of needles. The needles are shown in Fig. 4.18.

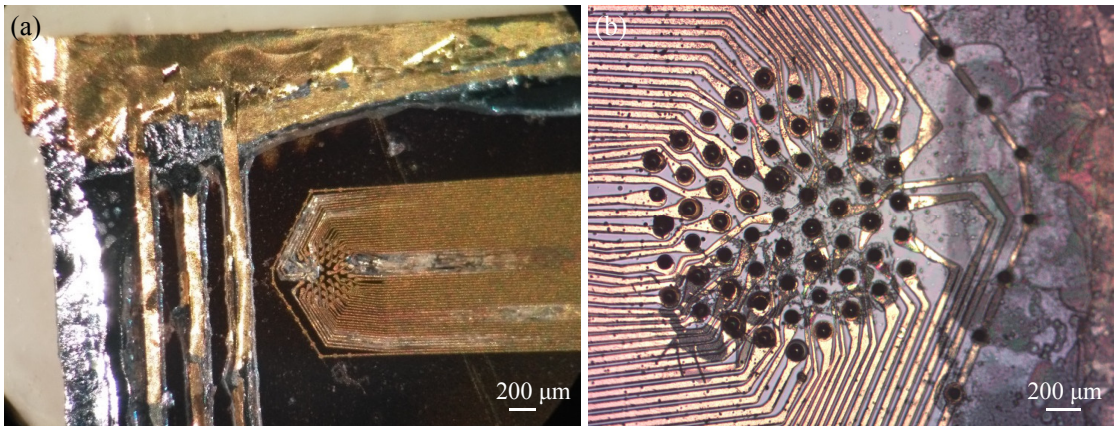

FIGURE 4.14: Post-etch images of front side surface. (a) Test sample after a long KOH etch. The ProTEK B3 film starts to peel off from the edge of sample and metal electrodes and tracks are partially etched away by KOH solution. Scale bar: 200 μm; (b) Metal electrodes and tracks are well-protected after 70-minute etch. Scale bar: 200 μm.

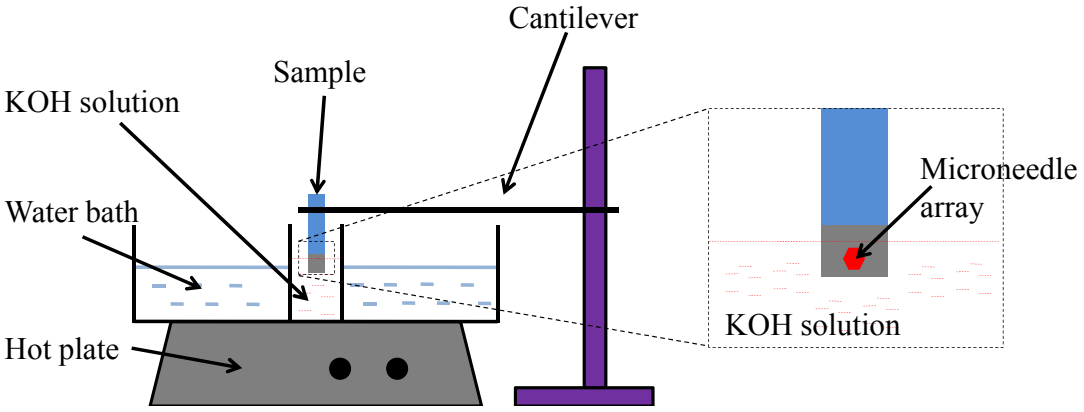

FIGURE 4.15: Schematic diagram of Si wet etching setup. Only the array region is dipped into the KOH solution.

4.3 Characterization of high-density penetrating microelectrode array

In the previous subsections, the fabrication steps for a penetrating microelectrode array were outlined. In this subsection, the performance of penetrating microelectrode array is characterized. The microelectrode array includes 61 recording elements and 18 grounding elements. All the recording channels are electrically isolated and the inter-channel capacitance were measured to be at the picofarad-level to avoid electric cross-talk. Furthermore, recording sites with low electrical impedance are achieved to record extracellular signals (typically between 50 μV and 500 μV) [130, 131].

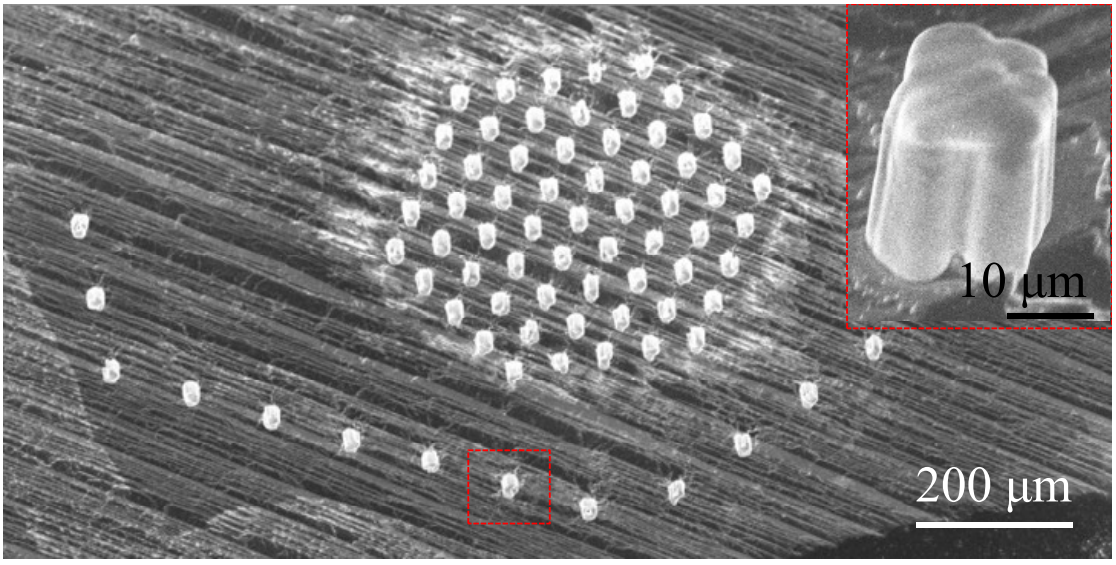

FIGURE 4.16: SEM image of the needle tips. Scale bar: 200 μm. (Inset) close-up image of a single needle tip. Scale bar: 10 μm.

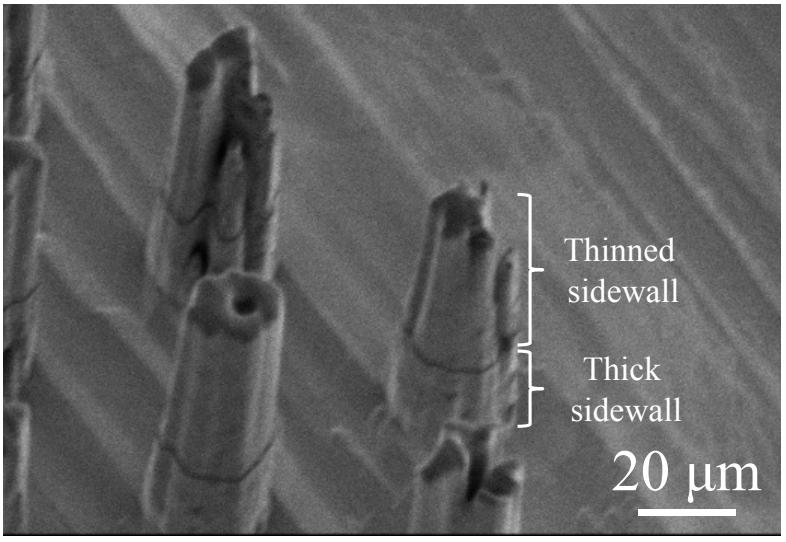

FIGURE 4.17: SEM image of the microneedles with thinned sidewalls. Scale bar: 20 μm.

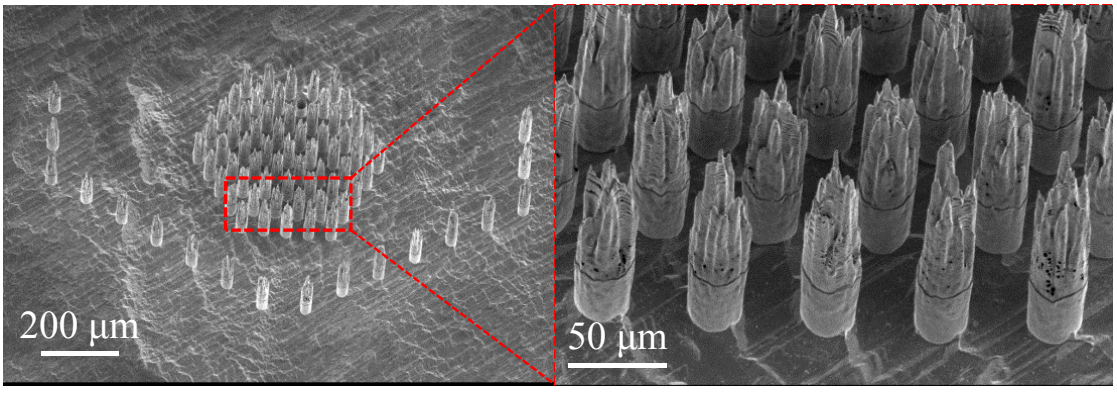

FIGURE 4.18: SEM image of the penetrating microelectrode array. Scale bar: 200 μm. The needles are highlighted in the red dash box. Scale bar: 50 μm.

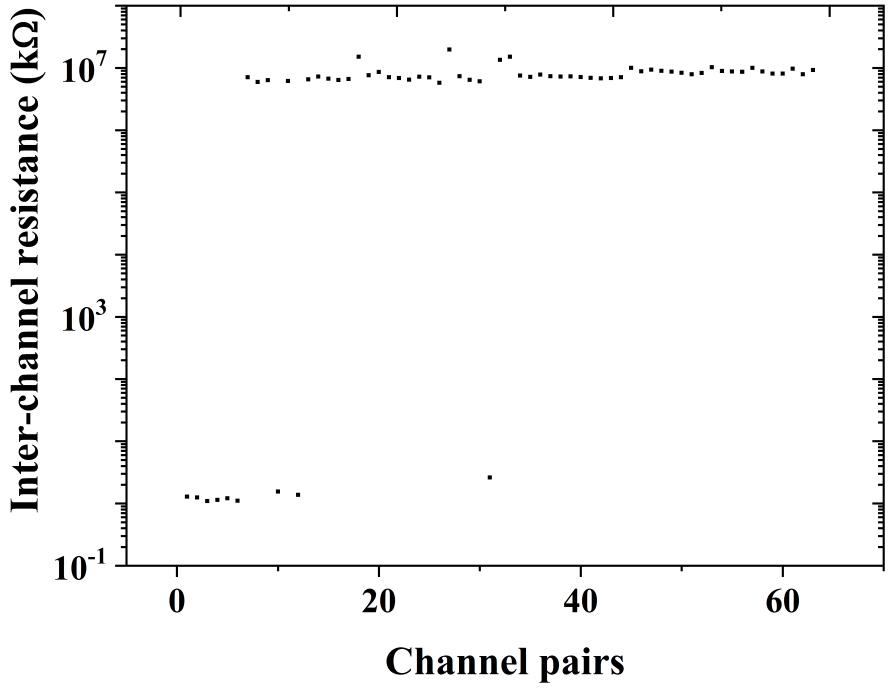

FIGURE 4.19: Resistance between adjacent channels. 9 pairs of channels are electrical shorted (inter channel resistances are about 1 kΩ).

4.3.1 Measurement of inter-channel resistance and capacitance

According to the design of penetrating microelectrode array, the interconnecting tracks are made of titanium and tungsten and are isolated by silicon dioxide. As shown in Fig. 4.1, the long parallel metal tracks connect to the electrodes and bonding pads. To evaluate the fabrication yield of microelectrode array, the inter-channel resistance and capacitance are measured respectively. The check is processed between adjacent channels: channel #1 and #2, channel #2 and #3, etc. As shown in Fig. 4.19, inter-channel resistances in 9 pairs of channels are about 1 kΩ and rest of them are about 10^7 kΩ, which is not the real resistance but the limitation of the instrument. Therefore, 9 pairs of channels are electrically shorted and the short circuits are caused by the etch defects introduced in deep reactive ion etch. In other word, over 80 % fabrication yield is achieved, i.e. 48 working electrodes from 61.

On the other hand, the recording channels are made of Ti/W bilayer. Therefore, long, parallel adjacent recording channels could form a parallel plate capacitor.

As a result, any alternating current (AC) signals in one channel could induce a voltage in the neighbouring channel, known as capacitive cross-talk. Since this cross-talk between channels occurs before the pre-amplification stage, even small voltages may induce noticeable signals in adjacent channels. In order to prevent this, the inter-channel capacitance should be at a low level. Since the impedance (Z) of a capacitor is relevant to its capacitance (C) and the signal frequency (f) (shown in formula 4.6),

$$\begin{aligned} Z &= \frac{1}{j\omega C} \\ &= \frac{1}{j2\pi fC} \end{aligned} \tag{4.6}$$

the impedance increases when the capacitance decreases. At a given frequency of 1 kHz, if the capacitance C is 1 μF, the impedance Z will be about 200 Ω. If the capacitance is 1 pF, the impedance will be about 200 MΩ. Since the impedance of electrode is designed to be at kiloohm-level, the capacitance therefore should be at picofarad-level to ensure a capacitor with greater impedance so that the capacitive cross-talk could be prevented. In this project, the inter-channel resistance and the inter-channel capacitance are measured with an LCR meter (LCR-821, ISO-TECH). As shown in Fig. 4.20, the averaged inter-channel capacitance among all the working electrodes is about 3.11 pF.

4.3.2 Measurement of microelectrode impedance

The electrode-electrolyte impedance is another important factor of microelectrode array performance in electrophysiological recordings. Typically, the amplitude of extracellular neural signals about hundreds of microvolts. Since action potentials have a duration of about 1 ms, an electrode should have a low impedance interface at 1 kHz frequency [1, 51].

The main charge transfer mechanism between the neurons and the electrode is through capacitive mechanism. Therefore the surface area of the electrode plays a significant role. The larger area the electrode is, the lower the impedance [132–134]. Due to the small dimensions of the electrodes, the impedance is typically expected to be megaohms or less at 1 kHz [135–137]. In this project, the recording

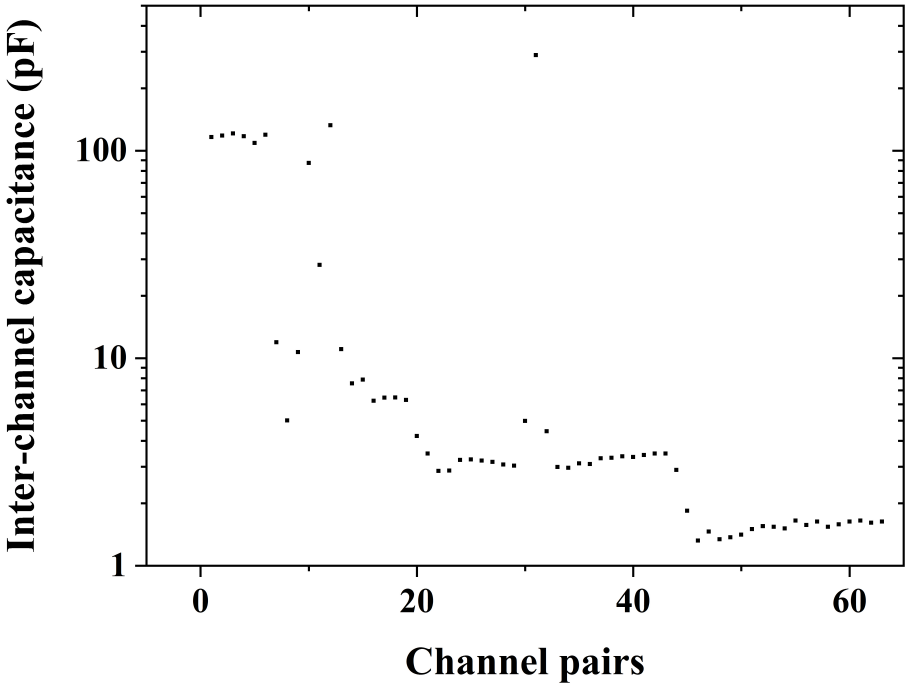

FIGURE 4.20: Capacitance between adjacent channels. 9 pairs of shorted channels have high inter-channel capacitance (more than 100 pF). The inter-channel capacitance between working channels are about 3 pF.

sites are needle shaped, which can be simplified as circular truncated cones (*ctc*) (shown in Fig. 4.21). According to the design and the fabrication, the diameter of the needle tip is about 15 μm and the height of the exposed tip is about 70 μm. Based on the geometry, the lateral surface area of a cone $A_{cone-lateral}$ can be written as:

$$A_{cone-lateral} = \pi \cdot R \cdot \sqrt{H^2 + R^2} \tag{4.7}$$

where R is the radius of base and H is the height of the cone. The lateral area of the circular truncated cone could be expressed as:

$$\begin{aligned} A_{ctc-lateral} &= A_{cone1-lateral} - A_{cone2-lateral} \\ &= \pi \cdot R_1 \cdot \sqrt{H^2 + {R_1}^2} - \pi \cdot R_2 \cdot \sqrt{(H-h)^2 + {R_2}^2} \end{aligned} \tag{4.8}$$

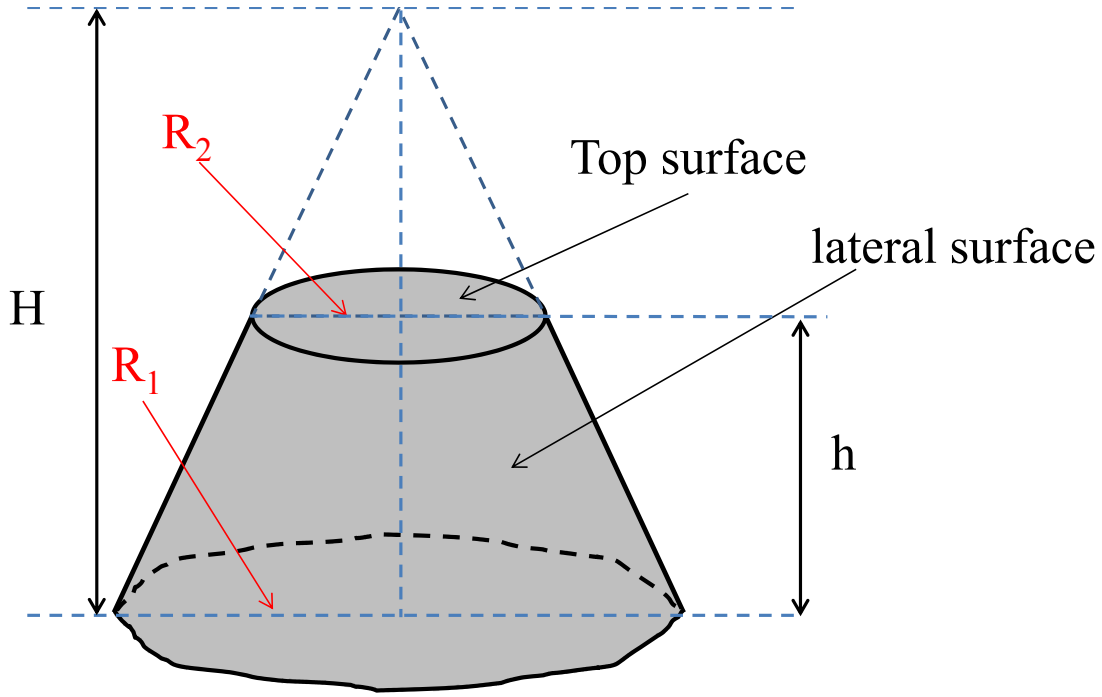

FIGURE 4.21: Simplification of single needle tip.

where H is the height of the cone, h represents the height of the circular truncated cone, R_1 and R_2 are the radii of base and top surface respectively. Therefore, the total surface area of the exposed needle tip in this project includes the lateral area and the top surface area, which is about 5,600 μm^2 in total. This is much larger than one of the more standard planar microelectrode arrays. Therefore, the impedance of the penetrating microelectrodes is expected to be lower than that of the planar microelectrodes [138]. Typically, a 5-μm diameter electrode has an impedance of about 6 MΩ at 1 kHz without coating any materials. After electroplating optimised materials, the impedance at 1 kHz can be reduced to about 300 kΩ [59, 139].

To measure the impedance of the penetrating microelectrodes, the needles were dipped into the electrolyte and a simplified equivalent circuit of the electrode-electrolyte interface is shown in Fig. 4.22, which comprises the interfacial capacitance (C_i), the charge transfer resistance (R_t) and the solution resistance (R_s) [140].

Interfacial capacitance C_i

When an electrode is immersed in an electrolyte, charge transfer immediately occurs at the interface between the metal and the electrolyte. According to the model of Gouy-Chapman-Stern [141], the interfacial capacitance (C_i) is a series

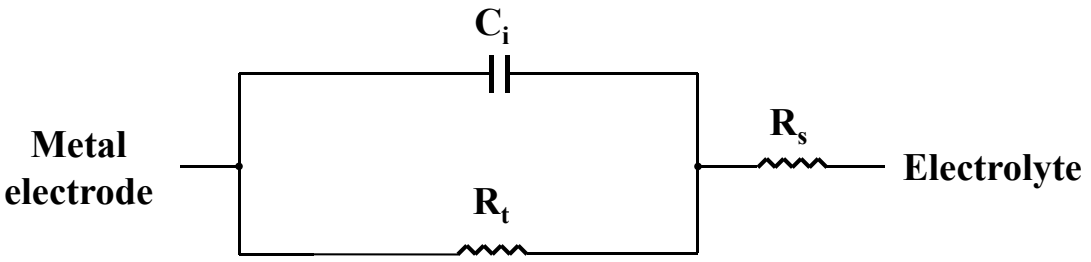

FIGURE 4.22: Simplified circuit model for the needle-electrolyte interface including the interfacial capacitance (C_i), the charge transfer resistance (R_t) and the solution resistance (R_s).

combination of the double-layer capacitance C_H and the diffuse layer capacitance C_G. This capacitance can be expressed as the following formula:

$$\frac{1}{C_i} = \frac{1}{C_H} + \frac{1}{C_G} = \frac{d_{OHP}}{\epsilon_0 \epsilon_r} + \frac{L_D}{\epsilon_0 \epsilon_r \cosh(\frac{z\phi_0}{2U_t})} \tag{4.9}$$

where d_{OHP} is the thickness of the double layer. ϵ_0 is the permittivity of free space and ϵ_r is the permittivity of the double layer. The double layer exists at the interface of electrolyte and electrode, which formed by two opposite ions. z is the charge on the ion in the electrolyte, $\phi_0$is the potential at the electrode and U_t is the thermal voltage. L_D is called Debye length, which characterizes the potential decay in distance. The Debye length can be written as a function of potential to the thickness of diffuse layer:

$$L_D = \sqrt{\frac{\epsilon_0 \epsilon_r U_t}{2n^0 z^2 q}} \tag{4.10}$$

where n^0 is the bulk number concentration of ions in the electrolyte and q is the charge on an electron.

Charge transfer resistance R_t

The charge transfer resistance (R_t) is formed at the interface of the electrode and the electrolyte due to the oxidation and reduction reactions. The resistance is determined by the exchange current density (J_0) which is generated by the charge

transfer during the oxidation and reduction reactions. The exchange current density is relevant to the material properties of the electrode and the compositions in the electrolyte. According to previous studies, the values of the exchange current density of different materials are shown in the Table 4.1 [3]. Even though the values of exchange current densities here are given in the sulfuric acid, they provide good references to start for investigating the values in physiological solutions.

TABLE 4.1: The exchange current densities (J_0) for different materials in 1 mol/kg H_2SO_4 after [3].

Material	**Exchange current density -log$_{10}$ (A/cm^2)**
Pd	3.0
Pt	3.1
Rh	3.6
Ir	3.7
Ni	5.2
Au	5.4
W	5.9
Nb	6.8
Ti	8.2
Cd	10.8
Mn	10.9
Pb	12.0
Hg	12.3

Solution resistance R_s

The solution resistance (R_s) is the resistance of the electrolyte between the recording electrode and the grounding electrode. It can be calculated from:

$$R_s = \rho \frac{L}{A} \tag{4.11}$$

where ρ is the resistivity of the electrolyte, L is the distance between the working electrode and the grounding electrode and A is the cross-sectional area of the electrolyte.

Therefore, the impedance of each component can contribute to the total impedance during the impedance measurement. The impedance of interfacial capacitance can be written as:

$$\begin{aligned} Z_{C_i} &= \frac{1}{j\omega C_i} \\ &= \frac{1}{j2\pi f C_i} \end{aligned} \tag{4.12}$$

and f is the ordinary frequency (Hz). According to the circuit model, the interfacial capacitance and the charge transfer resistance are in parallel. Therefore, the total impedance of the simplified circuit Z_{total} could be calculated as:

$$\begin{aligned} Z_{total} &= Z_s + \frac{1}{\frac{1}{Z_t} + \frac{1}{Z_{C_i}}} \\ &= R_s + \frac{1}{\frac{1}{R_t} + j2\pi f C_i} \end{aligned} \tag{4.13}$$

where Z_s is the impedance of the solution resistance and Z_t is the impedance of the charge transfer resistance. When a direct current (DC) is applied to the electrode, the total impedance could be considered as:

$$Z_{total-DC} = \lim_{f \to 0} (R_s + \frac{1}{\frac{1}{R_t} + j2\pi f C_i}) = R_s + R_t \tag{4.14}$$

And when an alternating current (AC) is applied and the frequency f approaches infinity, the total impedance could be calculated as:

$$Z_{total-AC} = \lim_{f \to \infty} (R_s + \frac{1}{\frac{1}{R_t} + j2\pi f C_i}) = R_s \tag{4.15}$$

Therefore, the characteristic of impedance-frequency is expected to have a non-linear relationship. In this project, the impedance measurement is performed to

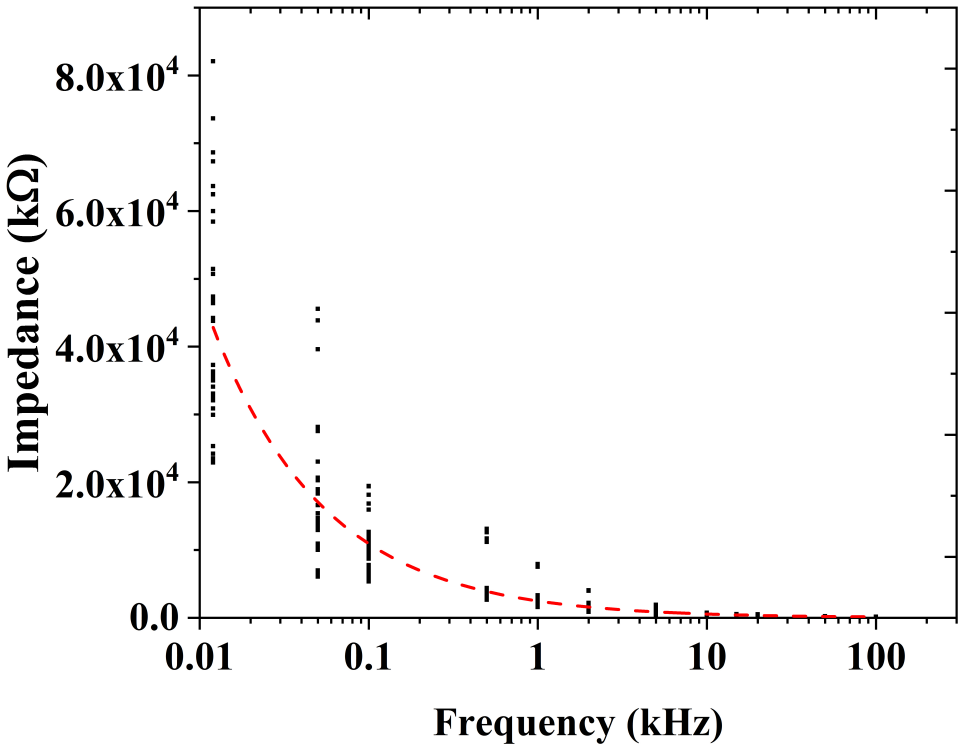

FIGURE 4.23: Impedance as a function of frequency. The 61 penetrating microelectrode array experimental data as shown in black dots and the averaged data are shown by the red dash line.

characterize the electrical response of the penetrating microelectrode array. As shown in Fig. 4.23, impedance from the working electrodes with frequencies from 0.012 kHz to 100 kHz are presented as the black dots and the red dash line indicates the averaged impedance.

However, the impedance of electrode at 1 kHz is about 3000 kΩ (shown in Fig. 4.23). This high electrode impedance may reduce the amplitude of the neural signal and/or introduce additional background noise [142–152]. For the purpose of well-performed neural recordings, the impedance of electrode at 1 kHz should be about 500 kΩ [153, 154]. Therefore, to further reduce the impedance without changing the physical extent (e.g. tip diameter), electroplating is chosen to deposit a thin conductive film onto the electrode. The resulting rough coating increases the surface area of the electrode and so reduces the impedance. Recently, platinum-coated electrodes are widely used in biological experiments due to two properties [139]. First of all, platinum does not react with the biological tissues due to its noble property. Secondly, the electroplated platinum is able to form a granular

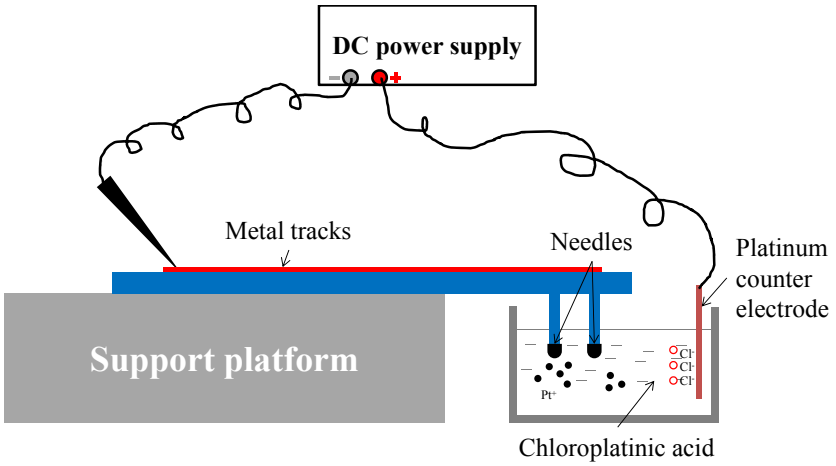

FIGURE 4.24: Schematic of electroplating setup. The needle is connected to the cathode of the DC power supply and the platinum counter electrode is connected to the anode of the power supply. When the current flows in the circuit, an electric field is built to separate the platinum ions (towards the microelectrodes) and chloride ions (towards the platinum counter electrode).

structure on the electrode, which allows an increase in the surface area of the electrode and reduces the impedance at the electrode-tissue interface. Therefore the electrodes in this project are coated by this type of the electroplated platinum which is known as platinum black [155–158].

As mentioned in previous chapter, the setup of electroplating includes a DC power supply, a platinum wire and an electrolyte. Specifically, the setup of electroplating in this project is shown in Fig. 4.24. Needle tips are dipped into the chloroplatinic acid which consists of 1 % platinic chloride, 0.08 % lead acetate and 98.92 % DI (de-ionized) water, and a platinum wire (connected to the anode) acts as a counter electrode. The microelectrode needle is connected to the cathode of the power supply. When a current flows in the circuit, an electric field is built between the anode and the cathode, resulting in movement of platinum ions towards the microelectrode and chloride ions towards the counter electrode. The magnitude of the current flow dictates the surface roughness. Here, a current density of 4 $nA/\mu m^2$ was utilized to form the platinum black on the top of the needle.

After electroplating, the impedance is measured and demonstrated in Fig. 4.25 and an impedance comparison between unplatinized and platinized microelectrode is shown in Fig. 4.26(a). The impedance of the microelectrodes was dramatically reduced. Specifically, the impedance of microelectrodes at 1 kHz is about 450 kΩ (shown in Fig. 4.26(b)), reduced from 3 MΩ. As a result, the penetrating microelectrode array was ready for the neural recording *in vivo* or *in vitro*.

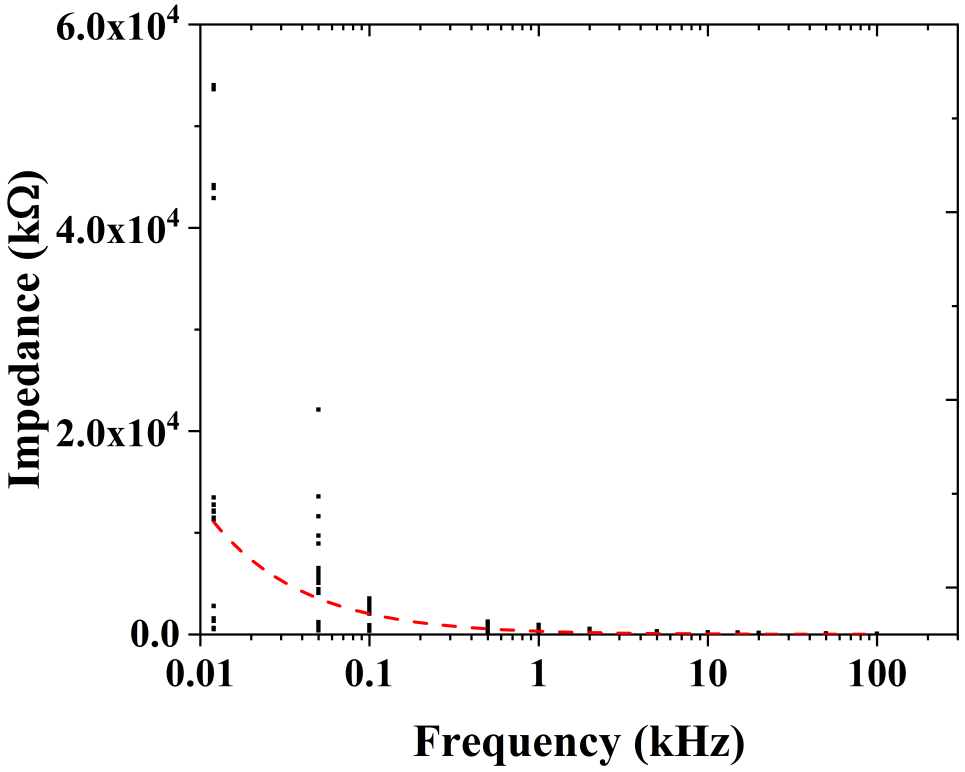

FIGURE 4.25: Impedance as a function of frequency after platinization. The 61 penetrating microelectrode array experimental data as shown in black dots and the averaged data are shown by the red dash line.

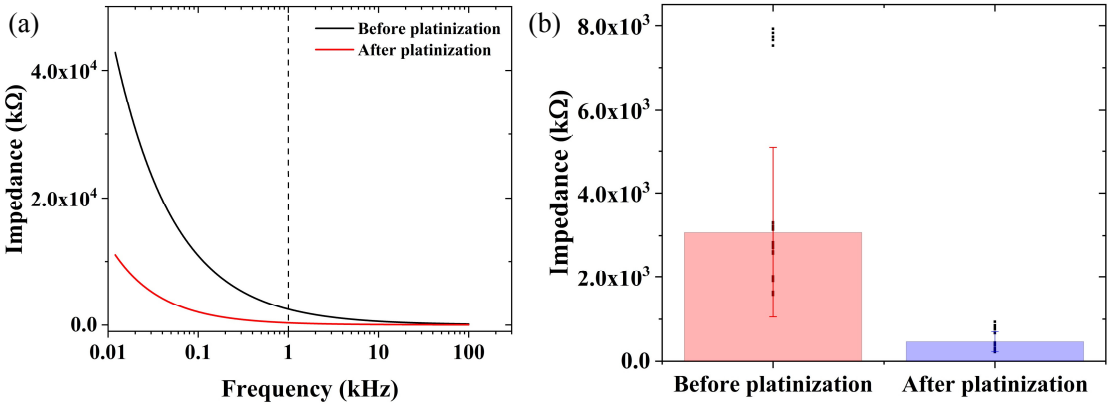

FIGURE 4.26: (a) Impedance comparison between unplatinized and platinized microelectrode array. The black solid line represents the impedance of microelectrode before plaitnization and the red solid line represents the impedance after platinization. The black dash line highlights the impedance of microelectrode at 1 kHz. (b) The impedance comparison between unplatinized and platinized microelectrode at 1 kHz. The red bar demonstrates the impedance measured before platinization (about 3 MΩ) and the blue bar shows the impedance after platinization (about 450 kΩ).

4.4 Summary

In this chapter, the fabrication and characterization of the penetrating microelectrode array is described. Section 4.1 described the design of the penetrating microelectrode array. Then in section 4.2, the fabrication process of the penetrating microelectrode array is explained. In order to improve the fabrication yield of penetrating microelectrode array, some steps such as photolithography and KOH wet etch were optimized to achieve clear pattern transfer and needle exposure with well-protected metal layers. The performance characterization detailed in section 4.3. Compared to the previous studies [59, 139], the electrical performance proves that the penetrating microelectrode array presented here is ready for the neural recording (450 kΩ electrode impedance and 3 pF inter-channel capacitance). However, etch defects were introduced during Si deep reactive ion etch and caused the short circuits between channels. Therefore, as a future plan, the Si deep reactive ion etch will need to be further optimized to improve the etch quality.

Chapter 5

μLED coupled glass optrode array for optogenetics

The work presented in this chapter is to produce a μLED coupled glass optrode array for optogenetics. The design of the μLED array is shown in section 5.1 and the fabrication process is detailed in section 5.2. Before coupling, the electrical and optical performances of the μLED array are described in section 5.3 and the device with a good performance is ready for coupling. The μLED array was then glued to the back plane of Utah glass needle array using an optical glue, which is detailed in section 5.4. The integrated device is then called the optrode array and the optical and thermal performances are demonstrated in section 5.5. The performance of this neural interface device is explored by studying the distribution of light from the tip of a needle and the temperature profile during operation. It can be estimated that a single μLED-coupled needle can activate around 5500 neurons, if the neuronal density is estimated around 10^5 neurons/mm^3[159, 160]. At all times, the resultant average temperature change is less than 1 °C, which is below expected damage thresholds for neurons in the brain [161, 162].

5.1 Design of μLED coupled glass optrode array

As described in previous chapters, optogenetics is another efficient strategy to study information flows in neural circuits by optical stimulation of neurons. In order to deliver light into deep brain regions, the optical guide is required to be long and narrow so that the implantation damage is minimized. Furthermore, the

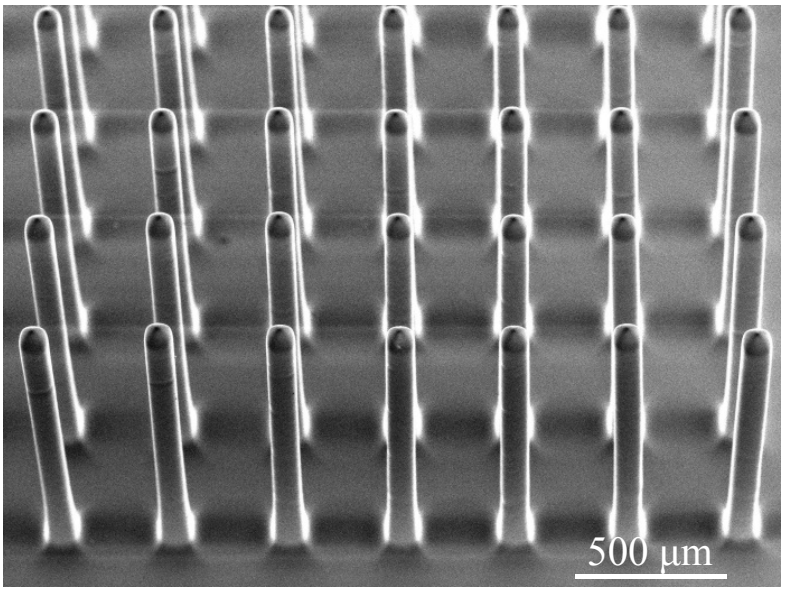

FIGURE 5.1: SEM image of the Utah glass needle array. The array includes 100 needles (10 × 10 array) with 400-μm pitch. Each needle is 1.5 mm long. Scale bar: 500 μm.

light source should be able to provide a light that can be efficiently coupled giving an optical power at the emission point that meets the requirement for optogenetics.

According to the work of Korbinian Brodmann in 1909 [163], the human cerebral cortex is divided into six main layers with an averaged thickness of approximately 2.5 mm (shown in Fig. 5.2) [164–166]. Therefore, the Utah glass needle array utilized in this project is designed to have 100 glass needles with 1.5-mm length and 400-μm pitch (Fig. 5.1) [42, 43], for the purpose of contacting neurons in the layer V and VI of cerebral cortex. When the μLED array is coupled to the Utah glass needle array, the integrated device can provide 181 individually addressable illumination sites (81 for surface illumination and 100 for deep cortex illumination). This ability to produce spatio-temporal patterns of light at two layers within the cortex, promises to help studies aimed at linking the neural activity of small groups of neurons to specific cognitive functions.

In the Utah glass needle array, 100 needles are arranged in 10 × 10 matrix at 400-μm pitch. As a result, the μLED array is designed to include 100 elements that project light into each needle. A secondary pattern of 9 × 9 allows the 81 interstitial sties to facilitate light activation of superficial cortical layers. As shown in Fig. 5.3, the array is designed as a chess-board pattern with two arrays (10 × 10 array and 9 × 9 array) arranging along the diagonal line. Each element has dimensions of 80 μm × 80 μm with 200-μm centre-to-centre distance between

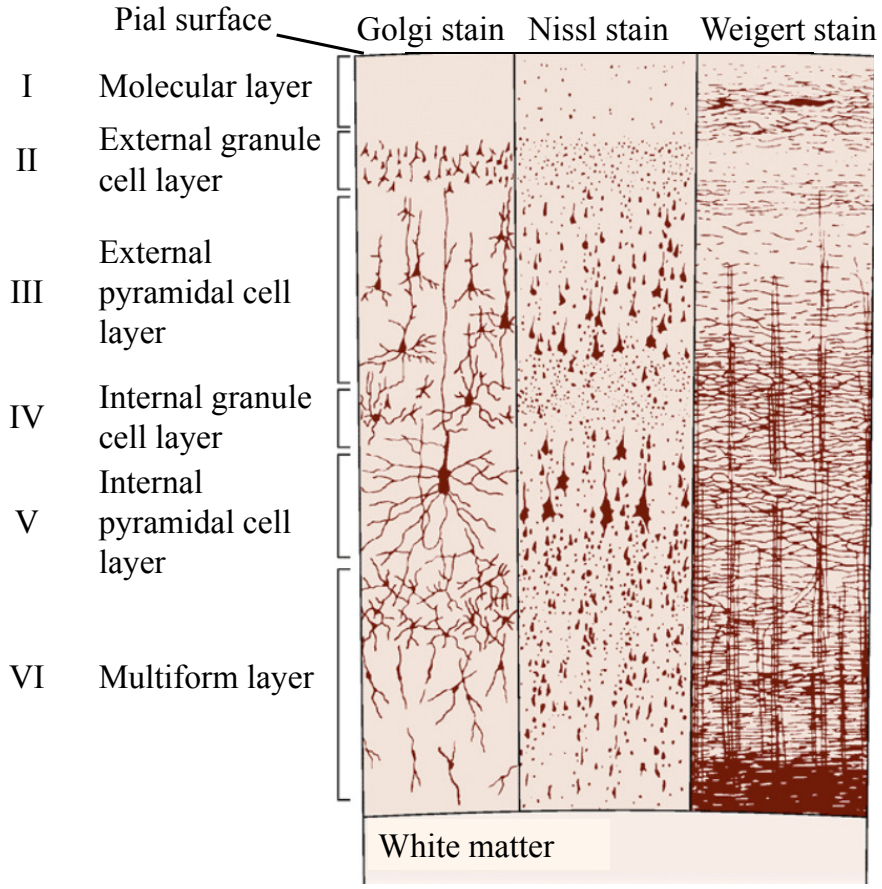

FIGURE 5.2: The cerebral cortex includes six layers and different stains demonstrate different appearance of the cortex. The Golgi stain reveals neuronal cell bodies and dendritic trees. The Nissl method shows cell bodies and proximal dendrites. The Weigert stain is used to reveal the patterns of axonal distribution. After [1, 167].

adjacent elements. Therefore, once the μLED array is integrated with the Utah glass needle array, the 10 $\times$ 10 array is aligned to the needles which allows light to be delivered into the deep brain region. The 9 $\times$ 9 array, on the other hand, is aligned to the gaps between needles to enable interstitial stimulation at the surface region of brain.

According to the structure of the μLED, the μLED element requires two connections: n-type connection (anode) and p-type connection (cathode). Therefore, 362 connections are needed to control 181 elements, resulting in a complicated design for the external driving system. In order to reduce the driving channels, a matrix addressing scheme is introduced to the design. Here the μLED array elements in the same row have a common n-type contact and the ones in the same column have a common p-type contact. Therefore, only m + n control channels are required to

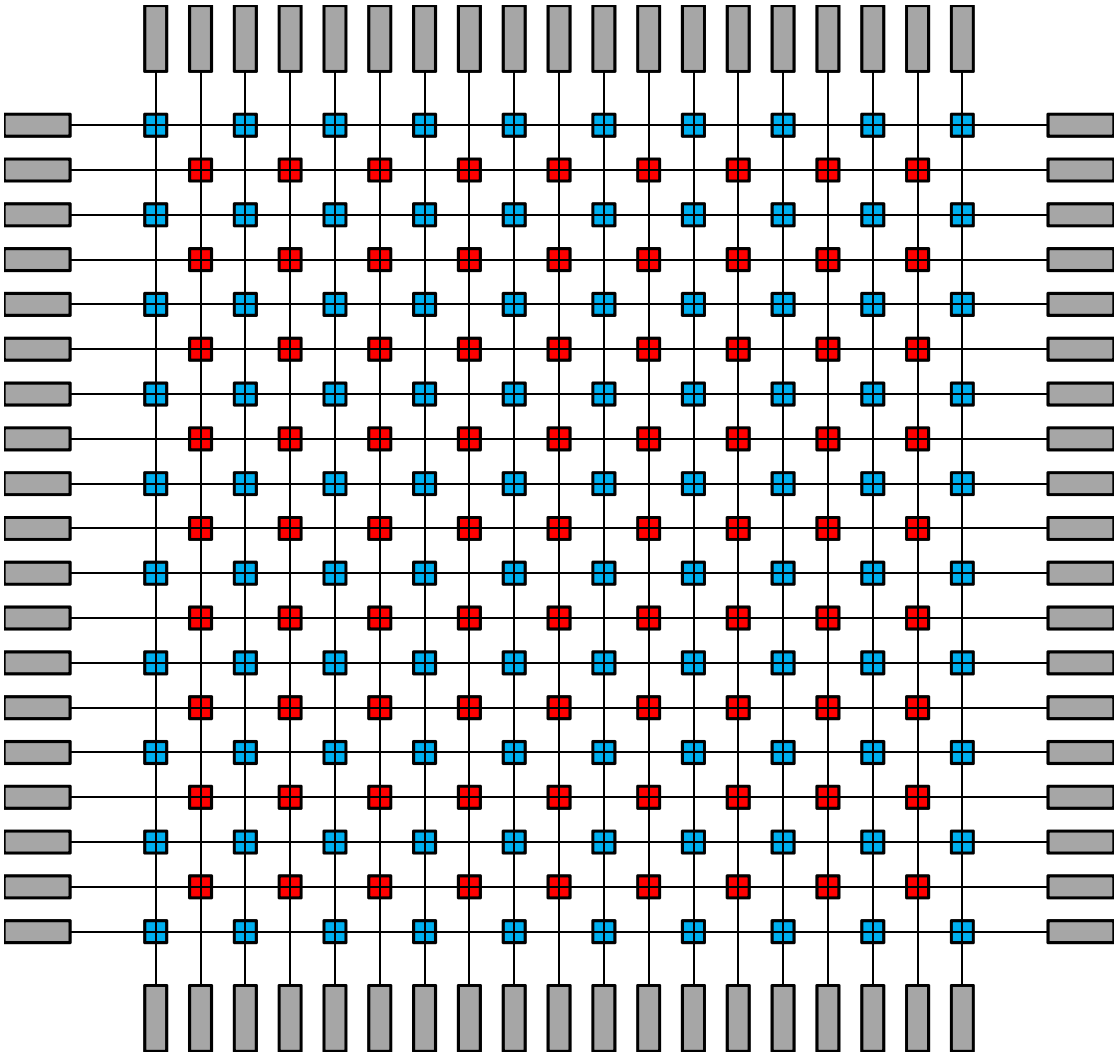

FIGURE 5.3: Design of μLED array. The array in blue are aligned to the glass needle array and the one in red are coupled to the gaps of glass needles.

drive m × n array. As a consequence, 38 connections (19 n-type connections and 19 p-type connections) are involved in connecting the μLED array.

The matrix-addressing scheme enables not only individual controls across the array, but also multiple lighting up of pixels across the array. As shown in Fig. 5.4(a), elements in the same row or column can be lit up simultaneously. Moreover, elements in n × n matrix could also be lit up by connecting n anodes and n cathodes (Fig. 5.4(b)). However, diagonal illumination patterns and simultaneously displayed horizontal and vertical lines are not possible.

According to the design, a set of photomasks for the μLED array are made for the following fabrication. An overview of the photomask is shown in Fig. 5.5.

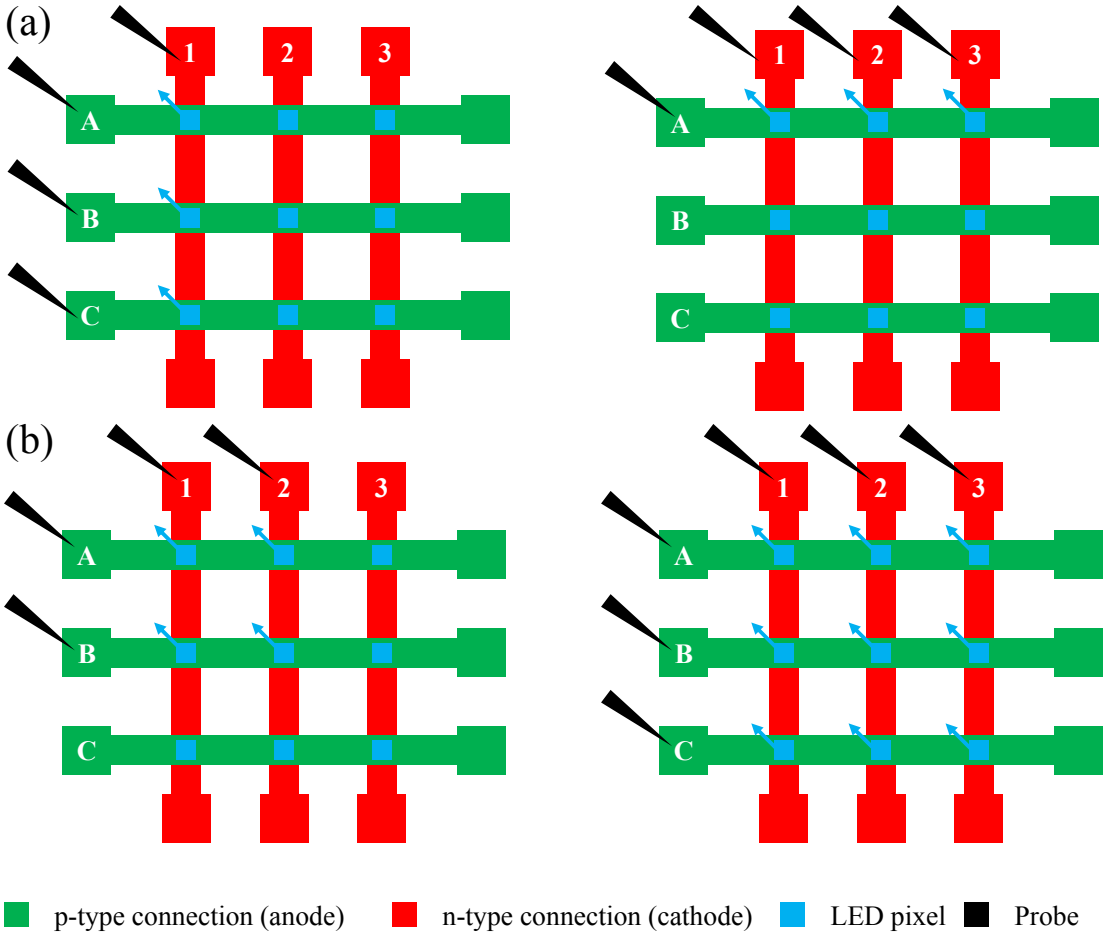

FIGURE 5.4: Schematic of matrix addressable scheme. (a) Lighting-up elements in a row or a column. (b) Lighting-up elements in a 2 × 2 or 3 × 3 array.

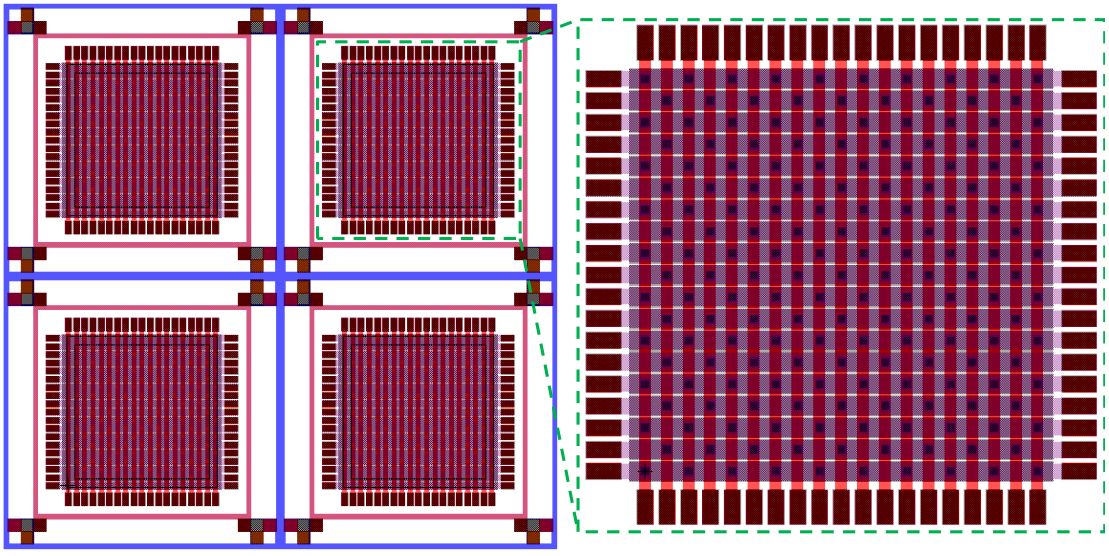

FIGURE 5.5: Photomask design of μLED array. The mask is designed for 15 mm × 15 mm chip which contains 4 devices. The single die is highlighted by the green dash box.

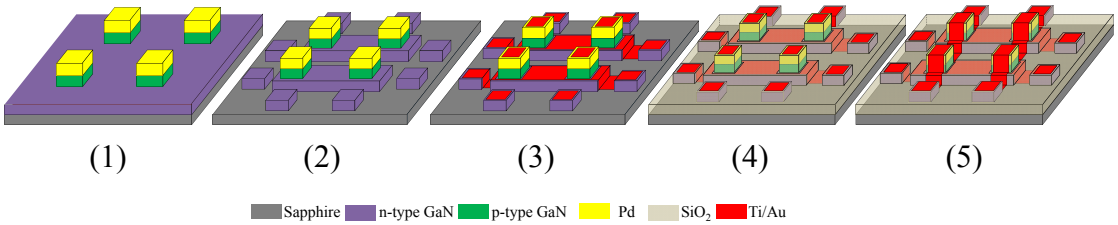

FIGURE 5.6: Fabrication process flow of μLED array. The elements are isolated by GaN etch with a Pd layer on the top (**step #1**). Mesa structures are formed by further GaN etch down to the sapphire substrate (**step #2**). N-type tracks are made of a Ti/Au bilayer (**step #3**). Passivation layer is formed by SiO_2 and vias are opened through the SiO_2 layer for the purpose of metal contacts (**step #4**). P-type tracks are made of a Ti/Au bilayer (**step #5**)

.

5.2 Fabrication process of μLED array

According to the design shown in Fig. 5.5, the fabrication process flow is mapped out and shown in Fig. 5.6. The fabrication starts with 15 mm $\times$ 15 mm GaN-on-Sapphire chip. The p-type contact for each element is firstly created by palladium (Pd) deposition on p-type GaN layer. Then the n-type and p-type GaN layers are etched to create individual element and mesa structure respectively. The n-type tracks and p-type tracks are formed by Ti/Au bilayers and a SiO_2 layer is deposited between them as a passivation layer. The chip is then thinned from the sapphire side and then diced into individual devices. The details of fabrication steps are covered below.

Step #1 The sample is firstly solvent cleaned and then acid cleaned (HCl) to remove the native oxide layer on the GaN. Then a 100-nm thick Pd layer is deposited by electron-beam evaporation process. After Pd deposition, a SiO_2 layer is deposited in PECVD tool as a hardmask for Pd etching. Shipley S1805 positive photoresist is used to pattern the SiO_2 layer. Both SiO_2 and Pd etching are performed in RIE tool and the recipe of Pd etching is shown in Table A.8. Here, the Pd was etched as opposed to a lift-off process, as it can be processed in the same step as the p-type GaN etch. This simplifies the processing.After Pd etching, the sample is directly loaded into the ICP system to form the μLED elements by etching the p-type GaN layer (Fig. 5.7(a)). The etching recipe is shown in Table A.9.

Step #2 After a solvent clean, the sample is loaded into RIE tool to remove the remaining SiO_2 layer (hardmask in step #1) by a dry etching process. A SiO_2

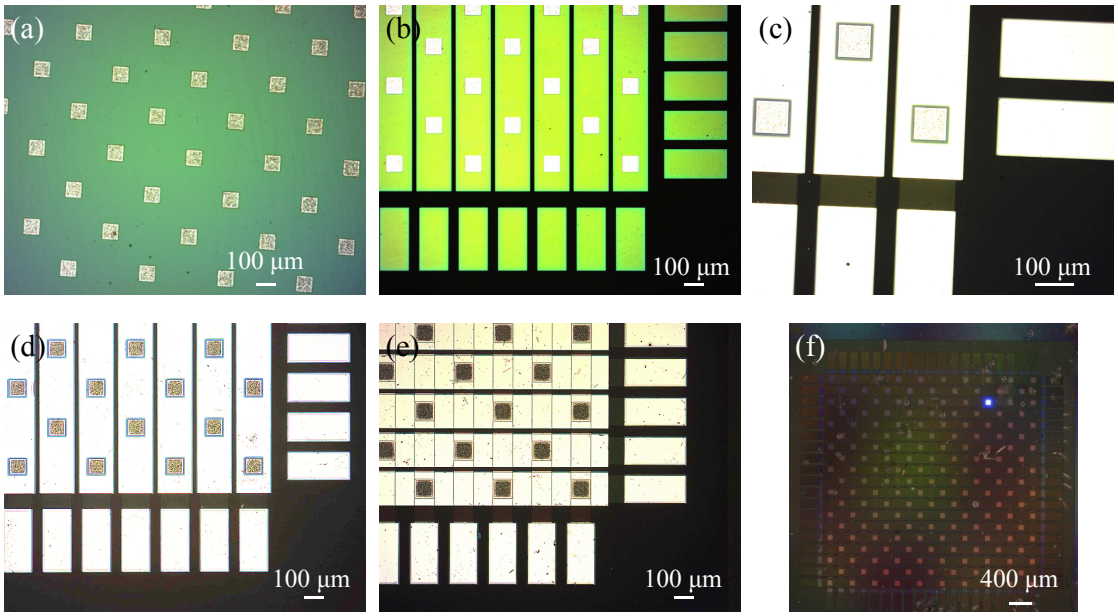

FIGURE 5.7: μLED array fabrication images. (a) Element definition on p-type GaN layer (**Step #1**). Scale bar: 100 μm. (b) Mesa structures on n-type GaN layer (**Step #2**). Scale bar: 100 μm. (c) N-type tracks made of Ti/Au bilayer (**Step #3**). Scale bar: 100 μm. (d) Vias formation on SiO_2 layer (**Step #4**). Scale bar: 100 μm. (e) P-type tracks made of Ti/Au bilayer (**Step #5**). Scale bar: 100 μm. (f) Completed device with one lighting element. Scale bar: 400 μm.

layer is deposited onto the sample by PECVD process. Shipley S1805 positive photoresist is spin coated onto the sample as a softmask in the following SiO_2 etch. The n-type GaN etching is performed in ICP system with the same etching recipe used in step #1 (Fig. 5.7(b)).

Step #3 After n-type GaN etch, the sample is solvent cleaned to remove photoresist residuals. Then the remaining SiO_2 is removed by RIE process. In order to create a metal contact to p-type GaN with a low electrical resistance, annealing is then applied in the RTA equipment. After annealing, SPR220-4.5 photoresist is firstly spin coated onto the sample and patterned by photolithography proesses. Then a Ti/Au bilayer (100 nm/300 nm) is sputter deposited onto the sample. The lift-off process is performed by soaking the sample into the Microposit^{TM} remover 1165 solvent, which is heated up to 80 °C in water bath (Fig. 5.7(c)).

Step #4 After lift-off process, the sample is cleaned by O_2 plasma in a matrix plasma asher system to completely remove the photoresist residuals in order to avoid weak points in the SiO_2 layer, which is deposited onto the sample by PECVD

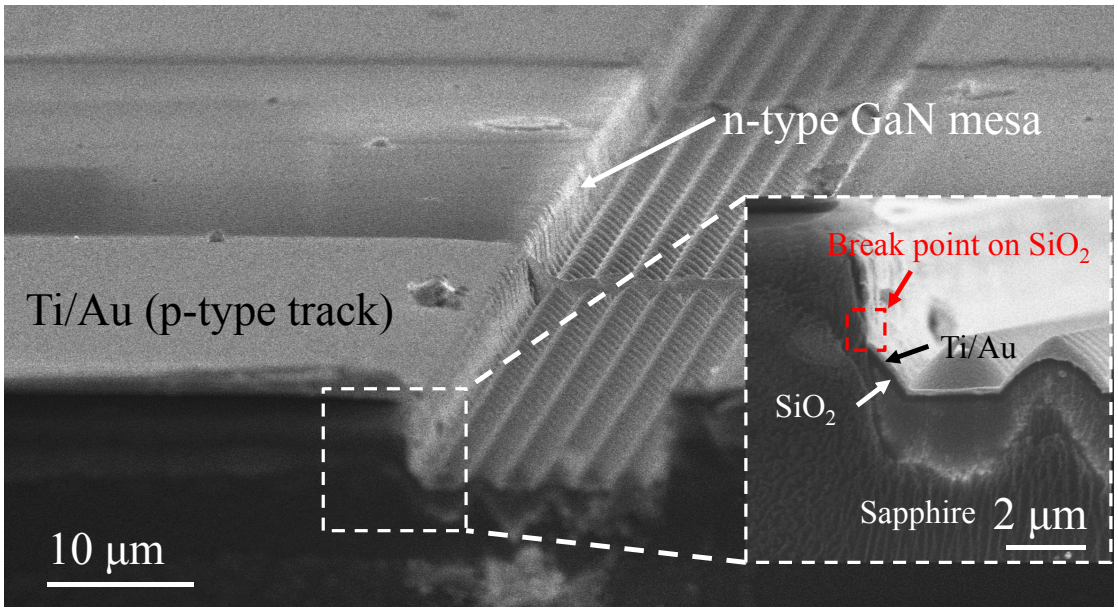

FIGURE 5.8: SEM cross-section image of μLED array. The cross-section is created along the p-type contact. Scale bar: 10 μm; Inset: The close-up image of cross-section. The weak point of SiO_2 layer is highlighted by red dash box. Scale bar: 2 μm.

.

process. Initially, the sample is cleaned by a standard solvent clean process (acetone, methanol and IPA) and break points are found in the SiO_2 layer (as shown in Fig. 5.8). These weak points create short circuits between n-type tracks and p-type tracks. This means that the neighbouring LED element cannot be lit up.

As mentioned in chapter 3, a plasma asher is able to provide higher energy to the chemical reaction of photoresist stripping due to the plasma acceleration (about 600 W RF power) and sample heating (150 °C). This O_2 plasma asher is a better way to remove the photoresist residuals (Fig. 5.7(d)) that cause the shorting of channels.

After deposition, vias are created through the SiO_2 layer on the top of each element via RIE process, while Shipley S1818 positive photoresist is used to mask the SiO_2 layer. After dry etching, the sample is again cleaned by O_2 plasma in matrix plasma asher system (Fig. 5.7(d)).

Step #5 The p-types tracks are created by the lift-off process. Same as step #3, thick SPR220-4.5 photoresist (4.5 μm) is used to form the lift-off layer and the Ti/Au bilayer (50 nm/300 nm) is then sputter deposited on the sample. The lift-off process is accomplished by soaking the sample in the Microposit^{TM} remover 1165

solvent, which is heated up to 80 °C in water bath (Fig. 5.7(e)). The completed device with one lighting element is shown in Fig. 5.7(f).

5.3 Characterization of μLED array

The μLED array is characterized after the fabrication including the fabrication yield and the electrical and optical performance. It is necessary to ensure the device is working properly before integrating with the Utah glass needle array.

5.3.1 Fabrication yield of μLED array

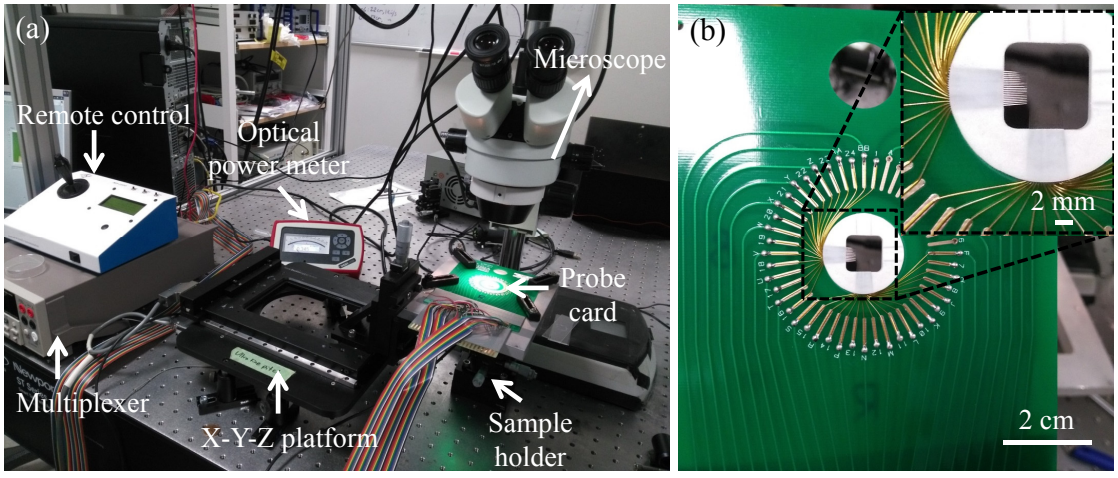

FIGURE 5.9: Home-built setup to check the fabrication yield of μLED array. (a) Setup for I-V measurement of the μLED array. The μLED array is put onto the sample holder while the detector of optical power meter is placed underneath to measure the output power. A customized probe card is fixed onto an X-Y-Z stage to position the probe pins to the μLED array. (b) Image of the customized probe card with 38 pins: 19 cathodes and 19 anodes. Scale bar: 2 cm. (inset) close-up image of the 38 pins. Scale bar: 2 mm.

This device is designed for studies of neural activity in non-human primates. As such, the fabrication steps outlined in previous section are used to produce reliable, high yield devices. In order to ensure the high fabrication yield, each individual μLED array needs to be fully characterized. To calculate the fabrication yield, a home-built system is used to check the status of 181 LED elements across the entire array (Fig. 5.9(a)). A customized probe card with 38 pins (19 pins as cathodes and 19 pins as anodes) was designed, which has the same dimensions as μLED array (Fig. 5.9(b)). Therefore, 38 pins could be simply aligned to the 38 channels

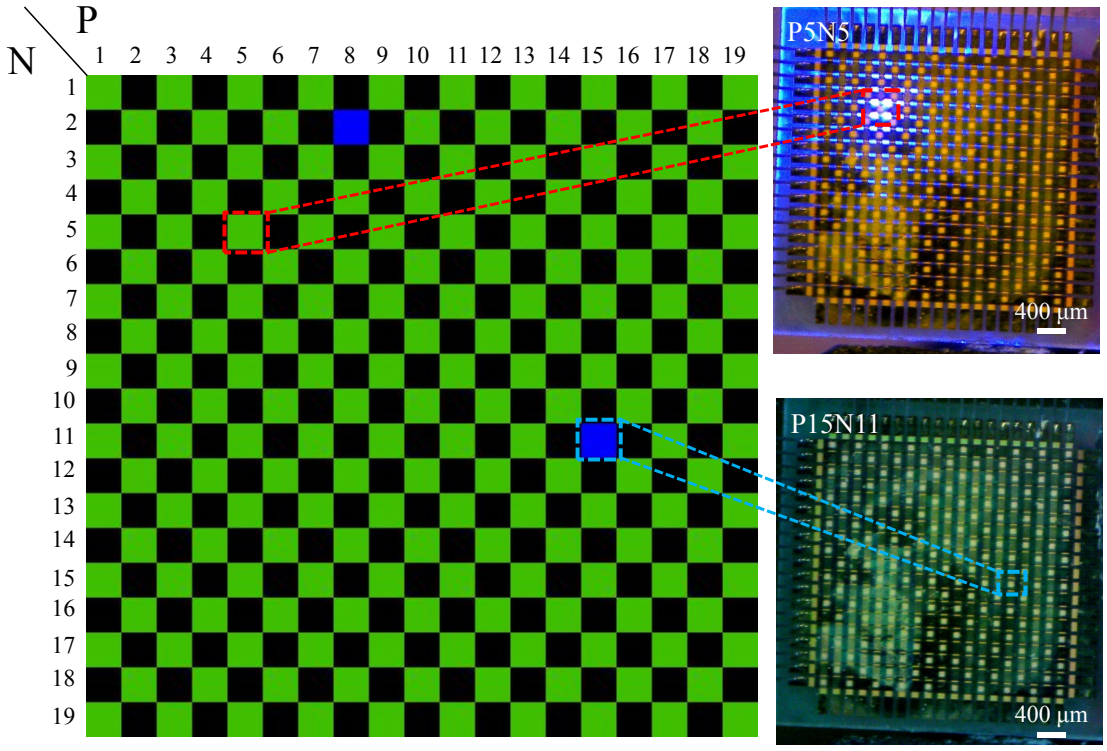

FIGURE 5.10: Colour map of one μLED array created after I-V measurement. Left: Colour map of μLED array to show the working status of each element. The green represents the working LED element. The blue represents the short LED element. The black represents the gap between LED elements. Top right: Back view of a working element highlighted by a red dash box. Scale bar: 400 μm. Bottom right: A short-circuited element highlighted by a blue dash box. Scale bar: 400 μm.

of the μLED array and operate each element at an acceptable current level. In order to achieve an automatic operation, a LabVIEW program is set to control the current source (GS610, Yokogawa), the optical power meter, the multiplexer and the X-Y-Z stage. The program forms a colour map to demonstrate the status of each element with different colours. The map has three level - green, blue and red. The green represents an element with the current-voltage (I-V) characteristic that has an expected exponential forward bias relationship. The blue indicates that the element has a linear I-V characteristic and the red represents the element with an open circuit. Fig. 5.10 shows one test example of one μLED array with two failed elements. In this project, the fabrication yield is achieved over 95 %.

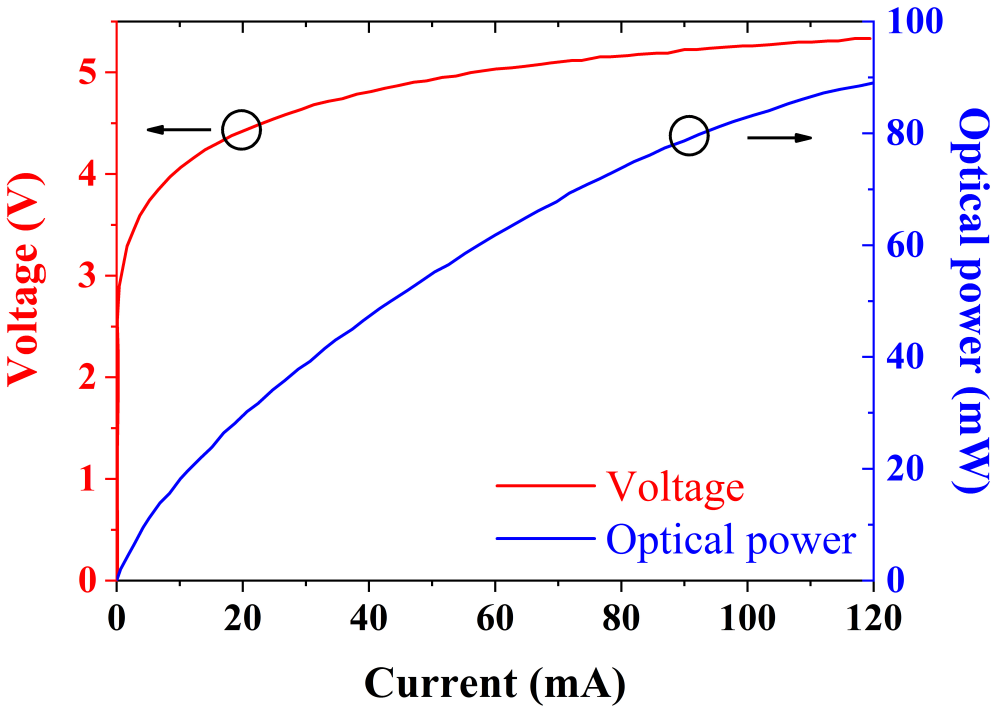

FIGURE 5.11: I-V (red line) and L-I (blue line) characteristics measurement from single element.

5.3.2 Electrical and optical performance of μLED array

Before coupling, the electrical and optical performances of the μLED array are detailed respectively in this section. The I-V and the output optical power-current (L-I) characteristics of a single element is shown in Fig. 5.11. According to the optical model mentioned by McAlinden et, al. [168], the optical power received by the detector is about 11.5 % of the total optical output power [168]. Therefore, the optical output power is approximately 80 mW when the element is driven at 100 mA. Similar results have been achieved in previous studies [169, 170]. As a result, the electrical to optical power conversion efficiency of the device is about 16 %, which matches the typical efficiency of μLED with 450-nm wavelength [171].

As a light source for optogenetics, the μLED array enables the optical stimulation of neurons, not only from a single region, but also from multiple regions. Therefore, it is highly desirable that the μLED array has a uniform electrical and optical performance. In order to demonstrate the uniformity across the entire array, 5 LED elements in a diagonal are randomly selected and operated at the same voltage level (10 V). According to the equivalent circuit model (Fig. 5.12), n-type

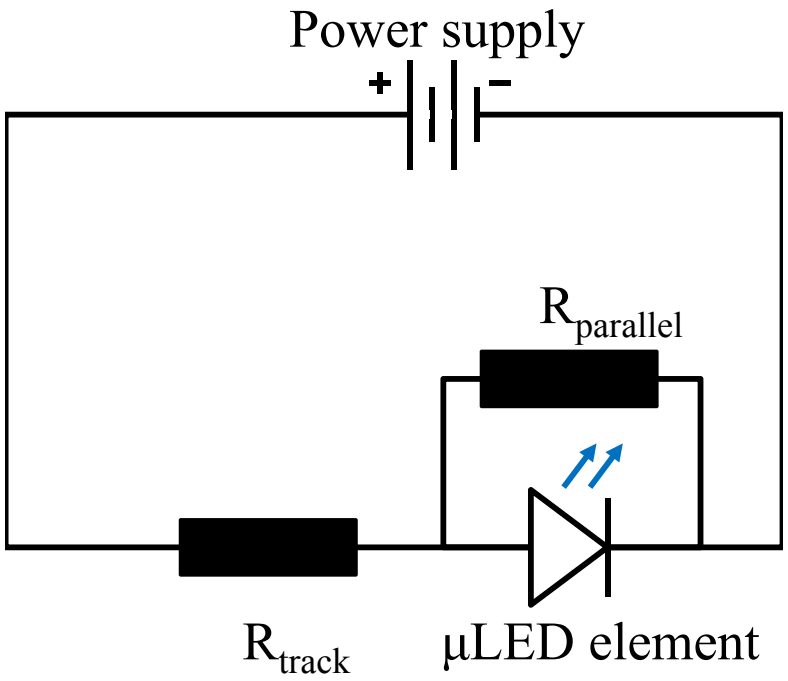

FIGURE 5.12: Equivalent circuit model for single LED element. R_{track} is the resistance of metal tracks in ohm and $R_{parallel}$ is the parallel resistance in ohm.

and p-type contacts and metal tracks are considered as a series resistance R_{series}. From number 1 to number 19, the metal tracks become longer and longer (as shown in Figure 5.13) resulting in higher and higher series resistance. As mentioned in chapter 4, the length of gold tracks to the first element is 800 μm, the thickness of gold layer is 600 nm and the width of gold track is 170 μm. According to the previous studies, the resistivity of gold at room temperature is $2.44 \times 10^{-8}\ \Omega \cdot$ m [172]. Therefore, the resistance of gold track to the first LED element is about 0.19 Ω and the one of 19th element is about 1.9 Ω. If the LED element is driven by the voltage source (10V), the current flowing through the LED element will decrease due to the increase of the series resistance and then will lead to a reduction on the optical out power (Fig. 5.14). On the contrary, current driving strategy (20 mA) is able to keep a stable optical output from each LED element in the array (Fig. 5.15).

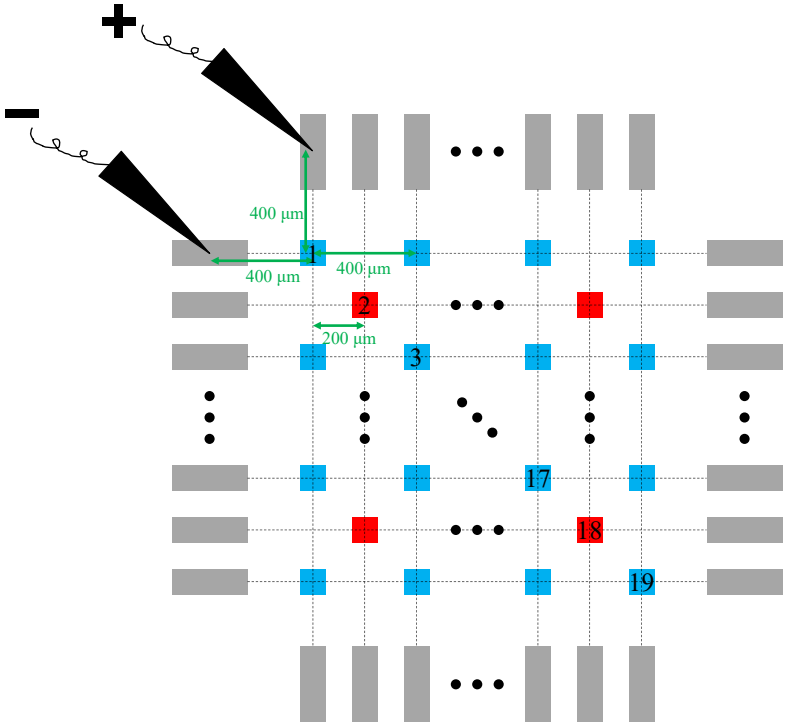

FIGURE 5.13: The blue squares represent LED elements aligned to the needles and the red squares indicate the interstitial LED elements. According to the design, the length of metal track becomes longer and longer from the first LED element to the 19th LED element.

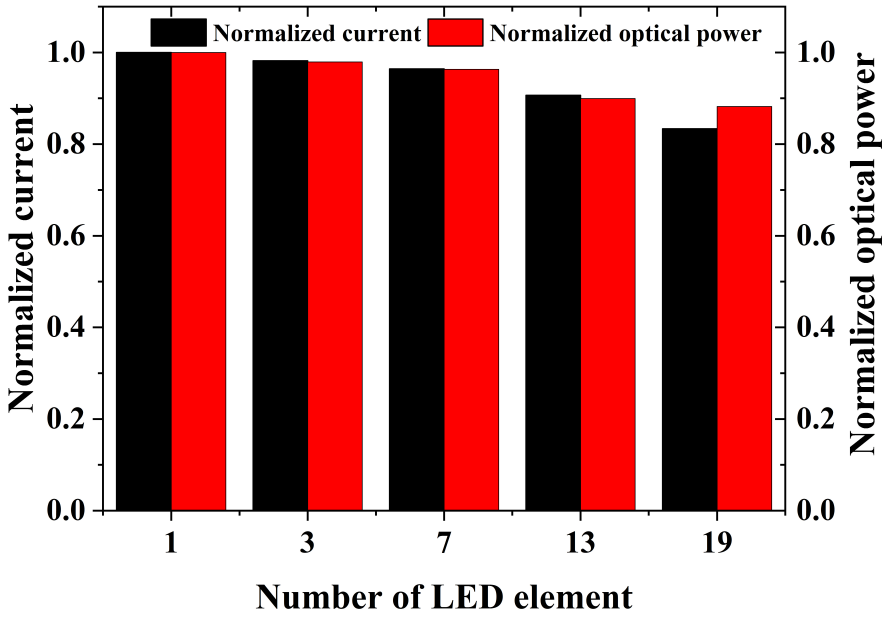

FIGURE 5.14: Uniformity of the electrical and optical performance across the array. 5 elements (#1, #3, #7, #13 and #19) are operated at 10 V. Longer metal tracks are, lower current is achieved through the element (black bars), resulting in a reduction of optical power across the array (red bars).

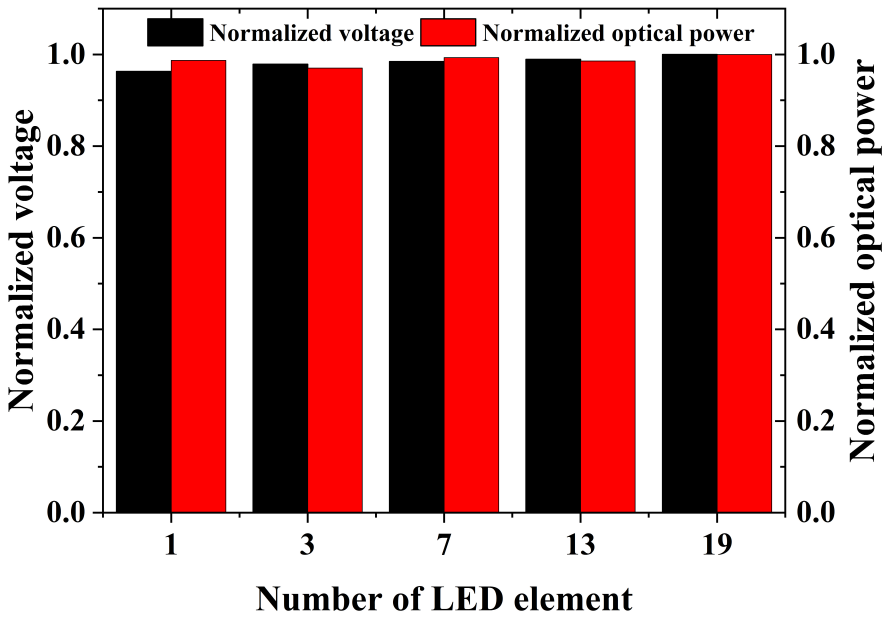

FIGURE 5.15: Uniformity of the electrical and optical performance across the array. 5 elements (#1, #3, #7, #13 and #19) are operated at 20mA. Longer metal tracks are, higher voltage is achieved through the element (black bars). The optical power across the array is steady due to the constant current input (red bars).

5.4 Integration of the μLED array and the Utah glass needle array

To accomplish the integration of the μLED array with the Utah glass needle array, an aligning setup was built and is shown in Fig. 5.16(a). The μLED array and the Utah glass needle array were placed on holder A and holder B respectively. Holder A is free to move using an X-Y-Z stage while holder B is fixed. To tightly couple the μLED array and the Utah glass needle array, a glue with high optical transmission to blue light is required. Furthermore, the glue should have a relatively low viscosity to form a thin uniform adhesion layer between the μLED array and the Utah glass needle array. According to the data sheet, Norland Optical Adhesive (NOA) 61 has a transmission of blue light (450 nm) of over 95 % and a viscosity of about 300 cps, making it ideal for utilizing in this project.

Once the μLED array is fixed onto holder A by vacuum with the sapphire substrate facing up, a 1 ml bead of NOA 61 was dispensed in the centre of sapphire substrate by syringe to avoid bubble generation. The Utah glass needle array was then put

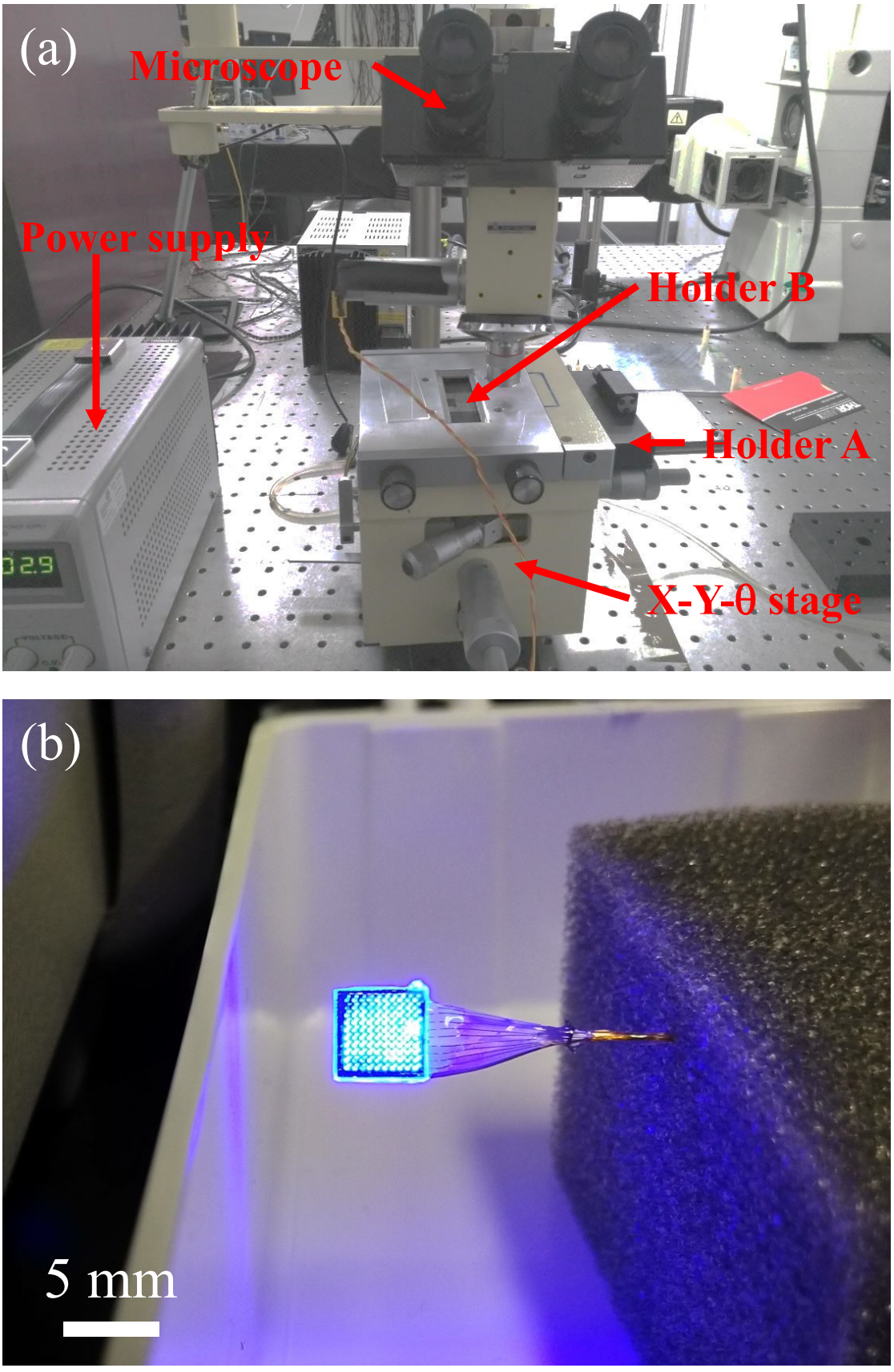

FIGURE 5.16: Integration of the μLED array with the Utah glass needle array. (a) A home-built aligning setup for the integration process. The μLED array and the Utah glass needle array are fixed onto the holder A and B respectively. (b) An overview of μLED coupled glass optrode array with all pixels lighting up to show a good result of integration. Scale bar: 5 mm.

on holder B with tips vertical. During the aligning process, holder A could be brought close to holder B so that the μLED array and the Utah glass needle array could be imaged together and positioned using the X-Y-Z stage. Once the two arrays were precisely aligned, holder A was further lifted towards holder B so that the arrays were fully in contact. An ultraviolet (UV) lamp is then used to fully cure the NOA 61 to obtain full adhesion. The integration result is shown in Fig. 5.16(b) with all μLED pixels lit up.

5.5 Characterization of μLED coupled glass optrode array

The μLED coupled glass optrode array is characterized to demonstrate both optical performance and thermal performance, which are two main properties for optogenetics. The optrode array is expected to provide sufficient light output to activate light-sensitive proteins without heating the brain tissue.

5.5.1 Optical performance of μLED coupled glass optrode array

According to the design, the light could be either guided into the targeted region of brain to achieve deep brain stimulation via glass needles (Fig. 5.17(a)), or could enable the superficial stimulation at the surface of cortex (Fig. 5.17(b)). However, the light from an μLED element is emitted at all angles, i.e. the μLED element is a Lambertian emitter. Therefore, the further it is away from the μLED element, the wider the spread of light. In the optrode array, the μLED array is about 300 μm away from the Utah glass needle array due to the sapphire substrate (about 150 μm thick) and the glass backplane (about 150 μm thick). As a result, the light is scattered when propagating through the sapphire substrate and the glass backplane, which leads to optical cross-talks between adjacent glass needles. Light is not only delivered into the brain tissue via the aligned needle, but also delivered by neighbouring needles due to light spread in the sapphire substrate and the glass backplane.

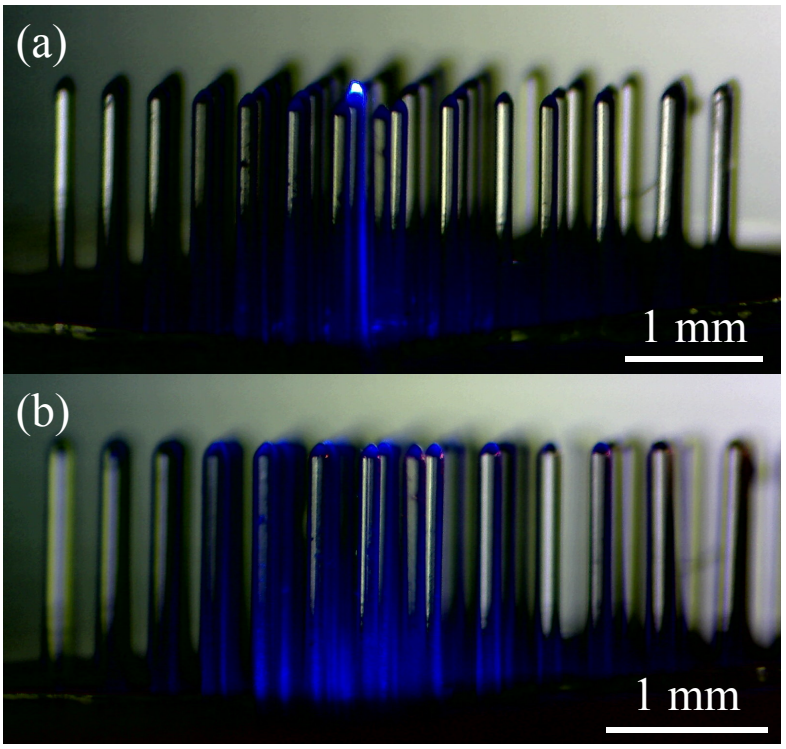

FIGURE 5.17: Two types of stimulation achieved by the μLED coupled glass optrode array. (a) Light coupled into the glass needle to achieve deep brain stimulation. Scale bar: 1 mm. (b) Light emitted from the gap of needles to enable superficial stimulation. Scale bar: 1 mm.

In order to prevent the light from escaping to outside of the needle, a thin metal blocking layer is added to the interface between the μLED array and the Utah glass needle array (Fig. 5.18). For a better comparison, half area of the μLED array is covered by the metal layer and the pinholes are opened for optrode elements ($80 \times 80\ \mu m^2$) and superficial elements ($40 \times 40\ \mu m^2$). As shown in Fig. 5.19(a) and (b), light from the optrode element and the superficial element demonstrate wider emission profiles without the pinhole layer. On the contrary, when the pinhole structure is added to the element, it prevents light from coupling into neighbouring needles. This improves the spatial resolution of optical stimulation. (Fig. 5.20(a) and (b)).

To further investigate the emission profile, the distribution of light from the needle tip is experimentally obtained by introducing fluorescence. Fluorescein sodium ($C_{20}H_{10}Na_2O_5$), one of the commonly used fluorescent tracers, is used in this project to reveal light emission profiles. The peak absorption of fluorescein sodium ranges from 460 nm to 490 nm depending on the pH value and the concentration of solution [173]. Here, a concentration of 0.5% fluorescein sodium solution is applied

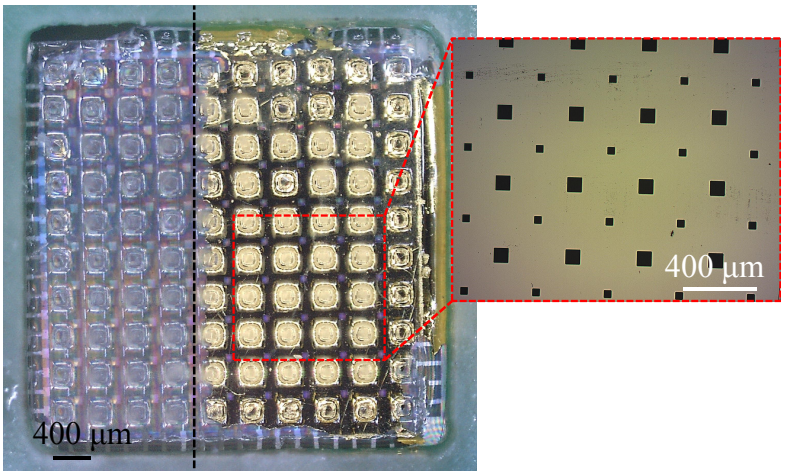

FIGURE 5.18: μLED-coupled optrode array with a metal pinhole layer at the interface between the μLED array and the Utah glass needle array. The black dash line shows the boundary of metal pinhole layer: metal pinhole layer covers the right and the left area is left blank. Scale bar: 400 μm. The close-up image highlighted by a red dash box. Pinholes with 80 × 80 μm^2 are aligned to glass needles and the ones with 40 × 40 μm^2 are aligned to the interstitial regions of glass needles. Scale bar: 100 μm.

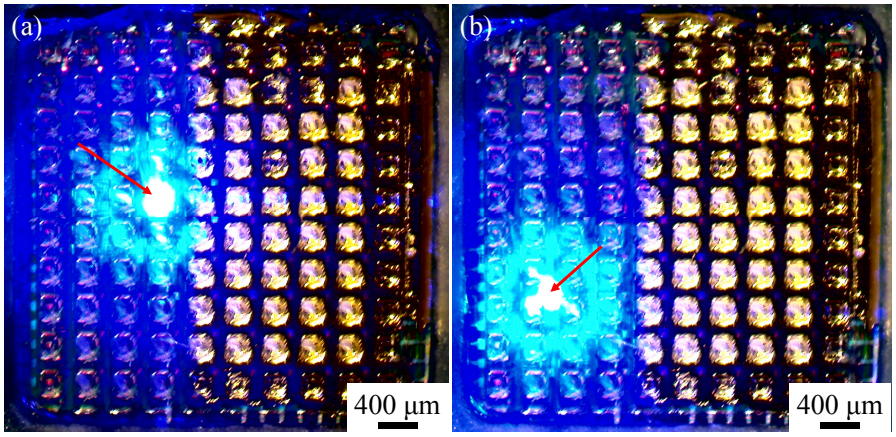

FIGURE 5.19: Light emission profiles from the optrode element and the interstitial element without the pinhole structure. (a) The light is scattered and coupled into the aligned needle (labelled by a red arrow) and the neighbouring needles. Scale bar: 400 μm. (b) Broad emission profile is formed due to the scattering in the sapphire substrate and the glass backplane. The red arrow points out the lighted interstitial element. Scale bar: 400 μm.

to check the light beam profile. The optrode array is placed on an X-Y-Z stage so that it could freely move in all directions at a constant speed (shown in Fig. 5.21). Therefore, it is available to adjust the position of the optrode array in the solution to get a better view from the camera (Fig. 5.22).

When the optrode array is dipped into the fluorescein sodium solution, an image of clear the paths is obtained by the digital camera. Two optrode elements were

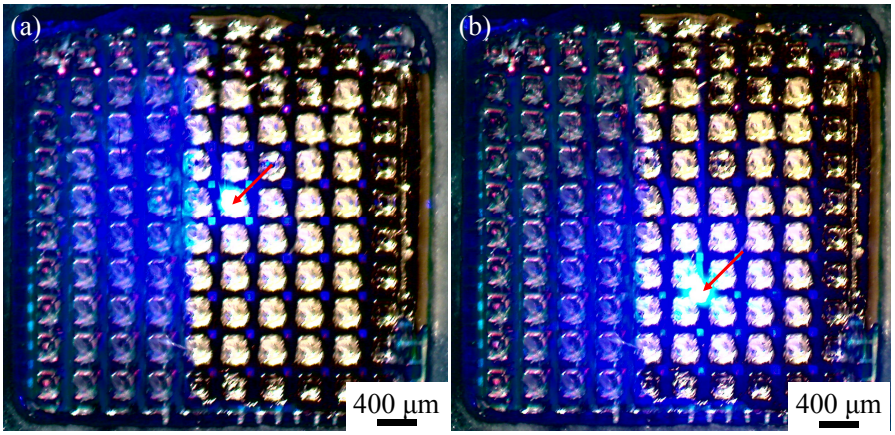

FIGURE 5.20: Light emission profiles from the optrode element and the interstitial element with the pinhole structure. (a) The light emitted from the optrode element (labelled by a red arrow) is confined at the needle tip. Scale bar: 400 μm. (b) Collimated light emission profile is achieved by the interstitial element with pinhole structure (highlighted by a red arrow). Scale bar: 400 μm.

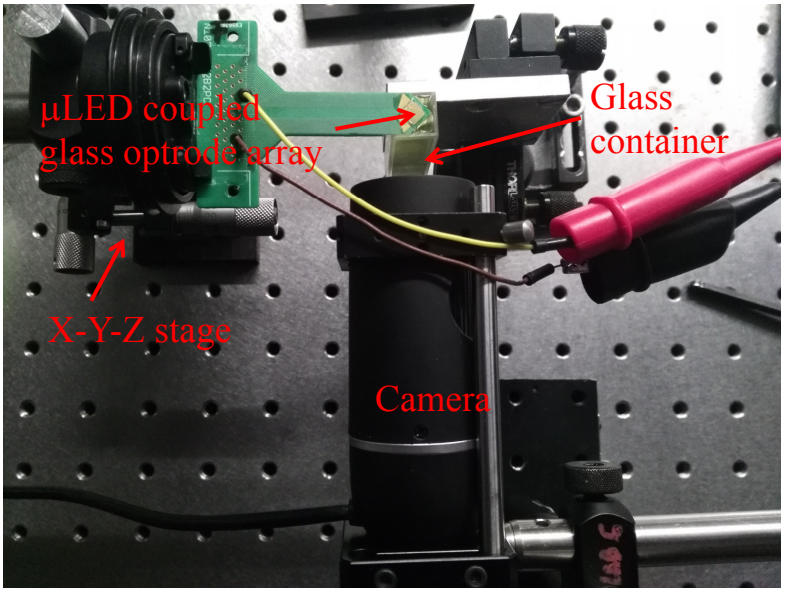

FIGURE 5.21: Setup for investigation on light beam profile. The μLED coupled glass optrode array is fixed onto an X-Y-Z stage which provides horizontal and vertical movements and the camera is set to offer a side view.

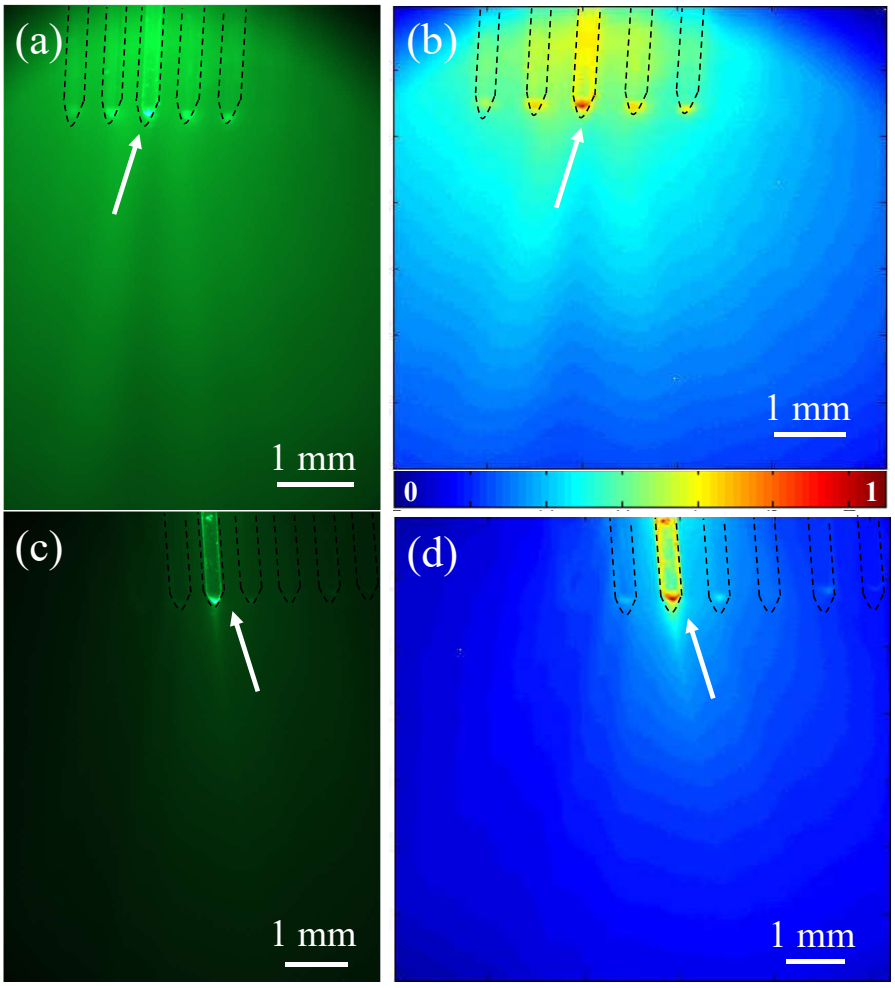

FIGURE 5.22: Light emission profiles of the optrode array with and without pinhole structures. Glass needles are labelled by black dash lines and the lighted optrode element is highlighted by the white arrow. (a) Single lighted optrode element without pinhole structure. The light distribution is revealed in the fluorescein sodium solution. The light scattering in the glass backplane causes the light coupling into the adjacent needles. Scale bar: 1 mm. (b) Colour map of light distribution with normalized optical power intensities. The intensities of light around five needles are in the same level, resulting in a broad emission profile. Scale bar: 1 mm. (c) Single lighted optrode element with pinhole structure. The light distribution is revealed in the fluorescein sodium solution. The light scattering is eliminated so that less light is coupled into the adjacent needles. Scale bar: 1 mm. (d) Colour map of light distribution with normalized optical power intensities. Restricted beam profile is formed near the tip of lighted needle. Scale bar: 1 mm.

driven at 20 mA: without pinhole structure and with pinhole collimation (Fig. 5.22(a) and (c) respectively). When there is no pinhole structure, the light is coupled into the neighbouring needles and emitted out from multiple tips. Moreover, background illumination is introduced by the scattering in the glass backplane so that the spatial selectivity of optical stimulation in brain tissue is limited. On the contrary, the back scattering could be eliminated by the pinhole structure so that the optical cross-talk is avoided. Furthermore, colour maps are obtained from the light path images to demonstrate the light beam distributions from two types of elements (Fig. 5.22(b) and (d) respectively). The distributions are plotted according to the normalized optical intensities from 0 to 1. The needles are labelled by black dash lines and the lighted needle is highlighted by the black arrow. In Fig. 5.22(b), the light is not only guided by the aligned needle, but also coupled into the neighbouring needles. The light emitted from the neighbouring needles show the same level of optical intensity as the one from aligned needle. Thus, when one optrode element is lit up, neighbouring optrode elements are simultaneously lit up due to the optical cross-talk. A broad emission profile is achieved so that the spatial resolution of optical stimulation is reduced. On the other hand, restricted emission profile is formed at the region near the lighted needle (Fig. 5.22(d)). The scattering in the glass backplane is avoided by the pinhole structure so that less light is coupled into the adjacent needles. Therefore, higher spatial resolution is achieved with pinhole structures.

On the other hand, agarose with fluorescein sodium solution is used to characterize the mechanical stability of the optrode array. Low concentration agarose usually acts as a surrogate of the physical characteristics for brain tissue and the light path will be revealed due to the doped fluorescence sodium solution [174]. Therefore, a proper size of agarose cuboid (length $\times$ width $\times$ height = 1.2 cm $\times$ 1.2 cm $\times$ 4.5 cm) was prepared in this project doped by the fluorescein sodium solution with a concentration of 0.5 %. After the test, the optrode array was found to be able to penetrate into the agarose gel without damage.

In addition, the output optical power at the needle tip is measured by an optical power meter. As mentioned in the previous section, a current source is used to operate the μLED coupled glass optrode array to achieve stable optical outputs. With one optrode element lit up (by applying a current from 0 to 100 mA) the optical power climbs up to 0.187 mW (Fig. 5.23). The coupling efficiency of the integrated optrode array is about 0.22 %, which matches the value obtained

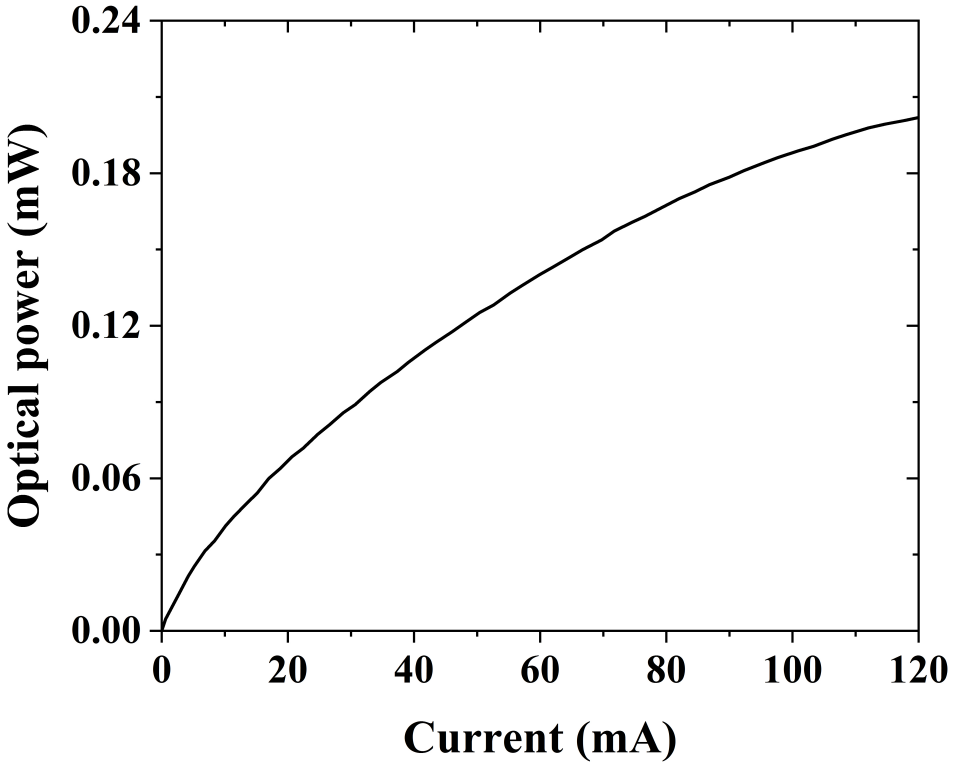

FIGURE 5.23: Output optical power at the tip of the needle of the optrode array is plotted as a function of current.

from the optical model [168]. Regarding the surface area of the needle tip, the irradiance at the needle tip is approximately 80 mW/mm^2, which is appropriate for optogenetic applications [74, 175, 176].

5.5.2 Thermal performance of μLED coupled glass optrode array

Thermal performance is one of the most important characteristics for the μLED-based devices, especially μLED-based optogenetic devices. As introduced in previous chapters, not all of the electrical energy is transformed into optical energy and part of energy becomes heat that spreads over the whole LED device. In previous studies, the μLED components are implanted into the brain tissue along with the carrier. Therefore, the heat generated from μLED elements directly propagates into the brain tissue and neurons may be damaged if the element is overheated [177–179]. In this project, the μLED array is coupled to the Utah glass needle

array so that only the needle array is implanted into the brain tissue. Hence, the heat generated could be introduced into the tissue along the glass needle. Glass is a material which has a low thermal conductivity. As a consequence, the heat does not transmit rapidly across the glass backplane and the glass needle. However, it takes longer time for glass to be cooled down once the glass is heated up due to its small heat capacity. The optrode array could be operated at 20 mA in a duty cycle of 10 % without triggering more than 1 °C increasing in this project and the measurement is detailed in this section.

5.5.2.1 Mechanisms of thermal measurement

According to the black body radiation law, objects with a certain temperature emit infrared radiation. The amount of radiation energy increases when the temperature of object increases. Therefore, to record and analyze the radiation energy, a thermal camera working in a wavelength from 9 μm to 14 μm, is utilized to detect the radiation. Typically, a thermal camera mainly includes three components: an optical system with a set of optical lens to collect the emitted infrared light; a infrared detector to convert optical signals into electric signals and a signal processor to process the electrical signals to create images or plots which contain temperature information.

In this project, a forward-looking infrared (FLIR) SC7600BB infrared camera is used to sense the infrared radiation from the lighted optrode element of μLED coupled glass optrode array. The camera features a Indium Antimonide (InSb) sensor with resolution of 640 × 512 pixels and enables a broad measurement range of temperature from 5 °C to 300 °C with a sensitivity of 20 mK [180]. Before thermal measurement, the camera is calibrated by using a thermocouple. The thermalcouple is an electrical device consisting of two conductive wires that form an electrical junction. The thermocouple is able to produce a temperature-dependent voltage based on the thermoelectric effect. The thermoelectric effect is a direct conversion between temperature change and voltage difference [181]. Therefore, the voltage is then a function of the temperature at the joint of the two wires. and so the voltage is then a function of the temperature at the joint of the two wires.

Typically, the thermocouple is categorized into different types based on the materials of wires: noble metal wires, base metal wires, high temperature or refractory metal wires and non-metal wires [182]. Here, a type-E thermocouple with Nickel

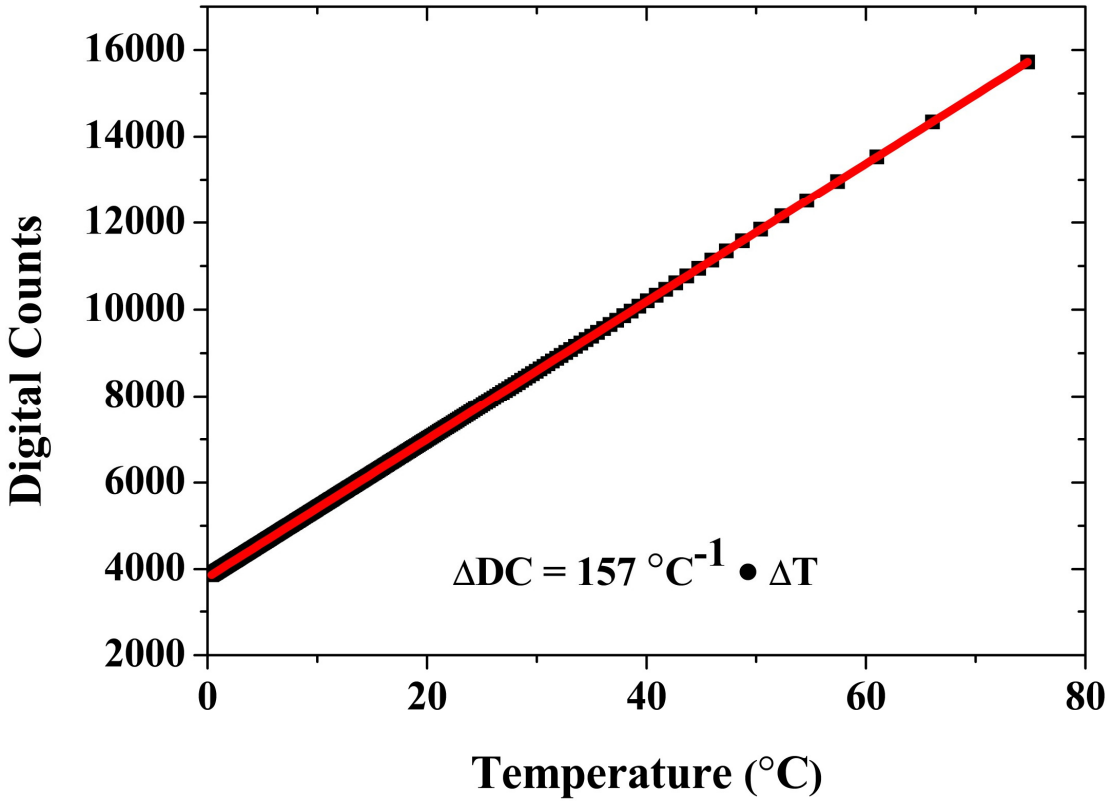

FIGURE 5.24: Calibration of the thermal camera. When the temperature increases 1 °C, the digital count increases 157 in response.

and Chromium wires is utilized to characterize the performance of the thermal camera. The thermocouple can provide a temperature measurement from -270 to 900 °C based on the voltage change. In order to perform the calibration, the thermocouple is placed on a glass microscope slide by a thermal tape and then focused by the thermal camera. The temperature of glass slide is increased to 100 °C by a heating gun. Then the heating gun is released to let the glass slide cool down to the room temperature. The heating and cooling step are repeated for several times to create a plot of digital counts vs temperature (Fig. 5.24).

A linear fit is applied to obtain that the conversion factor between digital counts and the temperature and the relationship can be written as:

$$\Delta DC = 157°C^{-1} \times \Delta T \tag{5.1}$$

where ΔDC represents the change in digital counts and ΔT represents the change in temperature. Therefore, the digital counts changes 157 as a response of 1 °C change in temperature.

5.5.2.2 Thermal performance of μLED coupled glass optrode array

According to the design of μLED coupled glass needle array, only glass needles are inserted into the brain tissue. Therefore, the temperature is measured at the needle tip. For the purpose of neuronal activation in optogenetic applications, periodic pulses of light with a given pulse width (ranging from 1 to 200 ms) and frequency (ranging from 1 to 20 Hz) [183] are required. The thermal measurements detailed here are performed over this range.

As mentioned before, overheating of the optrode array should be avoided and a threshold of temperature change in brain tissue is often set at 1 °C [184–187]. Based on the design, the optrode array enables either individual or multi-site stimulation. Therefore, the thermal measurement is carried out for both single and multiple activated optrodes.

Thermal measurement on a single activated optrode

This thermal measurement is performed in air at room temperature. To operate the μLED coupled glass optrode array, a GS610 Yokogawa current source is utilized to drive an optrode in pulsed mode. Thermal measurements were performed at 20, 50 and 100 mA (corresponding to 30, 55 and 80 mW/mm^2 respectively). The pulse mode was set at different pulse widths (*PW*, 1, 2, 5, 10, 20, 50, 100 and 200 ms) and frequencies (*f*, 1, 2, 5, 10 and 20 Hz). As shown in Fig. 5.25(a), (b) and (c), a higher amplitude current results in a greater change in temperature at the needle tip. At a constant current level, the heat generation is affected by the pulse width and the frequency. For a given frequency, the amount of generated heat decreases while the pulse width reduces. As an example, the optrode was driven at 20 mA with 1 Hz, the temperature is increased by about 3.5 °C when the pulse width is set to 200 ms. Once the pulse width decreases to 1 ms, less rise in temperature (0.1 °C) is recorded at the needle tip. When the frequency of current supply is set to 2, 5 and 20 Hz, the amount of temperature increase at the needle tip is also reduced with the decrease of the pulse width. A similar decreasing trend is observed when the optrode is operated at different current level (50 and 100 mA) with same frequencies (1, 2, 5, 10 and 20 Hz) and pulse widths (1, 2, 5, 10, 20, 50, 100 and 200 ms).

According to the Fig. 5.25, the relationship between the temperature change and the pulse width of current supply at a certain amplitude (20, 50 and 100 mA) and a given frequency (1, 2, 5, 10 and 20 Hz) is linear in logarithm scales. In order to further investigate the thermal performance of optrode array, the temperature change (ΔT) was plotted as a function of the duty cycle (D) (as shown in Fig. 5.26). Similarly, the relationship between temperature change and duty cycle is linear in logarithm scales. Therefore, if a represents the intercept on y-axis (temperature change) and b is the slope of the line. Then the relationship can be written as:

$$10^{\Delta T} = 10^{a+b\times D} \tag{5.2}$$

which can be rearranged to:

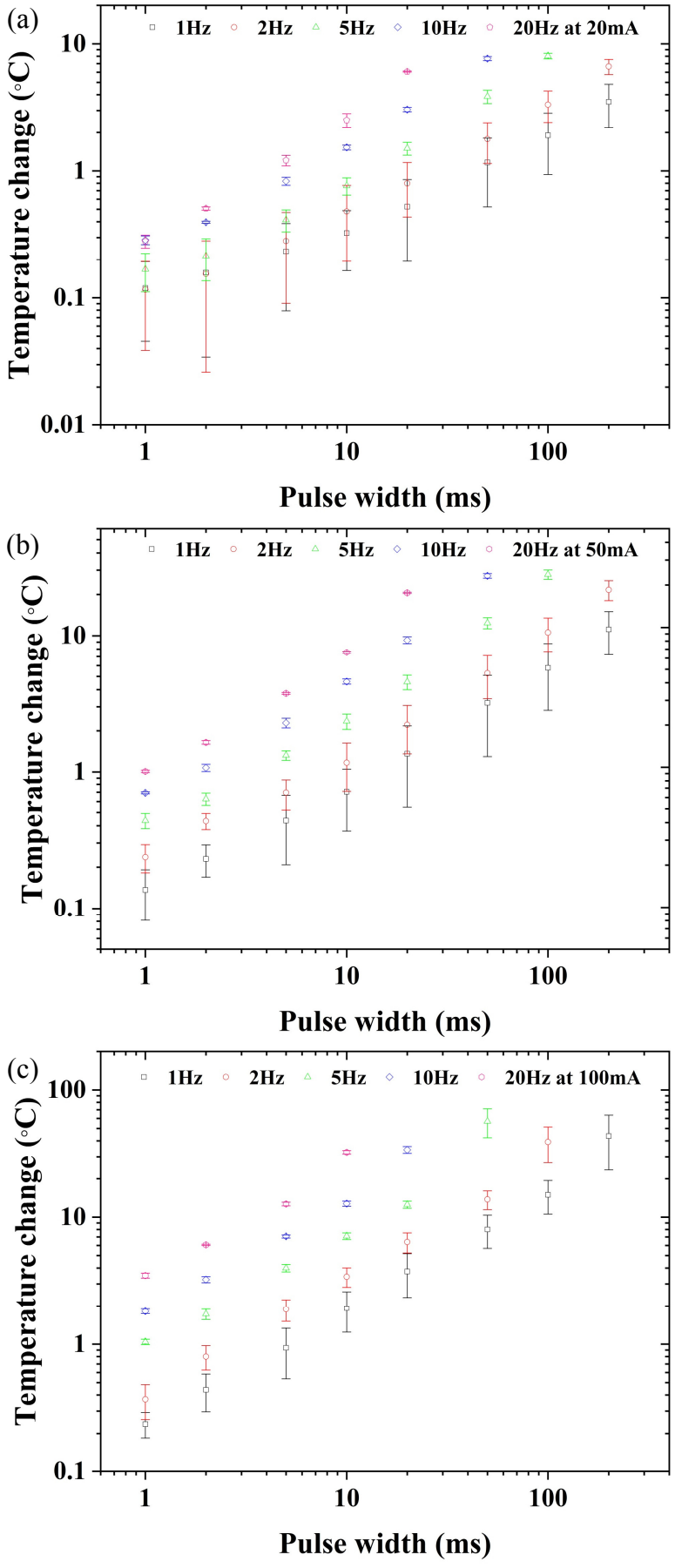

FIGURE 5.25: Thermal measurement performed at the single needle tip. The single optrode is operated by a current source with different frequencies (1, 2, 5, 10 and 20 Hz) and pulse widths (1, 2, 5, 10, 20, 50, 100 and 200 ms). The optrode is operated at (a) 20 mA, (b) 50 mA and (c) 100 mA, respectively. All the measurements are repeated for 5 times.

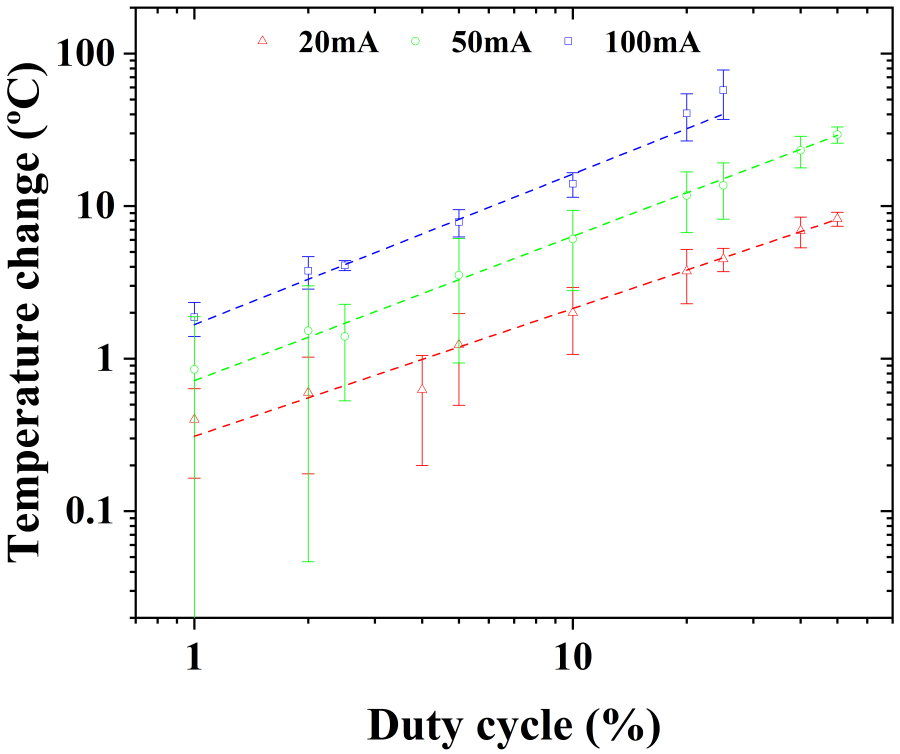

FIGURE 5.26: Thermal measurement performed at the single needle tip with different duty cycles. The single optrode is operated by a current source with different duty cycles (from 1% to 50 %). The amplitude of current source is 20 mA (red triangles), 50 mA (green circles) and 100 mA (blue squares). Linear fits are achieved and indicate linear relationship between the temperature change and the duty cycle.

$$\Delta T = 10^a + D^b \tag{5.3}$$

Therefore, for a given duty cycle and current, the relationship could be written as exponential function with base 10 (formula. 5.3). The slope and the intercept on y-axis of each characteristic is displayed in Table 5.1.

According to the Table 5.1, when the amplitude of current ranges from 20 mA to 100 mA, no significant difference occurs in the slope but a decrease appears in the intercept. A linear relationship between the intercept and the amplitude of current was found and could be expressed as an equation below:

$$Intercept = a_2 + b_2 I \tag{5.4}$$

TABLE 5.1: The slope and the intercept on y-axis of each characteristic.

Current (mA)	Intercept on y-axis	Slope
20	0.22	0.99
50	-0.14	0.95
100	-0.51	0.84

where $a_2 = 0.36$ and $b_2 = -0.01$. As a result, an equation could be used to express the relationship among the temperature increase, the amplitude of current and the duty cycle:

$$\begin{aligned} \Delta T &= 10^{a} + D^{b} \\ &= 10^{(a_2 + b_2 I)} + D^{b_1} \\ &= 10^{(0.36 - 0.01 \times I)} + D^{0.93} \end{aligned} \tag{5.5}$$

Thermal measurement on two lighted optrodes

Thermal performance is also applied to the μLED coupled glass optrode array with two lighted optrodes. As shown in Fig. 5.27(a), the blue element is the targeted optrode where the temperature is recorded. The adjacent element is lit up from element #1 to element #5 to set the distance from 400 μm to 2000 μm. Both optrodes are operated at 50 mA with duty cycles from 1 % to 20 %.

The thermal recording is demonstrated in Fig. 5.27(b). For a given distance, it is similar to the single lighted optrode that the greater temperature change is achieved at the needle tip with higher duty cycle. On the other hand, when both optrodes are operated with same duty cycles, no significant differences of the temperature increase are observed when the distance of two optrodes is changed. No matter two optrodes are closer or further, the temperature change is kept in the same level. Therefore, the heat would not accumulated at the single needle tip when multiple elements are working. Moreover, duty cycle limit was set when simultaneously illuminating multiple LEDs to keep the temperature in brain tissue below 1 °C. For example, if 5 LEDs are activated, the duty cycle will be 15 % at 20 mA. As a result, the heat spreads out along the glass needles and substrate, which makes the device ideal for the brain implantation.

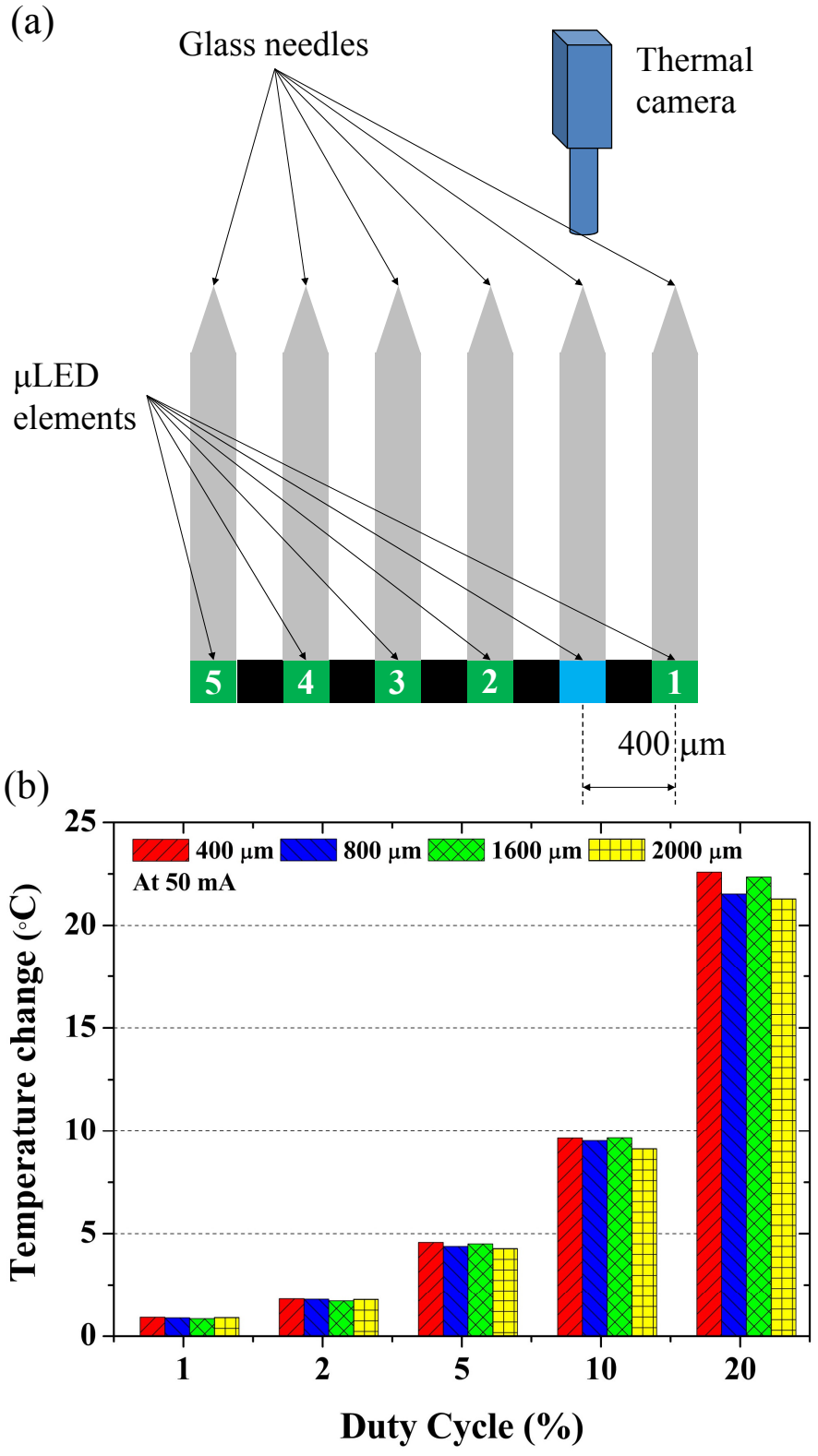

FIGURE 5.27: Thermal performance of the optrode array with two lighted LED pixels. (a) Schematic diagram of measurement setup. The pitch of LEDs is 400 μm. The blue and green indicate the lighted LED elements and the black are gaps between LED elements. Thermal camera is placed on the top of the needle tip to record temperature change. (b) Thermal values of two lighting-up pixels with different distances (400, 800, 1600 and 2000 μm). The LED elements are driven by pulse current at 50 mA with duty cycles from 1 % to 20 %.

5.6 Summary

In this chapter, a μLED coupled glass needle array for optogenetics is introduced. The design and the fabrication process are described in section 5.1 and 5.2 respectively. Then the performance of μLED array is demonstrated in section 5.3. In section 5.4, the integration process is described and in section 5.5, the optical and the thermal performance of μLED coupled glass optrode array are described. According to the requirement of optogenetics, the optical threshold for neuronal stimulation is approximately 1 mW/mm^2. The optrode array developed in this project is able to provide optical irradiance up to 80 mW/mm^2, which satisfies the requirement. The optrode array also enables deep brain stimulation and superficial stimulation. Similar devices have been developed by Kwon et al [188] and Schwaerzle et al [189] which aim to resolve the optical alignment issue by directly integrating LEDs to the penetrating needles. Their use of LEDs with low optical power densities and large standoff distances between the LED and wave guiding structures resulted in low optical power densities (less than 2 mW/mm2) at each illumination site. On the other hand, thermal performance of the array is also characterized. In order to keep the neurons and the neural networks functioning correctly, temperature increase should be maintained below 1 °C. As the optrode array is operated by the current source in pulse mode. According to the thermal characterization, the relationship among the amplitude of current, the duty cycle of current source and the change of temperature at the needle tip could be expressed as an equation of $\Delta T = 10^{0.36-0.01\times I} + D^{0.93}$.

Chapter 6

Conclusion and perspectives

In this thesis, advanced devices for studying neural activity have been presented. A conclusion of the work is given in section 6.1 and some future plans are proposed in section 6.2.

6.1 Conclusions

The work presented in this thesis mainly focused on developing, fabricating and characterizing devices for studying the brain. As mentioned in chapters 1 and 2, studying how neurons interact at the level of circuits will help our understanding of brain functions. Therefore, it is necessary to have a high-density interface between neurons and signal acquisition system. Over the last decade there has been much activity in this area, with neuroscientists now recording from 10s to 100s of neurons simultaneously. The ability to perturb these neural circuits (either electrically or optically), while recording circuit activity, has become an important research area. Optogenetic techniques are a fine example of this, since they have rapidly expanded within a little over 10 years.

For *in vivo* and the *in vitro* experiments, the desire is to have this high-density recording/stimulation in a format that does minimal damage to the neural substrate. These closely packed multi-site devices are required to simplify spike sorting and identify signals from individual neurons. Therefore, semiconductor fabrication

techniques are introduced to produce compact microdevices with multiple channels accessing networks of neurons. The techniques used to develop these devices, are outlined in chapter 3.

Devices fabricated in this project were detailed in chapter 4 and 5 respectively. The high-density penetrating microelectrode array was designed to have 61 recording sites. Each site was placed on the tip of a 200-μm high needle so that all the recording sites can penetrate the surface of tissue and approach to the healthy neurons underneath. During the fabrication process, three main challenges were overcome by developing the fabrication steps. Firstly, the deep reactive ion etch was optimized to achieve deep needle-shape profile with high aspect ratio ($> 12:1$). Typically, the standard etching recipe was able to achieve a deep trench with parallel sidewalls. In this project, the etch recipe therefore was optimized (shown in Table A.3).

Secondly, the spin uniformity of photoresist was affected by the high aspect ratio features on the sample (shown in Fig. 4.9(b)). The photoresist around the deep features was thicker than at other regions of sample. In order to achieve uniform spin coating, a multi-exposure step was developed to completely expose the thicker photoresist so that the recording electrodes and tracks can be clearly defined. Furthermore, the photomask was also updated with wider tracks to avoid over exposure. Thirdly, KOH wet etching was applied to reveal needles from the back side of sample. In order to protect all the metal tracks on the front side, two extra steps were introduced: the sample was firstly coated with protective film to prevent KOH solution from damaging the tracks and then the sample was partially placed into the KOH solution to expose the needles.

This device showed all of the electrical characteristics needed to record from neurons. The impedance of electrode was about 450 kΩ at 1 kHz so that the neural signals can be efficiently extracted. Moreover, 3 pF of inter-channel capacitance was achieved. Therefore, the electrical cross-talk between neighbouring channels is minimized when recording neural signals.

In chapter 5, a μLED array was demonstrated as a light source for optogenetics. The array presented in this thesis can provide 181 individually addressable illumination sites (81 for surface illumination and 100 for deep cortex illumination). When the μLED array was coupled to the Utah glass needle array, comprehensive electrical, optical and thermal testing of the compact device was performed and

demonstrated in chapter 5. An output power of 170 μW at 450-nm wavelength can be emitted from the tip of the needle, when driven at 100 mA. It gives a peak irradiance of 80 mW/mm^2 at the tip of needle. According to the thermal measurement and modelling, a duty cycle limit was put on the operation of the device to ensure the neural tissue does not exceed a 1 °C temperature rise. The equation obtained from the thermal measurement can be used to determine the operation strategies. Furthermore, the thermal constraint was also considered when multiple sites were activated. If the temperature in brain tissue at the tip is to be kept below 1 °C, a 15 % duty cycle limit will be placed when simultaneously illuminating multiple LEDs such as 5 elements at 20 mA.

As mentioned in chapter 5, the main difficulty in the fabrication process is to avoid weak points at the passivation layer (SiO_2). These weak points are the main reason for electrical shorts between the p- and n-type contacts of the LED element. In order to overcome this challenge, an O_2 plasma ashing step was introduced to further clean the sample and ensure no photoresist residual left on the surface, especially on the trenches between adjacent n-type GaN mesa (shown in Fig. 5.8). Therefore, a fabrication yield of over 95 % was achieved in this project.

6.2 Future works

In order to further improve the performance of the penetrating microelectrode array and the μLED coupled glass optrode array, some optimizations in the fabrication process are needed and detailed below.

6.2.1 Optimization of high-density penetrating microelectrode array

According to the device characterization, the fabrication process of this penetrating microelectrode array can be further developed to improve the performance. Firstly, the front side of sample should be well-protected during KOH wet etching since 13 tracks were damaged by this process. According to the fabrication result, ProTEK B3 film was not enough to resist the KOH etch on the front side. Therefore, an oxide-nitride-oxide (SiO_2-SiN_x-SiO_2) stack will be deposited onto

the sample before coating ProTEK B3 film. The oxide layer has a good adhesion and also a good resistance to KOH solution. The nitride layer is able to further improve the alkaline resistance. As a consequence, all recording channels will be well-protected so that all 61 electrodes will fully function during *in vitro* experiment.

Secondly, the needle tips were found to be rough after KOH and BOE wet etch (shown in Fig. 4.18). Therefore, the needles will be fragile and may be broken during insertion. As shown in Fig. 6.1, some tips of needles faded away during the wet etch and the remaining tips started to be damaged. In order to fabricate needles with proper shapes, some additives such as isopropyl alcohol (IPA) can be added to the KOH aqueous solution [190] to achieve good control on wet etch process. Therefore, the needles will be exposed more uniformly with a regular needle-shape.

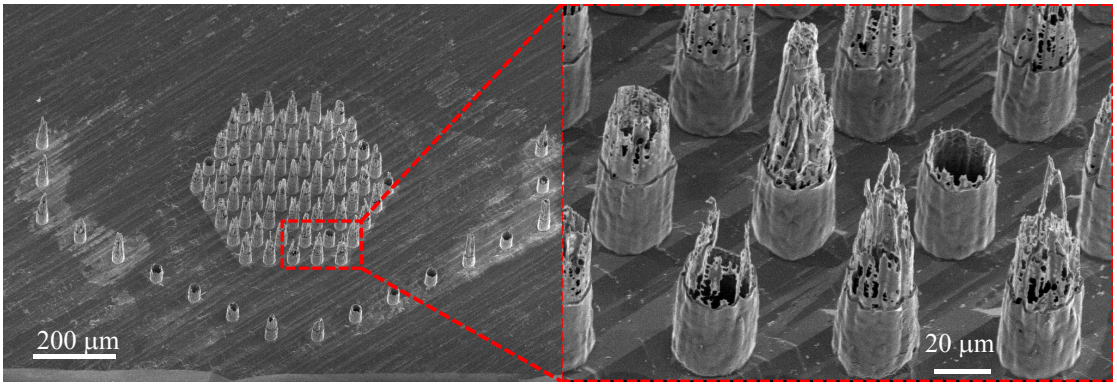

FIGURE 6.1: Penetrating microelectrode array with broken needles. Scale bar: 200 μm. After KOH and BOE wet etch, some tips of needles were found to have been damaged (highlighted by red dash box). Scale bar: 20 μm.

6.2.2 Optimization of μLED coupled glass optrode array

As mentioned in chapter 5, the μLED array is designed to be matrix addressable to achieve individual and multi-site illumination, while minimizing the number of interconnects. Therefore, any short circuits in the array will lead to unexpected pattern illumination. In order to further avoid short circuits, two possible strategies will be applied in the future fabrication process. One of the simplest way is to increase the thickness of the passivation layer (SiO_2). In this work, the thickness of the passivation layer is 300 nm. In the future, the thickness will be increased to 1 μm. Moreover, in order to avoid pinholes during the PECVD process, the

deposition will be separated into two steps and each step will form 500-nm thick SiO_2 layer. However, the thicker the SiO_2 layer, the more stressed the thin film becomes. The sample may have more risk to be cracked and therefore, another strategy is developed to create small steps on the sidewalls of the n-type GaN mesa (shown in Fig. 6.2). During the current fabrication process, the height of n-type GaN mesa was about 5 μm which is big step for thin SiO_2 layer (300 nm) to fully cover. Therefore, the SiO_2 layer will be thinner on the sidewall than on the top and bottom of the mesa. The thinner SiO_2 is considered as a weak part on the passivation layer and may cause short circuits. This can be mitigated by creating a stepped sidewall profile, with each step measuring 2, 2 and 1 μm in height. The sidewall profile can be obtained by using Veeco Dektak3 Surface Profileometer. This will allow a relatively uniform coating to be achieved over the smaller steps and minimise the chance of poor isolation between the n- and p-type contacts. This is shown in Fig. 6.2. As a consequence, the coverage of thin SiO_2 layer will be improved to achieve uniform thickness of deposition and the short circuits therefore will be further avoided.

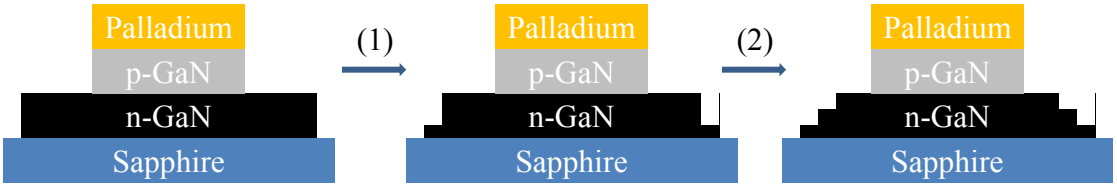

FIGURE 6.2: Schematic diagram of creating small steps on the sidewalls of n-type GaN mesa. After p-type GaN etch, the n-type GaN layer will be etched twice. This two-step etch will create stepped sidewall on n-type GaN layer and the step will be 2, 2 and 1 μm in height.

Apart from the device fabrication, the coupling of the μLED array and the Utah glass array can be further optimized. In the current design, the optical cross-talk between the glass needles was significantly reduced using a metallic layer (Ti/Au) with small apertures (80×80 μm^2 and 40×40 μm^2) to block stray light. However, according to the modelling, the pinhole structure is not ideal to block stray light. It cannot block all stray light and still allow for enough light emitted from the needle tip. An alternative option is to replace the glass backplane of the needle array with a silicon backplane with ethced holes that acts as optical interposers to allow light to couple into the needles and the interstitial sites. The completed optrode array with silicon interposer is shown in Fig. 6.3 and the performance characterization is underway.

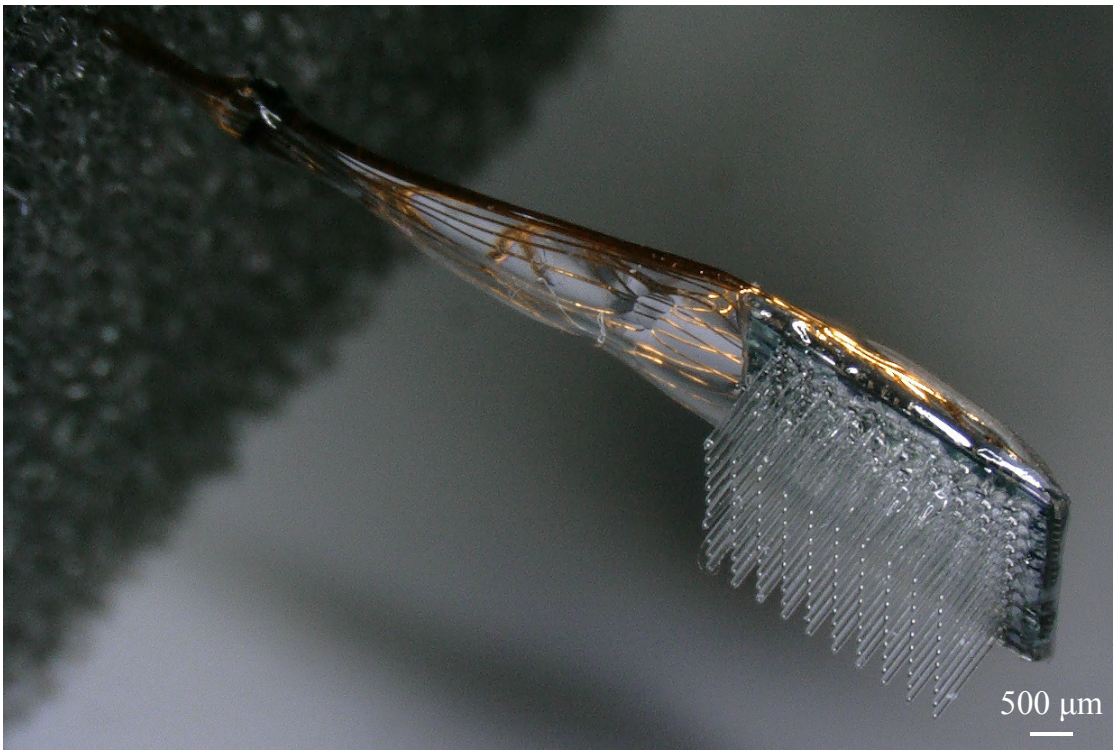

FIGURE 6.3: Completed optrode array with silicon interposer. Glass needles are directly integrated onto the silicon substrate with optical interposer. The μLED array is placed at the back side of the silicon interposer. The whole device is wire bonded to the external electronic system via insulated gold wires and is encapsulated with polymer. Scale bar: 500 μm.

6.2.3 New design of novel integrated optrode array

The optrode array demonstrated in this project is only used to activate neurons optically. The generated neural signals can propagate to the rest regions of the brain through the neural network. In order to investigate the connections between neighbouring regions, another electrophysiological recording device is needed such as high-density microneedle array. As a result, secondary invasion to the brain will be introduced by the implantation of microneedle array. To minimize the tissue damage, it is expected to integrate the electrodes with the optrode array so that it can function as a stimulus and a recording site simultaneously (Fig. 6.4). Moreover, mapping the neural network in the deep brain region becomes possible due to the large coverage (5 mm $\times$ 5 mm) of the optrode array.

This design will present some device fabrication challenges: firstly, the electrodes should be positioned on the needle tip with metal tracks wired out to the outer electronic system. The fabrication will be challenge but the recent study provides a potential strategy to achieve the goal [191]. However, the light will be blocked

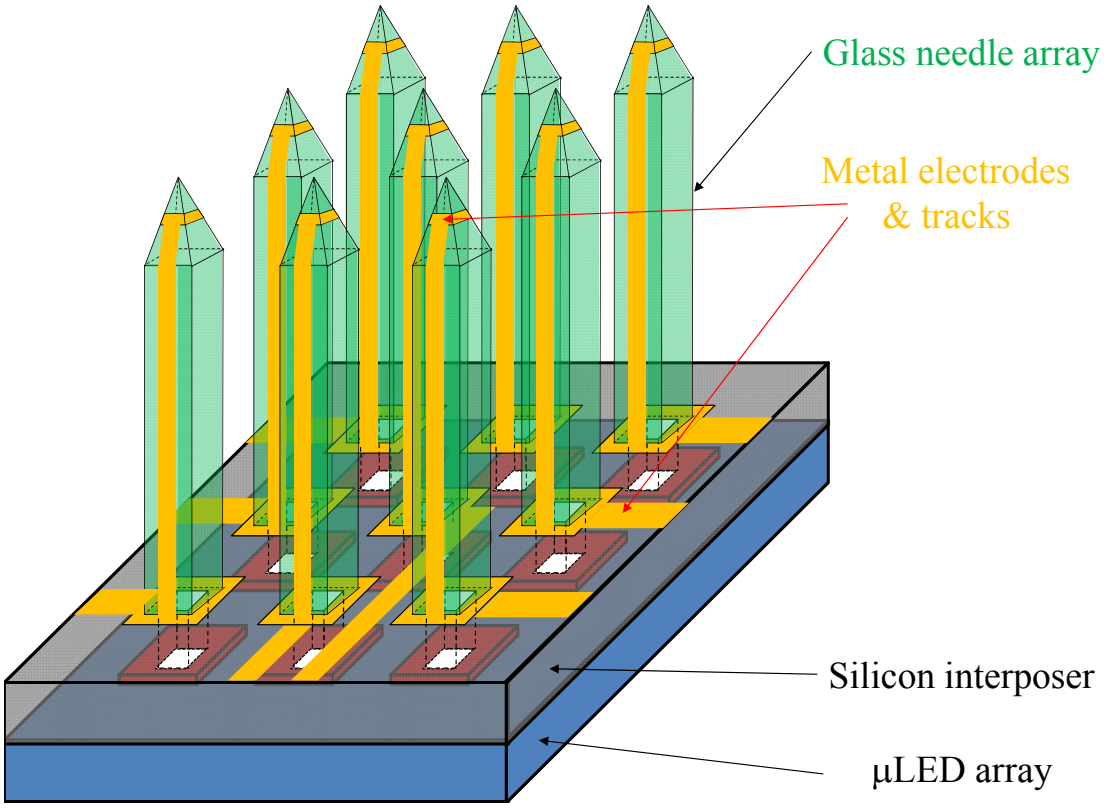

FIGURE 6.4: Schematic of integrated optrode array. Metal electrodes are placed on the top of the needles and the tracks are along the needles.

by the electrodes and wires if they are made of metal such as gold, tungsten or platinum; secondly, there will be 181 recording channels connect between outer electronic system and electrodes. As a result, transparent conductors should be considered that have the capability to be patterned at a density that would allow multiple tracks between each needle in the array. Indium Tin Oxide is a good candidate for this and has been used to individually address microelectrodes for neural recordings in the past [139, 188] and is optically transparent. With these optimizations, the devices presented in this thesis promise to realise high-density recording/stimulation from intact neural circuits both *in vivo* and *in vitro*.

Appendix A

Dry etching recipes

A.1 Aluminium etch recipe

In this project, the aluminium etch was achieved by using ICP system and the recipe is shown in table A.1. The etch rate is about 120 nm/min.

Table A.1: Aluminium etch recipe.

Cl_2 (sccm)	BCl_3 (sccm)	Platen power (W)	Coil power (W)	Pressure (Torr)
4	16	50	*NA*	0.02

Table A.2: Si etch recipe of standard Bosch process.

Parameter name	Unit	Dep	Etch
Process time	sec	7	7
C_4F_8	sccm	135	*NA*
SF_6	sccm	*NA*	135
ICP Forward Power	W	600	800

A.2 Silicon etch recipe

The etch recipe of a standard Bosch process is shown in table A.2. In this project, the Bosch process was optimized for the purpose of needle-shape etching profile and the optimized recipe is shown in table A.3.

TABLE A.3: Characterized Bosch process recipe to achieve long, tapered needle profile.

Parameter name	**Unit**	**Dep**	**Etch A**	**Etch B**
Process time	sec	2.5	1.5	3.5
C_4F_8	sccm	150	*NA*	*NA*
SF_6	sccm	*NA*	150	300
Ar	sccm	30	30	30
ICP Forward Power	W	2000	3000	3000
Pressure	mT	25	40	75

A.3 Silicon dioxide etch recipe

TABLE A.4: Silicon dioxide etch recipe of high etch rate.

Ar (sccm)	**CHF_3 (sccm)**	**RIE power (W)**	**Pressure (Torr)**
15	5	200	0.03

TABLE A.5: Silicon dioxide etch recipe of low etch rate.

Ar (sccm)	**CHF_3 (sccm)**	**RIE power (W)**	**Pressure (Torr)**
15	5	120	0.03

There are two etch recipes of silicon dioxide in this project. One provides a high etch rate (40 nm/min) and the other one provides a low etch rate (28 nm/min). The recipe of high etch rate is detailed in table A.4 and the one of low etch rate is shown in table A.5.

A.4 Titanium/tungsten bilayer etch recipe

The titanium/tungsten bilayer is etched in RIE tool and the recipe is demonstrated in table A.6.

Table A.6: Titanium/tungsten bilayer etch recipe.

Material	**Ar (sccm)**	**SF_6 (sccm)**	**RIE power (W)**	**Pressure (Torr)**
Ti	40	10	200	0.045
W	*NA*	60	120	0.05

A.5 Parylene-C etch recipe

Parylene-C film is etched in RIE tool and the recipe is shown in table A.7. The etch rate is about 380 nm/min.

Table A.7: Parylene-C etch recipe.

O_2 (sccm)	**RIE power (W)**	**Pressure (Torr)**
50	200	0.08

A.6 Palladium etch recipe

The palladium is etched in RIE tool and the etch recipe is shown in table A.8. The etch rate is about 10 nm/min.

Table A.8: Palladium etch recipe.

Ar (sccm)	**RIE power (W)**	**Pressure (Torr)**
20	300	0.035

A.7 Gallium nitride etch recipe

The Gallium nitride is etched in ICP system and the etch recipe is shown in table A.9. The etch rate is about 280 nm/min.

Table A.9: Gallium nitride etch recipe.

Ar (**sccm**)	**Cl_2** (**sccm**)	**Platen power** (**W**)	**Coil power** (**W**)	**Pressure** (**Torr**)
10	30	200	400	0.02

Bibliography

[1] Eric R Kandel, James H Schwartz, Thomas M Jessell, Department of Biochemistry, Molecular Biophysics Thomas Jessell, Steven Siegelbaum, and AJ Hudspeth. *Principles of neural science*, volume 4. McGraw-hill New York, 2000.

[2] Harvey Lodish, Arnold Berk, S Lawrence Zipursky, Paul Matsudaira, David Baltimore, James Darnell, et al. *Molecular cell biology*, volume 3. WH Freeman New York, 1995.

[3] D.T. Sawyer, A. Sobkowiak, and J.L. Roberts. *Electrochemistry for Chemists*. Wiley, 1995. ISBN 9780471594680. URL `https://books.google.co.uk/books?id=a6R1QgAACAAJ`.

[4] The Human Brain Project. . URL `https://www.humanbrainproject.eu/`.

[5] Human Brain Project, Framework Partnership Agreement. . URL `https://sos-ch-dk-2.exo.io/public-website-production/filer_public/7b/1c/7b1c5b15-1a7f-4912-815e-c9a3ff5820d5/hbp_fpa_amendment_1.pdf`.

[6] Black Obama. BRAIN Initiative | The White House. URL `http://www.whitehouse.gov/share/brain-initiative`.

[7] BRAIN 2025: A scientific vision. Brain Research through Advancing Innovative Neurotechnologies (BRAIN) Working Group Report to the Advisory Committee to the Director, NIH.

[8] David A Drachman. Do we have brain to spare?, 2005.

[9] Edgar D Adrian and Detlev W Bronk. The discharge of impulses in motor nerve fibres. *The Journal of physiology*, 67(2):9–151, 1929.

[10] D Williams and G Parsons-Smith. The spontaneous electrical activity of the human thalamus. *Brain*, 72(3):450–482, 1949.

[11] David H Hubel and Torsten N Wiesel. Receptive fields of single neurones in the cat's striate cortex. *The Journal of physiology*, 148(3):574–591, 1959.

[12] Elwin Marg and John E Adams. Indwelling multiple micro-electrodes in the brain. *Electroencephalography and clinical neurophysiology*, 23(3):277–280, 1967.

[13] Eric Halgren, Thomas L Babb, and Paul H Crandall. Activity of human hippocampal formation and amygdala neurons during memory testing. *Electroencephalography and Clinical Neurophysiology*, 45(5):585–601, 1978.

[14] Apostolos P Georgopoulos, Andrew B Schwartz, and Ronald E Kettner. Neuronal population coding of movement direction. *Science*, 233(4771): 1416–1419, 1986.

[15] George A Ojemann, Otto Creutzfeldt, Ettore Lettich, and Michael M Haglund. Neuronal activity in human lateral temporal cortex related to short-term verbal memory, naming and reading. *Brain*, 111(6):1383–1403, 1988.

[16] Alexa Riehle, Sonja Grün, Markus Diesmann, and A Aertsen. Spike synchronization and rate modulation differentially involved in motor cortical function. *Science*, 278(5345):1950–1953, 1997.

[17] P R Kennedy and R AE Bakay. Restoration of neural output from a paralyzed patient by a direct brain connection. *Neuroreport*, 9(8):1707–1711, 1998.

[18] Garrett B Stanley, Fei F Li, and Yang Dan. Reconstruction of natural scenes from ensemble responses in the lateral geniculate nucleus. *Journal of Neuroscience*, 19(18):8036–8042, 1999.

[19] Miguel AL Nicolelis, Dragan Dimitrov, Jose M Carmena, Roy Crist, Gary Lehew, Jerald D Kralik, and Steven P Wise. Chronic, multisite, multielectrode recordings in macaque monkeys. *Proceedings of the National Academy of Sciences*, 100(19):11041–11046, 2003.

[20] Leigh R Hochberg, Mijail D Serruya, Gerhard M Friehs, Jon A Mukand, Maryam Saleh, Abraham H Caplan, Almut Branner, David Chen, Richard D Penn, and John P Donoghue. Neuronal ensemble control of prosthetic devices by a human with tetraplegia. *Nature*, 442(7099):164, 2006.

[21] Margaret B Rheinberger and Herbert H Jasper. Electrical activity of the cerebral cortex in the unanesthetized cat. *American Journal of Physiology-Legacy Content*, 119(1):186–196, 1937.

[22] Harry Grundfest, Robert W Sengstaken, Walter H Oettinger, and RW Gurry. Stainless steel micro-needle electrodes made by electrolytic pointing. *Review of Scientific Instruments*, 21(4):360–361, 1950.

[23] Andrus Jules. Fabrication of semiconductor devices, March 3 1964. US Patent 3,122,817.

[24] Kensall D Wise, James B Angell, and Arnold Starr. An integrated-circuit approach to extracellular microelectrodes. *IEEE transactions on biomedical engineering*, (3):238–247, 1970.

[25] Michael Salcman and M Bak. Thumbtack microelectrode and method of making same, July 30 1974. US Patent 3,826,244.

[26] Gerald E Loeb, MJ Bak, M Salcman, and EM Schmidt. Parylene as a chronically stable, reproducible microelectrode insulator. *IEEE Transactions on Biomedical Engineering*, (2):121–128, 1977.

[27] J Krüger and M_ Bach. Simultaneous recording with 30 microelectrodes in monkey visual cortex. *Experimental brain research*, 41(2):191–194, 1981.

[28] Khalil Najafi, KD Wise, and Tohru Mochizuki. A high-yield ic-compatible multichannel recording array. *IEEE Transactions on Electron Devices*, 32 (7):1206–1211, 1985.

[29] Patrick K Campbell, Kelly E Jones, Robert J Huber, Kenneth W Horch, and Richard A Normann. A silicon-based, three-dimensional neural interface: manufacturing processes for an intracortical electrode array. *IEEE Transactions on Biomedical Engineering*, 38(8):758–768, 1991.

[30] Franz Laermer and Andrea Schilp. Method of anisotropically etching silicon, March 26 1996. US Patent 5,501,893.

[31] Karen Cheung, Gun Lee, Kaj Djupsund, Yang Dan, and Luke P Lee. A new neural probe using soi wafers with topological interlocking mechanisms. In *Microtechnologies in Medicine and Biology, 1st Annual International, Conference On. 2000*, pages 507–511. IEEE, 2000.

[32] Patrick J Rousche, David S Pellinen, David P Pivin, Justin C Williams, Rio J Vetter, and Daryl R Kipke. Flexible polyimide-based intracortical electrode arrays with bioactive capability. *IEEE Transactions on biomedical engineering*, 48(3):361–371, 2001.

[33] Xinyan Cui and David C Martin. Electrochemical deposition and characterization of poly (3, 4-ethylenedioxythiophene) on neural microelectrode arrays. *Sensors and Actuators B: Chemical*, 89(1-2):92–102, 2003.

[34] Y Zhong, GC McConnell, JD Ross, SP DeWeerth, and RV Bellamkonda. A novel dexamethasone-releasing, anti-inflammatory coating for neural implants. In *Neural Engineering, 2005. Conference Proceedings. 2nd International IEEE EMBS Conference on*, pages 522–525. IEEE, 2005.

[35] Jeffrey R. Capadona, Kadhiravan Shanmuganathan, Dustin J. Tyler, Stuart J. Rowan, and Christoph Weder. Stimuli-responsive polymer nanocomposites inspired by the sea cucumber dermis. 319(5868):1370–1374, 2008. doi: 10.1126/science.1153307.

[36] John L Skousen, Michael J Bridge, and Patrick A Tresco. A strategy to passively reduce neuroinflammation surrounding devices implanted chronically in brain tissue by manipulating device surface permeability. *Biomaterials*, 36:33–43, 2015.

[37] Katarzyna M Szostak, Laszlo Grand, and Timothy G Constandinou. Neural interfaces for intracortical recording: Requirements, fabrication methods, and characteristics. *Frontiers in neuroscience*, 11:665, 2017.

[38] Birdsey Renshaw, Alexander Forbes, and BR Morison. Activity of isocortex and hippocampus: electrical studies with micro-electrodes. *Journal of neurophysiology*, 3(1):74–105, 1940.

[39] David H Hubel et al. Tungsten microelectrode for recording from single units. *Science*, 125(3247):549–550, 1957.

[40] Nature Publishing Group. Editorial: Method of the Year 2010. *Nature Meth*, 8(1):549–550, 2011.

[41] Deborah E Gunning, John M Beggs, Wladeslaw Dabrowski, Pawel Hottowy, Christopher J Kenney, Alexander Sher, Alan M Litke, and Keith Mathieson. Dense arrays of micro-needles for recording and electrical stimulation of neural activity in acute brain slices. *Journal of neural engineering*, 10(1):016007, 2012.

[42] Tanya Vanessa F Abaya, Mohit Diwekar, Steve Blair, Prashant Tathireddy, Loren Rieth, GA Clark, and Florian Solzbacher. Characterization of a 3d optrode array for infrared neural stimulation. *Biomedical optics express*, 3 (9):2200–2219, 2012.

[43] Tanya Vanessa F Abaya, Mohit Diwekar, Steve Blair, Prashant Tathireddy, Loren Rieth, and Florian Solzbacher. Deep-tissue light delivery via optrode arrays. *Journal of Biomedical Optics*, 19(1):015006, 2014.

[44] Kensall D Wise, Amir M Sodagar, Ying Yao, Mayurachat Ning Gulari, Gayatri E Perlin, and Khalil Najafi. Microelectrodes, microelectronics, and implantable neural microsystems. *Proceedings of the IEEE*, 96(7):1184–1202, 2008.

[45] Rajmohan Bhandari, Sandeep Negi, and Florian Solzbacher. Wafer-scale fabrication of penetrating neural microelectrode arrays. *Biomedical microdevices*, 12(5):797–807, 2010.

[46] Miguel Cabello, Carmen Aracil, Francisco Perdigones, Marta Mozo, Berta de la Cerda, and José M Quero. Gold microelectrodes array embedded in pdms for electrical stimulation and signal detection. *Sensors and Actuators B: Chemical*, 257:954–962, 2018.

[47] Almut Branner, Richard B Stein, Eduardo Fernandez, Yoichiro Aoyagi, and Richard A Normann. Long-term stimulation and recording with a penetrating microelectrode array in cat sciatic nerve. *IEEE transactions on biomedical engineering*, 51(1):146–157, 2004.

[48] Jean Delbeke, Luis Hoffman, Katrien Mols, Dries Braeken, and Dimiter Prodanov. And then there was light: perspectives of optogenetics for deep brain stimulation and neuromodulation. *Frontiers in neuroscience*, 11:663, 2017.

[49] John A Neff. Major initiatives for optical computing. *Optical Engineering*, 26(1):260102, 1987.

[50] Ruth Palombo Weiss. Brain based learning. *Training & Development*, 54 (7):21–21, 2000.

[51] Michael A Paradiso, Mark F Bear, and Barry W Connors. Neuroscience: exploring the brain. *Hagerstwon, MD: Lippincott Williams & Wilkins*, 718, 2007.

[52] Julian Seifter, David Sloane, and Austin Ratner. *Concepts in medical physiology*. Lippincott Williams & Wilkins, 2005.

[53] The Nobel Prize in Physiology or Medicine 1981.

[54] M Salcman and M. J. Bak. Design, fabrication, and in vivo behavior of chronic recording intracortical microelectrodes. *Biomedical Engineering IEEE Transactions on*, BME-20(4):253–260, 1973.

[55] Michael Salcman and Martin J. Bak. A new chronic recording intracortical microelectrode. *Medical & Biological Engineering*, 14(1):42–50, 1976.

[56] J Pine. Recording action potentials from cultured neurons with extracellular microcircuit electrodes. *Journal of Neuroscience Methods*, 2(1):19–31, 1980.

[57] Fabrice O. Morin, Yuzuru Takamura, and Eiichi Tamiya. Investigating neuronal activity with planar microelectrode arrays: achievements and new perspectives. *Journal of Bioscience & Bioengineering*, 100(2):131–143, 2005.

[58] A. M. Litke, N. Bezayiff, E. J. Chichilnisky, and W. Cunningham. What does the eye tell the brain?: Development of a system for the large scale recording of retinal output activity. In *Nuclear Science Symposium Conference Record*, pages 951–955 Vol.2, 2004.

[59] D. E. Gunning, E. J. Chichilnisky, A. M. Litke, V. OShea, K. M. Smith, and K. Mathieson. Performance of ultra-high-density microelectrode arrays. *Nuclear Instruments & Methods in Physics Research A*, 576(1):215–219, 2007.

[60] U Frey, C. D. Sanchez-Bustamante, T Ugniwenko, F Heer, J Sedivy, S Hafizovic, B Roscic, M Fussenegger, A Blau, and U Egert. Cell recordings with a cmos high-density microelectrode array. In *Engineering in Medicine and*

Biology Society, 2007. Embs 2007. International Conference of the IEEE, pages 167–170, 2007.

[61] K. D Wise, J. B Angell, and Arnold Starr. An integrated-circuit approach to extracellular microelectrodes. *Biomedical Engineering IEEE Transactions on*, BME-17(3):238–247, 1970.

[62] K Najafi, K. D Wise, and T Mochizuki. A high-yield ic-compatible multichannel recording array. *Electron Devices IEEE Transactions on*, 32(7): 1206–1211, 1985.

[63] Peter Norlin, Maria Kindlundh, Aliette Mouroux, Ken Yoshida, and Ulrich G Hofmann. A 32-site neural recording probe fabricated by drie of soi substrates. *Journal of Micromechanics & Microengineering*, 12(12):414–419, 2002.

[64] Jrg Scholvin, Justin P. Kinney, Jacob G. Bernstein, Caroline Moorekochlacs, Nancy Kopell, Clifton G. Fonstad, and Edward S. Boyden. Close-packed silicon microelectrodes for scalable spatially oversampled neural recording. *IEEE transactions on bio-medical engineering*, 63(1):120, 2016.

[65] R. A. Normann, P. K. Campbell, and K. E. Jones. A silicon based electrode array for intracortical stimulation: structural and electrical properties. In *Century., Proceedings of the International Conference of the IEEE Engineering in*, pages 939–940 vol.3, 1989.

[66] P K Campbell, K E Jones, R J Huber, K W Horch, and R A Normann. A silicon-based, three-dimensional neural interface: manufacturing processes for an intracortical electrode array. *Biomedical Engineering, IEEE Transactions on*, 38(8):758–768, 1991.

[67] Rajmohan Bhandari, Sandeep Negi, Loren Rieth, Michael Toepper, Sohee Kim, Matthias Klein, Hermann Oppermann, Richard A. Normann, and Florian Solzbacher. System integration of the utah electrode array using a biocompatible flip chip under bump metallization scheme. In *Active and Passive Smart Structures and Integrated Systems*, pages 65251K–65251K–8, 2007.

[68] H. A. Wark, R Sharma, K. S. Mathews, E Fernandez, J Yoo, B Christensen, P Tresco, L Rieth, F Solzbacher, and R. A. Normann. A new high-density

(25 electrodes/mm) penetrating microelectrode array for recording and stimulating sub-millimeter neuroanatomical structures. *Journal of Neural Engineering*, 10(4):045003, 2013.

[69] Bryan Kolb and Ian Q Whishaw. *An introduction to brain and behavior.* Worth Publishers, 2001.

[70] Francis HC Crick. Thinking about the brain. *Scientific American*, 241(3): 219–233, 1979.

[71] Ryan T LaLumiere. A new technique for controlling the brain: optogenetics and its potential for use in research and the clinic. *Brain stimulation*, 4(1): 1–6, 2011.

[72] David C Plachetzki, Caitlin R Fong, and Todd H Oakley. The evolution of phototransduction from an ancestral cyclic nucleotide gated pathway. *Proceedings of the Royal Society of London B: Biological Sciences*, 277(1690): 1963–1969, 2010.

[73] Russell D Fernald. Casting a genetic light on the evolution of eyes. *Science*, 313(5795):1914–1918, 2006.

[74] Ofer Yizhar, Lief E. Fenno, Thomas J. Davidson, Murtaza Mogri, and Karl Deisseroth. Optogenetics in neural systems. *Neuron*, 71(1):9–34, 2011.

[75] Dieter Oesterhelt and Walther Stoeckenius. Rhodopsin-like protein from the purple membrane of halobacterium halobium. *Nature new biology*, 233(39): 149, 1971.

[76] Dieter Oesterhelt and Walther Stoeckenius. Functions of a new photoreceptor membrane. *Proceedings of the National Academy of Sciences*, 70(10): 2853–2857, 1973.

[77] Efraim Racker and Walther Stoeckenius. Reconstitution of purple membrane vesicles catalyzing light-driven proton uptake and adenosine triphosphate formation. *Journal of Biological Chemistry*, 249(2):662–663, 1974.

[78] Ho Michel and D Oesterhelt. Light-induced changes of the ph gradient and the membrane potential in h. halobium. *FEBS letters*, 65(2):175–178, 1976.

[79] Brian Y Chow, Xue Han, Allison S Dobry, Xiaofeng Qian, Amy S Chuong, Mingjie Li, Michael A Henninger, Gabriel M Belfort, Yingxi Lin, Patrick E

Monahan, et al. High-performance genetically targetable optical neural silencing by light-driven proton pumps. *Nature*, 463(7277):98, 2010.

[80] Akemi Matsuno-Yagi and Yasuo Mukohata. Two possible roles of bacteriorhodopsin; a comparative study of strains of halobacterium halobium differing in pigmentation. *Biochemical and biophysical research communications*, 78(1):237–243, 1977.

[81] Viviana Gradinaru, Kimberly R Thompson, and Karl Deisseroth. enphr: a natronomonas halorhodopsin enhanced for optogenetic applications. *Brain cell biology*, 36(1-4):129–139, 2008.

[82] Oleg A Sineshchekov, Kwang-Hwan Jung, and John L Spudich. Two rhodopsins mediate phototaxis to low-and high-intensity light in chlamydomonas reinhardtii. *Proceedings of the National Academy of Sciences*, 99 (13):8689–8694, 2002.

[83] Alexander I Erofeev, Maxim V Matveev, Stanislav G Terekhin, Olga A Zakharova, Polina V Plotnikova, and Olga L Vlasova. The new method for studying neuronal activity: Optogenetics. *St. Petersburg Polytechnical University Journal: Physics and Mathematics*, 1(3):256–263, 2015.

[84] Xue Han and Edward S Boyden. Multiple-color optical activation, silencing, and desynchronization of neural activity, with single-spike temporal resolution. *PloS one*, 2(3):e299, 2007.

[85] A Duschl, Janos K Lanyi, and László Zimányi. Properties and photochemistry of a halorhodopsin from the haloalkalophile, natronobacterium pharaonis. *Journal of Biological Chemistry*, 265(3):1261–1267, 1990.

[86] Edward S Boyden, Feng Zhang, Ernst Bamberg, Georg Nagel, and Karl Deisseroth. Millisecond-timescale, genetically targeted optical control of neural activity. *Nature neuroscience*, 8(9):1263, 2005.

[87] Nathan C Klapoetke, Yasunobu Murata, Sung Soo Kim, Stefan R Pulver, Amanda Birdsey-Benson, Yong Ku Cho, Tania K Morimoto, Amy S Chuong, Eric J Carpenter, Zhijian Tian, et al. Independent optical excitation of distinct neural populations. *Nature methods*, 11(3):338, 2014.

[88] Viviana Gradinaru, Feng Zhang, Charu Ramakrishnan, Joanna Mattis, Rohit Prakash, Ilka Diester, Inbal Goshen, Kimberly R Thompson, and Karl

Deisseroth. Molecular and cellular approaches for diversifying and extending optogenetics. *Cell*, 141(1):154–165, 2010.

[89] Elena G Govorunova, Oleg A Sineshchekov, Roger Janz, Xiaoqin Liu, and John L Spudich. Natural light-gated anion channels: A family of microbial rhodopsins for advanced optogenetics. *Science*, page aaa7484, 2015.

[90] Adam M Packer, Botond Roska, and Michael Häusser. Targeting neurons and photons for optogenetics. *Nature neuroscience*, 16(7):805, 2013.

[91] Feng Zhang, Viviana Gradinaru, Antoine R Adamantidis, Remy Durand, Raag D Airan, Luis De Lecea, and Karl Deisseroth. Optogenetic interrogation of neural circuits: technology for probing mammalian brain structures. *Nature protocols*, 5(3):439, 2010.

[92] Caroline E Bass, Valentina P Grinevich, Zachary B Vance, Ryan P Sullivan, Keith D Bonin, and Evgeny A Budygin. Optogenetic control of striatal dopamine release in rats. *Journal of neurochemistry*, 114(5):1344–1352, 2010.

[93] Ilana B Witten, Shih-Chun Lin, Matthew Brodsky, Rohit Prakash, Ilka Diester, Polina Anikeeva, Viviana Gradinaru, Charu Ramakrishnan, and Karl Deisseroth. Cholinergic interneurons control local circuit activity and cocaine conditioning. *science*, 330(6011):1677–1681, 2010.

[94] Michael T Stefanik, Khaled Moussawi, Yonatan M Kupchik, Kyle C Smith, Rachel L Miller, Mary L Huff, Karl Deisseroth, Peter W Kalivas, and Ryan T LaLumiere. Optogenetic inhibition of cocaine seeking in rats. *Addiction biology*, 18(1):50–53, 2013.

[95] X. Han, X. Qian, J. G. Bernstein, H. H. Zhou, G. T. Franzesi, P Stern, R. T. Bronson, A. M. Graybiel, R Desimone, and E. S. Boyden. Millisecond-timescale optical control of neural dynamics in the nonhuman primate brain. *Neuron*, 62(2):191–198, 2009.

[96] Ken Sugino, Chris M Hempel, Mark N Miller, Alexis M Hattox, Peter Shapiro, Caizi Wu, Z Josh Huang, and Sacha B Nelson. Molecular taxonomy of major neuronal classes in the adult mouse forebrain. *Nature Neuroscience*, 9(1):99–107, 2006.

[97] G Fishell and N Heintz. The neuron identity problem: form meets function. *Neuron*, 80(3):602–12, 2013.

[98] Deniz Atasoy, Yexica Aponte, Helen Hong Su, and Scott M Sternson. A flex switch targets channelrhodopsin-2 to multiple cell types for imaging and long-range circuit mapping. *Journal of Neuroscience*, 28(28):7025–7030, 2008.

[99] Sandra J. Kuhlman and Z. Josh Huang. High-resolution labeling and functional manipulation of specific neuron types in mouse brain by cre-activated viral gene expression. *Plos One*, 3(4):e2005, 2008.

[100] Hsing-Chen Tsai, Feng Zhang, Antoine Adamantidis, Garret D Stuber, Antonello Bonci, Luis De Lecea, and Karl Deisseroth. Phasic firing in dopaminergic neurons is sufficient for behavioral conditioning. *Science*, 324(5930): 1080–1084, 2009.

[101] Jacob G Bernstein and Edward S Boyden. Optogenetic tools for analyzing the neural circuits of behavior. *Trends in cognitive sciences*, 15(12):592–600, 2011.

[102] Stephanie Chan, Jacob Bernstein, and Edward Boyden. Scalable fluidic injector arrays for viral targeting of intact 3-d brain circuits. *Journal of Visualized Experiments Jove*, (35):e1489–e1489, 2010.

[103] Linda Madisen, Tianyi Mao, Henner Koch, Jiamin Zhuo, Antal Berenyi, Shigeyoshi Fujisawa, Yun Wei A. Hsu, Alfredo J. Garcia Iii, Xuan Gu, and Sebastien Zanella. A toolbox of cre-dependent optogenetic transgenic mice for light-induced activation and silencing. *Nature Neuroscience*, 15(5):793, 2012.

[104] Benjamin Judkewitz, Matteo Rizzi, Kazuo Kitamura, and Michael Husser. Targeted single-cell electroporation of mammalian neurons in vivo. *Nature Protocols*, 4(6):862–9, 2009.

[105] M Schwaerzle, P Elmlinger, O Paul, and P Ruther. Miniaturized tool for optogenetics based on an LED and an optical fiber interfaced by a silicon housing. pages 5252–5255, 2014.

[106] Niall McAlinden, Erdan Gu, Martin D Dawson, Shuzo Sakata, and Keith Mathieson. Optogenetic activation of neocortical neurons in vivo with a sapphire-based micro-scale led probe. *Frontiers in neural circuits*, 9:25, 2015.

[107] Robert Scharf, Tomomi Tsunematsu, Niall Mcalinden, Martin D. Dawson, Shuzo Sakata, and Keith Mathieson. Depth-specific optogenetic control in vivo with a scalable, high-density μLED neural probe. *Sci Rep*, 6:28381, 2016.

[108] Ferruccio Pisanello, Leonardo Sileo, Ian A Oldenburg, Marco Pisanello, Luigi Martiradonna, John A Assad, Bernardo L Sabatini, and Massimo De Vittorio. Multipoint-emitting optical fibers for spatially addressable in vivo optogenetics. *Neuron*, 82(6):1245–1254, 2014.

[109] A. R. Adamantidis, F. Zhang, A. M. Aravanis, K Deisseroth, and Lecea L De. Neural substrates of awakening probed with optogenetic control of hypocretin neurons. *Nature*, 450(7168):420–424, 2007.

[110] Alexander M Aravanis, Li-Ping Wang, Feng Zhang, Leslie A Meltzer, Murtaza Z Mogri, M Bret Schneider, and Karl Deisseroth. An optical neural interface: in vivo control of rodent motor cortex with integrated fiberoptic and optogenetic technology. *Journal of neural engineering*, 4(3):S143, 2007.

[111] Gabriel Gagnon-Turcotte, Alireza Avakh Kisomi, Reza Ameli, Charles-Olivier Dufresne Camaro, Yoan LeChasseur, Jean-Luc Néron, Paul Brule Bareil, Paul Fortier, Cyril Bories, Yves De Koninck, et al. A wireless optogenetic headstage with multichannel electrophysiological recording capability. *Sensors*, 15(9):22776–22797, 2015.

[112] Nir Grossman, Vincent Poher, Matthew S Grubb, Gordon T Kennedy, Konstantin Nikolic, Brian McGovern, Rolando Berlinguer Palmini, Zheng Gong, Emmanuel M Drakakis, Mark AA Neil, et al. Multi-site optical excitation using ChR2 and micro-LED array. *Journal of neural engineering*, 7(1):016004, 2010.

[113] Takashi Tokuda, Hiroshi Kimura, Tomoaki Miyatani, Yasuyo Maezawa, Takuma Kobayashi, Toshihiko Noda, Kiyotaka Sasagawa, and Jun Ohta. CMOS on-chip bio-imaging sensor with integrated micro light source array for optogenetics. *Electronics letters*, 48(6):312–314, 2012.

[114] Fan Wu, Eran Stark, Pei-Cheng Ku, Kensall D Wise, György Buzsáki, and Euisik Yoon. Monolithically integrated μleds on silicon neural probes for high-resolution optogenetic studies in behaving animals. *Neuron*, 88(6): 1136–1148, 2015.

[115] K. Kim, D. English, S. McKenzie, F. Wu, E. Stark, J. Seymour, P.-C. Ku, K. Wise, G. Buzsaki, and E. Yoon. *GaN*-on-*Si* *μLED* optoelectrodes for high-spatiotemporal-accuracy optogenetics in freely behaving animals. In *Electron Devices Meeting*, pages 26.5.1–26.5.4, 2017.

[116] H. J. Round. A note on carborundum. *Electrical World*, 19, 1907.

[117] H Welker. On new semiconducting compounds. 1952.

[118] Nick Holonyak Jr and SF Bevacqua. Coherent (visible) light emission from ga (as_{1-x} p_x)) junctions. *Applied Physics Letters*, 1(4):82–83, 1962.

[119] M. E. (Mikhail Efimovich) Levinshten, S. L Rumyantsev, and Michael Shur. *Properties of advanced semiconductor materials : GaN, AlN, InN, BN, SiC, SiGe*. John Wiley, 2008.

[120] M. Fukuda. *Optical Semiconductor Devices*. A Wiley Interscience publication. Wiley, 1999. ISBN 9780471149590. URL `https://books.google.co.uk/books?id=I_J5uyUxOu4C`.

[121] J. P. Colinge and C. A. Colinge. Physics of semiconductor devices. *Materials Today*, 6(1):34, 2003.

[122] E Fred Schubert. *Light-emitting diodes*. E. Fred Schubert, 2018.

[123] Simon Aldridge and Anthony J Downs. *The Group 13 Metals Aluminium, Gallium, Indium and Thallium: Chemical Patterns and Peculiarities*. John Wiley & Sons, 2011.

[124] S Bouneau, A Brunelle, S Dellanegra, J Depauw, D Jacquet, Y Le Beyec, M Pautrat, M Fallavier, J. C Poizat, and H. H Andersen. Very large gold and silver sputtering yields induced by kev to mev energy aun clusters (n=1-13). *Phys.rev.b*, 65(14), 2002.

[125] SJ Pearton, JC Zolper, RJ Shul, and F Ren. Gan: Processing, defects, and devices. *Journal of applied physics*, 86(1):1–78, 1999.

[126] XA Cao, H Cho, SJ Pearton, GT Dang, AP Zhang, F Ren, RJ Shul, L Zhang, R Hickman, and JM Van Hove. Depth and thermal stability of dry etch damage in gan schottky diodes. *Applied physics letters*, 75(2):232–234, 1999.

[127] JK Sheu, YK Su, GC Chi, WC Chen, CY Chen, CN Huang, JM Hong, YC Yu, CW Wang, and EK Lin. The effect of thermal annealing on the ni/au contact of p-type gan. *Journal of applied physics*, 83(6):3172–3175, 1998.

[128] AH Marblestone, BM Zamft, YG Maguire, et al. Physical principles for scalable neural recording. 2013. *Available at: ArXiv. org/abs/1306.5709*.

[129] Martin J Walker. Comparison of bosch and cryogenic processes for patterning high-aspect-ratio features in silicon. In *MEMS Design, Fabrication, Characterization, and Packaging*, volume 4407, pages 89–100. International Society for Optics and Photonics, 2001.

[130] Ming Yin and Maysam Ghovanloo. A low-noise preamplifier with adjustable gain and bandwidth for biopotential recording applications. In *Circuits and Systems, 2007. ISCAS 2007. IEEE International Symposium on*, pages 321–324. IEEE, 2007.

[131] Ghazi Ben Hmida, Abdennaceur Kachouri, and Hamadi Ghariani. Design of a micro power amplifier for neural signal recording. In *Systems, Signals and Devices, 2009. SSD'09. 6th International Multi-Conference on*, pages 1–4. IEEE, 2009.

[132] Matthew R Angle and Andreas T Schaefer. Neuronal recordings with solid-conductor intracellular nanoelectrodes (scines). *PLoS One*, 7(8):e43194, 2012.

[133] Morton Schwartz. Electrodes and the measurement of bioelectric events. *Journal of Clinical Engineering*, 2(2):169, 1977.

[134] ET McAdams, A Lackermeier, JA McLaughlin, D Macken, and J Jossinet. The linear and non-linear electrical properties of the electrode-electrolyte interface. *Biosensors and Bioelectronics*, 10(1-2):67–74, 1995.

[135] Song Zhang, Yilin Song, Mixia Wang, Zhiming Zhang, Xinyi Fan, Xianteng Song, Ping Zhuang, Feng Yue, Piu Chan, and Xinxia Cai. A silicon based implantable microelectrode array for electrophysiological and dopamine recording from cortex to striatum in the non-human primate brain. *Biosensors and Bioelectronics*, 85:53–61, 2016.

[136] C Nick, S Yadav, R Joshi, JJ Schneider, and C Thielemann. A three-dimensional microelectrode array composed of vertically aligned ultra-dense carbon nanotube networks. *Applied Physics Letters*, 107(1):013101, 2015.

[137] Yichen Lu, Xin Liu, Ryoma Hattori, Chi Ren, Xingwang Zhang, Takaki Komiyama, and Duygu Kuzum. Ultralow impedance graphene microelectrodes with high optical transparency for simultaneous deep two-photon imaging in transgenic mice. *Advanced Functional Materials*, page 1800002, 2018.

[138] Steve Yaeli, Einat Binyamin, and Shy Shoham. Form-function relations in cone-tipped stimulating microelectrodes. *Frontiers in neuroengineering*, 2: 13, 2009.

[139] K Mathieson, S Kachiguine, C Adams, W Cunningham, D Gunning, V O'shea, KM Smith, EJ Chichilnisky, AM Litke, A Sher, et al. Large-area microelectrode arrays for recording of neural signals. *IEEE Transactions on Nuclear Science*, 51(5):2027–2031, 2004.

[140] Wendy Franks, Iwan Schenker, Patrik Schmutz, and Andreas Hierlemann. Impedance characterization and modeling of electrodes for biomedical applications. *IEEE Transactions on Biomedical Engineering*, 52(7):1295–1302, 2005.

[141] Allen J Bard, Larry R Faulkner, Johna Leddy, and Cynthia G Zoski. *Electrochemical methods: fundamentals and applications*, volume 2. wiley New York, 1980.

[142] John E Ferguson, Chris Boldt, and A David Redish. Creating low-impedance tetrodes by electroplating with additives. *Sensors and Actuators A: Physical*, 156(2):388–393, 2009.

[143] K. A. Ludwig, J. D. Uram, J. Yang, D. C. Martin, and D. R. Kipke. Chronic neural recordings using silicon microelectrode arrays electrochemically deposited with a poly(3,4-ethylenedioxythiophene) (pedot) film. *Journal of Neural Engineering*, 3(1):59, 2006.

[144] Kip A Ludwig, Nicholas B Langhals, Mike D Joseph, Sarah M Richardson-Burns, Jeffrey L Hendricks, and Daryl R Kipke. Poly (3, 4-ethylenedioxythiophene)(pedot) polymer coatings facilitate smaller neural recording electrodes. *Journal of neural engineering*, 8(1):014001, 2011.

[145] Edward W Keefer, Barry R Botterman, Mario I Romero, Andrew F Rossi, and Guenter W Gross. Carbon nanotube coating improves neuronal recordings. *Nature nanotechnology*, 3(7):434, 2008.

[146] Alberto Ansaldo, Elisa Castagnola, Emma Maggiolini, Luciano Fadiga, and Davide Ricci. Superior electrochemical performance of carbon nanotubes directly grown on sharp microelectrodes. *ACS nano*, 5(3):2206–2214, 2011.

[147] Gytis Baranauskas, Emma Maggiolini, Elisa Castagnola, Alberto Ansaldo, Alberto Mazzoni, Gian Nicola Angotzi, Alessandro Vato, Davide Ricci, Stefano Panzeri, and Luciano Fadiga. Carbon nanotube composite coating of neural microelectrodes preferentially improves the multiunit signal-to-noise ratio. *Journal of neural engineering*, 8(6):066013, 2011.

[148] Takashi DY Kozai, Zhanhong Du, Zhannetta V Gugel, Matthew A Smith, Steven M Chase, Lance M Bodily, Ellen M Caparosa, Robert M Friedlander, and X Tracy Cui. Comprehensive chronic laminar single-unit, multi-unit, and local field potential recording performance with planar single shank electrode arrays. *Journal of neuroscience methods*, 242:15–40, 2015.

[149] Zongya Zhao, Ruxue Gong, Liang Zheng, and Jue Wang. In vivo neural recording and electrochemical performance of microelectrode arrays modified by rough-surfaced aupt alloy nanoparticles with nanoporosity. *Sensors*, 16 (11):1851, 2016.

[150] Jiangang Du, Timothy J Blanche, Reid R Harrison, Henry A Lester, and Sotiris C Masmanidis. Multiplexed, high density electrophysiology with nanofabricated neural probes. *PloS one*, 6(10):e26204, 2011.

[151] Kimberly M Scott, Jiangang Du, Henry A Lester, and Sotiris C Masmanidis. Variability of acute extracellular action potential measurements with multisite silicon probes. *Journal of neuroscience methods*, 211(1):22–30, 2012.

[152] T Chung, JQ Wang, J Wang, B Cao, Y Li, and SW Pang. Electrode modifications to lower electrode impedance and improve neural signal recording sensitivity. *Journal of neural engineering*, 12(5):056018, 2015.

[153] G Kovacs. Introduction to the theory, design, and modeling of thin-film microelectrodes for neural interfaces. *Enabling technologies for cultured neural networks*, 1994.

[154] Emily S Kappenman and Steven J Luck. The effects of electrode impedance on data quality and statistical significance in erp recordings. *Psychophysiology*, 47(5):888–904, 2010.

[155] Anthony M Dymond, Lloyd E Kaechele, John M Jurist, and Paul H Crandall. Brain tissue reaction to some chronically implanted metals. *Journal of neurosurgery*, 33(5):574–580, 1970.

[156] Sharanya Arcot Desai, John D Rolston, Liang Guo, and Steve M Potter. Improving impedance of implantable microwire multi-electrode arrays by ultrasonic electroplating of durable platinum black. *Frontiers in neuroengineering*, 3:5, 2010.

[157] Raeyoung Kim and Yoonkey Nam. Novel platinum black electroplating technique improving mechanical stability. In *Engineering in Medicine and Biology Society (EMBC), 2013 35th Annual International Conference of the IEEE*, pages 184–187. IEEE, 2013.

[158] Kilhwa Pi, Jong Yoon Shin, Suk Won Jung, Sangmin Lee, and Dong-il Dan Cho. Electrical characterization of nanostructured 3d microelectrodes for retinal neuron stimulation. In *SENSORS, 2015 IEEE*, pages 1–4. IEEE, 2015.

[159] Christine E Collins, David C Airey, Nicole A Young, Duncan B Leitch, and Jon H Kaas. Neuron densities vary across and within cortical areas in primates. *Proceedings of the National Academy of Sciences*, 107(36):15927–15932, 2010.

[160] John O'Kusky and Marc Colonnier. A laminar analysis of the number of neurons, glia, and synapses in the visual cortex (area 17) of adult macaque monkeys. *Journal of Comparative Neurology*, 210(3):278–290, 1982.

[161] Per Andersen, Richard Morris, David Amaral, John O'Keefe, and Tim Bliss. *The hippocampus book*. Oxford university press, 2007.

[162] Niall McAlinden, David Massoubre, Elliot Richardson, Erdan Gu, Shuzo Sakata, Martin D Dawson, and Keith Mathieson. Thermal and optical characterization of micro-led probes for in vivo optogenetic neural stimulation. *Optics letters*, 38(6):992–994, 2013.

[163] Stanley Finger. *Origins of neuroscience: a history of explorations into brain function*. Oxford University Press, USA, 2001.

[164] Bruce Fischl and Anders M Dale. Measuring the thickness of the human cerebral cortex from magnetic resonance images. *Proceedings of the National Academy of Sciences*, 97(20):11050–11055, 2000.

[165] Jürgen K Mai and George Paxinos. *The human nervous system*. Academic Press, 2011.

[166] Constantin Freiherr von Economo, Georg N Koskinas, and Lazaros C Triarhou. Atlas of cytoarchitectonics of the adult human cerebral cortex. 2008.

[167] L. Heimer. *The Human Brain and Spinal Cord: Functional Neuroanatomy and Dissection Guide*. Springer New York, 2012. ISBN 9781468401509. URL `https://books.google.co.uk/books?id=dMvkBwAAQBAJ`.

[168] Niall McAlinden, Yunzhou Cheng, Robert Scharf, Enyuan Xie, Erdan Gu, Martin D Dawson, Christopher Reiche, Rohit Sharma, Prashant Tathireddy, Loren Rieth, et al. A multi-site microled optrode array for neural interfacing. *bioRxiv*, page 480582, 2018.

[169] Pengfei Tian, Jonathan JD McKendry, Zheng Gong, Benoit Guilhabert, Ian M Watson, Erdan Gu, Zhizhong Chen, Guoyi Zhang, and Martin D Dawson. Size-dependent efficiency and efficiency droop of blue ingan micro-light emitting diodes. *Applied Physics Letters*, 101(23):231110, 2012.

[170] Jonathan JD McKendry, David Massoubre, Shuailong Zhang, Bruce R Rae, Richard P Green, Erdan Gu, Robert K Henderson, AE Kelly, and Martin D Dawson. Visible-light communications using a cmos-controlled micro-light-emitting-diode array. *Journal of lightwave technology*, 30(1):61–67, 2012.

[171] AA Greshnov, AE Chernyakov, BY Ber, DV Davydov, AP Kovarskyi, NM Shmidt, FM Snegov, OA Soltanovich, PS Vergeles, EB Yakimov, et al. Comparative study of quantum efficiency of blue led with different nanostructural arrangement. *physica status solidi c*, 4(8):2981–2985, 2007.

[172] Raymond A Serway and John W Jewett. *Principles of physics*, volume 1. Saunders College Pub. Fort Worth, TX, 1998.

[173] Michael J Doughty. ph dependent spectral properties of sodium fluorescein ophthalmic solutions revisited. *Ophthalmic and Physiological Optics*, 30(2): 167–174, 2010.

[174] Roland Pomfret, Gurwattan Miranpuri, and Karl Sillay. The substitute brain and the potential of the gel model. *Annals of neurosciences*, 20(3): 118, 2013.

[175] Jessica A Cardin, Marie Carln, Konstantinos Meletis, Ulf Knoblich, Feng Zhang, Karl Deisseroth, Li Huei Tsai, and Christopher I Moore. Targeted optogenetic stimulation and recording of neurons in vivo using cell-type-specific expression of channelrhodopsin-2. *Nature Protocols*, 5(2):247–254, 2010.

[176] X. Liu, Y. Lu, E. Iseri, Y. Shi, and D. Kuzum. A compact closed-loop optogenetics system based on artifact-free transparent graphene electrodes. *Frontiers in Neuroscience*, 12, 2018.

[177] Joseph M. Stujenske, Timothy Spellman, and Joshua A. Gordon. Modeling the spatiotemporal dynamics of light and heat propagation for in vivo optogenetics. *Cell Reports*, 12(3):525–534, 2015.

[178] Thompson SM, Masukawa LM, and Prince DA. Temperature dependence of intrinsic membrane properties and synaptic potentials in hippocampal ca1 neurons in vitro. *Journal of Neuroscience the Official Journal of the Society for Neuroscience*, 5(3):817, 1985.

[179] M Volgushev, T. R. Vidyasagar, M Chistiakova, and U. T. Eysel. Synaptic transmission in the neocortex during reversible cooling. *Neuroscience*, 98(1): 9–22, 2000.

[180] FLIR SC7000 Series. URL `http://www.flirmedia.com/MMC/THG/Brochures/RND_017/RND_017_US.pdf`.

[181] SH Price. The peltier effect and thermoelectric cooling. *WWW-dokumentti. Saatavilla: http://ffden-2. phys. uaf. edu/212_spring2007. web. dir/sedona_price/phys_212_webproj_peltier. html [viitattu 20.5. 2017]*, 2007.

[182] F. R Caldwell. Thermocouple materials. *Technical Report Archive and Image Library*, page 81, 1962.

[183] Samarendra K Mohanty and Vasudevan Lakshminarayananan. Optical techniques in optogenetics. *Journal of modern optics*, 62(12):949–970, 2015.

[184] H M Hoffmann and V E Dionne. Temperature dependence of ion permeation at the endplate channel. *Journal of General Physiology*, 81(5):687–703, 1983.

[185] E Moser, I Mathiesen, and P Andersen. Association between brain temperature and dentate field potentials in exploring and swimming rats. *Science*, 259(5099):1324–1326, 1993.

[186] Joel R. Stiles, Irina V. Kovyazina, Edwin E. Salpeter, and Miriam M. Salpeter. The temperature sensitivity of miniature endplate currents is mostly governed by channel gating: Evidence from optimized recordings and monte carlo simulations. *Biophysical Journal*, 77(2):1177–87, 1999.

[187] S Fujii, H Sasaki, K Ito, K Kaneko, and H Kato. Temperature dependence of synaptic responses in guinea pig hippocampal ca1 neurons in vitro. *Cellular & Molecular Neurobiology*, 22(4):379–391, 2002.

[188] Ki Yong Kwon, Brenton Sirowatka, Arthur Weber, and Wen Li. Opto-μecog array: A hybrid neural interface with transparent μecog electrode array and integrated leds for optogenetics. *IEEE transactions on biomedical circuits and systems*, 7(5):593–600, 2013.

[189] Michael Schwaerzle, Philipp Elmlinger, Oliver Paul, and Patrick Ruther. Miniaturized 3× 3 optical fiber array for optogenetics with integrated 460 nm light sources and flexible electrical interconnection. pages 162–165, 2015.

[190] Norhafizah Burham, Azrul Azlan Hamzah, and Burhanuddin Yeop Majlis. Effect of isopropyl alcohol (ipa) on etching rate and surface roughness of silicon etched in koh solution. In *2015 IEEE Regional Symposium on Micro and Nanoelectronics (RSM)*, pages 1–4. IEEE, 2015.

[191] Joho Yun, Jinhwan Kim, and Jong-Hyun Lee. Fabrication of fine electrodes on the tip of hypodermic needle using photoresist spray coating and flexible photomask for biomedical applications. *JoVE (Journal of Visualized Experiments)*, (129):e56622, 2017.